



Leibniz  
Universität  
Hannover



**Ludwig-Franzius-Institute**  
for Hydraulic, Estuarine and  
Coastal Engineering



**FH AACHEN**  
UNIVERSITY OF APPLIED SCIENCES

# 03KIS118/9 waveSTEPS

## FINAL REPORT 01.08.2016 – 31.07.2019

31.01.2020

Report-Nr.: 776

Leibniz University Hannover

Talia Schoonees, M.Eng.

Dr.-Ing. Nils Kerpen

Prof. Dr.-Ing. habil. Torsten Schlurmann

(Project coordinator)

Nienburger Straße 4  
D-30167 Hannover  
Tel: +49 (0)511 762-2572  
Fax: +49 (0)511 762-4002  
schlurmann@lufi.uni-hannover.de  
www.lufi.uni-hannover.de

FH Aachen

Daniel Valero, PhD

Prof. Dr.-Ing Daniel Bung

Bayernallee 9  
D-52066 Aachen  
Tel: +49 (0)241 6009-51117  
Fax: +49 (0)241 6009-51125  
bung@fh-aachen.de  
www.wasserbau.fh-aachen.de

SPONSORED BY THE



Federal Ministry  
of Education  
and Research

SPONSORED BY THE



Federal Ministry  
of Education  
and Research

The authors are responsible for the content of this publication

## Table of contents

List of symbols.....	5
1. Project overview .....	6
1.1 Background and scope.....	6
1.2 Requirements and objectives .....	6
1.3 Project planning and execution.....	7
1.4 State of the art .....	8
1.4.1 WP1: Model tests in wave flume.....	8
1.4.2 WP2: Model tests in current flume .....	16
1.5 Cooperation with other institutions.....	19
2 Project results: Work Package 1 and 3.....	19
2.1 Experimental setups.....	19
2.1.1 WKS dataset.....	19
2.1.2 1V:6H dataset.....	21
2.1.3 GWK dataset.....	23
2.2 Wave run-up.....	25
2.2.1 Background.....	25
2.2.2 Measurements and data analysis.....	26
2.2.3 Results and discussion.....	26
2.2.4 Conclusions.....	27
2.3 Wave overtopping.....	28
2.3.1 Background.....	28
2.3.2 Measurements and data analysis.....	28
2.3.3 Results and discussion.....	29
2.3.4 Conclusions.....	31
2.4 Wave impact pressures.....	33
3 Project results: Work Package 2.....	35
3.1 Experimental setups, instrumentation and data analysis.....	35
3.1.1 Presentation.....	35
3.1.2 Experimental setup.....	35
3.1.3 Instrumentation and data analysis.....	40
3.2 Flow depths.....	45
3.2.1 Introduction.....	45
3.2.2 Mean flow depths.....	46
3.2.3 Mean flow depth gradients.....	48
3.2.4 Flow depth fluctuations.....	49
3.2.5 Conclusions.....	49

3.3	Flow velocities.....	50
3.3.1	Velocity determination techniques.....	50
3.3.2	Measuring locations.....	50
3.3.3	Mean velocity fields.....	51
3.3.4	Velocity gradients.....	52
3.3.5	Turbulence and shear stresses.....	53
3.3.6	Conclusions.....	54
3.4	Energy dissipation.....	55
3.4.1	Introduction.....	55
3.4.2	Friction factors from flow depth data.....	55
3.4.3	Friction factors from velocity gradients.....	56
3.4.4	Comparison to open-channel flows over macro-roughness elements.....	57
3.4.5	Conclusions.....	58
3.5	Grass-step interface.....	59
3.5.1	Introduction.....	59
3.5.2	Results.....	60
3.5.3	Conclusions.....	62
3.6	Flow parameters of stepped revetments under regular waves.....	63
3.6.1	Introduction.....	63
3.6.2	Experimental setup and instrumentation.....	63
3.6.3	Test conditions.....	65
3.6.4	Flow processes.....	65
4	Discussion.....	68
4.1	Stepped revetment geometry: recommendations.....	68
4.2	Flow processes of stepped revetments with varying step heights.....	68
5	Conclusions.....	70
	References.....	71
A	Appendix.....	77
A.1	Flow depth filtering technique (Robust Outlier Cutoff).....	77
A.2	Sampling time uncertainty on velocity measurements.....	78
A.3	Air concentration profiles.....	83

## List of symbols

$\alpha$	[°]	slope angle ( $\tan\alpha = 1/n$ )
$D$	[m]	hydraulic diameter
$f$	[-]	friction factor
$g$	[m/s <sup>2</sup> ]	gravity acceleration
$h$	[m]	local water depth
$H$	[m]	local wave height
$H_0$	[m]	deep water wave height
$H_{m0}$	[m]	spectral significant wave height
$H_s$	[m]	significant wave height in deep water
$k_s$	[m]	sand roughness
$k_s^+$	[-]	roughness Reynolds number
$L$	[m]	local wave length
$L_0$	[m]	wave length in deep water conditions
$L_{m-1,0}$	[m]	wave length calculated from spectral wave period
$m_n$	[m <sup>2</sup> s]	spectral moment
$n$	[-]	structure slope
$q$	[m <sup>3</sup> /(s·m)]	mean overtopping discharge
$R_c$	[m]	crest freeboard height
$R_{u,2\%}$	[m]	wave run-up height exceeded by 2 % of incident waves
$Re$	[-]	Reynolds number
$S_h$	[m]	step height
$T$	[s]	wave period
$T_{m-1,0}$	[s]	spectral wave period
$T_p$	[s]	peak wave period
$U$	[m/s]	mean flow velocity
$\delta$	[m]	boundary layer thickness
$\gamma_b$	[-]	influence factor for a berm
$\gamma_f$	[-]	influence factor for roughness of or on the slope
$\gamma_v$	[-]	influence factor for a crest wall
$\gamma_\beta$	[-]	influence factor for oblique wave attack
$\xi$	[-]	breaker parameter (Iribarren number)
$\xi_{m-1,0}$	[-]	breaker parameter based on spectral period $T_{m-1,0}$
$\tau_0$	[N/m <sup>2</sup> ]	wall mean shear

# 1. Project overview

## 1.1 Background and scope

Predictions indicate that the population and assets exposed to coastal risks will significantly increase in the coming decades as a result of population growth, economic development and urbanization in coastal regions (Wong et al. 2014). In addition, coastal areas are becoming increasingly vulnerable due to the anticipated effects of climate change, such as relative sea level rise as well as changes in storms and associated storm surges. As a result, it becomes increasingly important to ensure coastal safety.

Simultaneously, the population growth and economic development put additional pressures on the coastal areas that result in a higher demand for recreation and tourism. The function of the coastal zone is therefore not only to provide coastal safety, but also to offer space which are appealing to tourists and for recreational activities. In line with the given demands, there is a shift in coastal engineering towards implementing adapted or reinvented traditional coastal protection structures, such as dikes, to serve as a multi-functional solution. One example of such a multi-functional coastal protection structure, is a stepped revetment/dike. Figure 1.1 shows an example of a stepped revetment at Margate Seafront in the United Kingdom.

From a coastal engineering point of view, the main advantage of a stepped revetment (in comparison to a smooth slope dike with the same dimensions) is that the steps on the revetment create surface roughness which results in a reduction of wave run-up and overtopping. Stepped revetments can offer higher levels coastal safety compared to a smooth dike. In addition to offering coastal safety, a stepped revetment can promote tourism by providing access to water areas, creating walkways and/or serve as a bench. Another advantage is that a stepped revetment can be constructed from precast units.

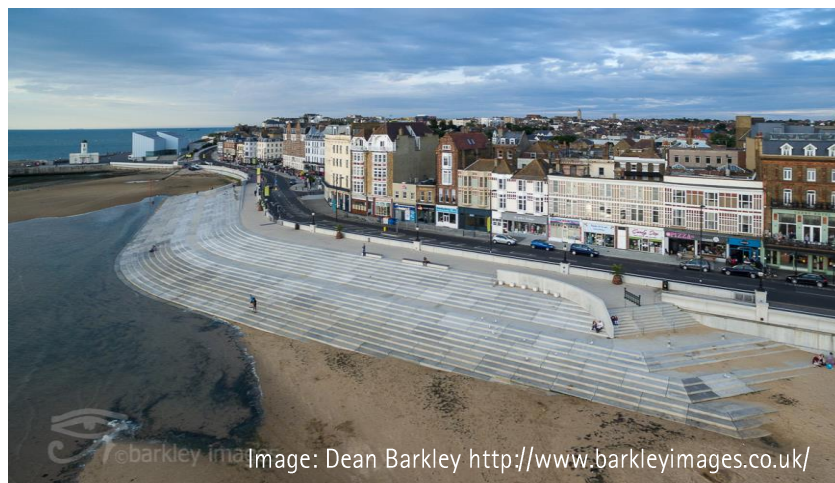


*Figure 1.1: Stepped revetment as multi-functional coastal protection structure at Margate Seafront, United Kingdom*

## 1.2 Requirements and objectives

Up to date no comprehensive systematic research studies (see Section 1.4) have been published on wave run-up and wave overtopping of stepped revetments. To address this shortcoming, the research project waveSTEPS, which stretches over a three year period, originated. The main aim of waveSTEPS is to systematically investigate wave run-up and wave overtopping of stepped revetments by means of physical model tests to ultimately provide design recommendations for stepped revetments.

The project was divided into three work packages, each with its own sub-objectives. The three work packages are outlined as follows:

1. WP1: Small scale physical model tests in the wave flume
2. WP2: Small scale physical model tests in the current flume
3. WP3: Full scale physical model tests in the Large Wave Flume (GWK)

Work Package 1 (WP1) and Work Package 3 (WP3) were conducted by Ludwig-Franzius-Institute (LuFI) at the Leibniz University Hannover (LUH), while Work Package 2 (WP2) is conducted by FH Aachen, University of Applied Sciences (FHAC).

WP1 investigated the system understanding of wave run-up and wave overtopping on stepped revetments through conducting physical model tests in a wave flume at LUH. These tests enabled the researchers to quantify wave run-up and wave overtopping for stepped revetments under a range of hydraulic and geometric boundary conditions. Predictions for wave run-up and/or wave overtopping are required for the crest level design for coastal structures. WP2 applied the same boundary conditions as WP1 to reproduce the physical model tests in stationary conditions within a current flume at FHAC. During the wave run-up and overtopping process, highly aerated conditions occur which cannot be scaled accurately. Therefore it is expected that the scaled physical model tests are subjected to significant scale effects. WP3 aimed to investigate these scale effects through conducting full scale model tests in the Large Wave Flume (GWK) situated in Hannover. Table 1.1 summarises the individual objectives for each work package.

*Table 1.1: Individual objectives for work packages*

Work package	Objective
WP1	Determine the wave run-up and wave overtopping of a stepped revetment in small scale for a range of boundary conditions (hydraulic and geometric)
WP2	Achieve a system understanding of the energy dissipation (turbulence, aeration) in the wave run-up process
WP3	Determine the scale effects

Overall the study aimed to gain a deeper understanding of the wave run-up process and to develop design recommendations for stepped revetments. More specifically the objective of the project was to determine the influence factor for roughness  $\gamma_f$  of a stepped revetment for wave run-up and wave overtopping (see Section 1.4 for definition of  $\gamma_f$ )

### 1.3 Project planning and execution

The project planning is summarised in Figure 1.2. A summary of the three work packages is given below:

**WP1:** Literature on stepped revetments as coastal structures was reviewed to identify knowledge gaps on the performance of stepped revetments. The literature review informed the selection of boundary conditions. Physical model tests were performed in a wave flume on stepped revetments with ranging slopes and step heights under various wave conditions representative for the German coast. Wave run-up, overtopping and wave pressures were measured. Roughness factors for wave run-up and overtopping were determined.

**WP2:** A thorough literature on friction in macro-roughness channels was conducted to identify most relevant parameters and requirements for a physical model study. Scaled model test were then carried out under steady flow conditions in a horizontal current flume with macro-roughness bottom. Flow depths and Froude numbers were varied in a range as expected to occur during the wave run-up on a stepped revetment. Subcritical as well as supercritical, aerated flows have been investigated with different type of instrumentation, depending on the flow condition in each setup. Resulting velocity field data and flow depth gradients are used to extract friction factors. Additionally, the turbulence and stresses occurring at the interface to a grass layer have been analysed.

WP3: Two typical stepped revetment cross-sections were selected to be tested in large scale. In the model tests, wave run-up and overtopping were measured. Resulting roughness factors were determined and compared to those in WP1 in order to assess possible scale effects. Design dimensioning are based on large results.

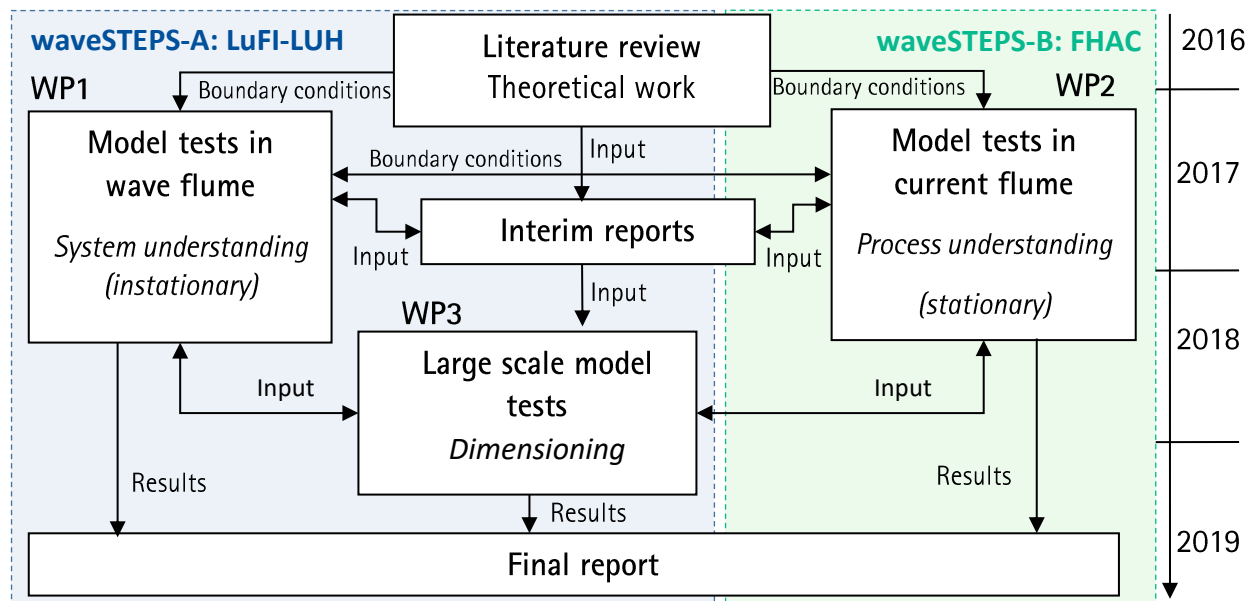


Figure 1.2: Collaboration between work packages

## 1.4 State of the art

### 1.4.1 WP1: Model tests in wave flume

#### 1.4.1.1 Wave run-up and overtopping

EurOtop (2018) provides the latest guidelines on wave run-up and wave overtopping of sea defences. The manual is largely based on European research, but also offers international application. The influence factor for roughness, or simply the roughness factor, ( $\gamma_f$ ) is present in both the prediction formula for wave run-up and wave overtopping. The equations for relatively gentle slopes ( $\cot\alpha \geq 2$ ), applicable for this project, are presented below.

The general equation for the mean value approach on the wave run-up is (EurOtop 2018):

$$\frac{R_{u2\%}}{H_{m0}} = 1.65 \cdot \gamma_b \cdot \gamma_f \cdot \gamma_\beta \cdot \xi_{m-1,0} \quad (1.1)$$

$$\text{with a maximum of } \frac{R_{u2\%}}{H_{m0}} = 1.0 \cdot \gamma_f \cdot \gamma_\beta \left( 4 - \frac{1.5}{\sqrt{\gamma_b \cdot \xi_{m-1,0}}} \right) \quad (1.2)$$

where  $R_{u2\%}$  is defined as the wave run-up height exceeded by 2% of the incoming waves [m],  $H_{m0}$  is the spectral significant wave height [m],  $\gamma_b$  depicts the influence factor for a berm [-],  $\gamma_f$  is the influence factor for the roughness elements on a slope [-],  $\gamma_\beta$  is the influence factor for oblique wave attack [-] and  $\xi_{m-1,0}$  is the breaker parameter [-].

The general equation for the average wave overtopping discharge on a slope (dike, levee, embankment) is (EurOtop 2018):

$$\frac{q}{\sqrt{g \cdot (H_{m0})^3}} = \frac{0.023}{\sqrt{\tan\alpha}} \cdot \gamma_b \cdot \xi_{m-1,0} \cdot \exp \left[ - \left( 2.7 \frac{R_c}{\xi_{m-1,0} \cdot H_{m0} \cdot \gamma_b \cdot \gamma_f \cdot \gamma_\beta \cdot \gamma_v} \right)^{1.3} \right] \quad (1.3)$$

$$\text{with a maximum of } \frac{q}{\sqrt{g \cdot (H_{m0})^3}} = 0.09 \cdot \exp \left[ - \left( 1.5 \frac{R_c}{H_{m0} \cdot \gamma_f \cdot \gamma_\beta \cdot \gamma^*} \right)^{1.3} \right] \quad (1.4)$$

where  $q$  is defined as the average overtopping discharge [ $m^3/(s.m)$ ],  $H_{m0}$  is the spectral significant wave height [m],  $R_c$  is the crest freeboard [m],  $\gamma_b$  depicts the influence factor for a berm [-],  $\gamma_f$  is the influence factor for the roughness elements on a slope [-],  $\gamma_\beta$  is the influence factor for oblique wave attack [-],  $\gamma_v$  is the influence factor for a wall at the end of a slope [-],  $\gamma^*$  is a combined factor for all kind of geometrical influences and  $\xi_{m-1,0}$  is the breaker parameter [-].

The factor for roughness,  $\gamma_f$ , gives the influence which roughness elements have on the wave run-up and wave overtopping when compared to a smooth slope with the same boundary conditions. Following the generic approach listed in (EurOtop 2018) the influence factor for roughness for wave run-up and wave overtopping in relation to the design case of stepped revetments can be defined as:

$$\gamma_f = \frac{R_{u2\% \text{ stepped revetment}}}{R_{u2\% \text{ smooth slope}}} \quad \text{for wave run – up} \quad (1-5)$$

$$\gamma_f = \frac{\ln(q_{\text{smooth slope}})}{\ln(q_{\text{stepped revetment}})} \quad \text{for wave overtopping} \quad (1-6)$$

$\gamma_f$	Influence factor for roughness
$q_{\text{stepped revetment}}$	Overtopping discharge for stepped revetment
$q_{\text{smooth slope}}$	Overtopping discharge for smooth slope
$R_{u2\% \text{ stepped revetment}}$	Run-height for stepped revetment
$R_{u2\% \text{ smooth slope}}$	Run-height for smooth slope

#### 1.4.1.2 Overview of studies on stepped revetments

As part of the research conducted prior to the start of project waveSTEPS, Kerpen and Schlurmann (2016) undertook a comprehensive literature review to assess and summarise previous research on stepped revetments. The review included the available knowledge on wave run-up, wave overtopping and wave loads on stepped revetments. Figure 1.3 defines the important parameters for stepped revetments. Although stepped revetments have been implemented for more than 60 years, Kerpen and Schlurmann (2016) found that no comprehensive studies have been conducted with a wide range of hydraulic and geometric boundary conditions. As a result, also no generic design guidelines for stepped revetments exist.

The first documentation on a stepped seawall is presented by O'Shaughnessy et al. (1924). They discuss the design and construction of a seawall along a highway along a San Franciscan beach, California that offer protection against erosion. The seawall consisted of a stepped revetment with a recurved wall at its crest.

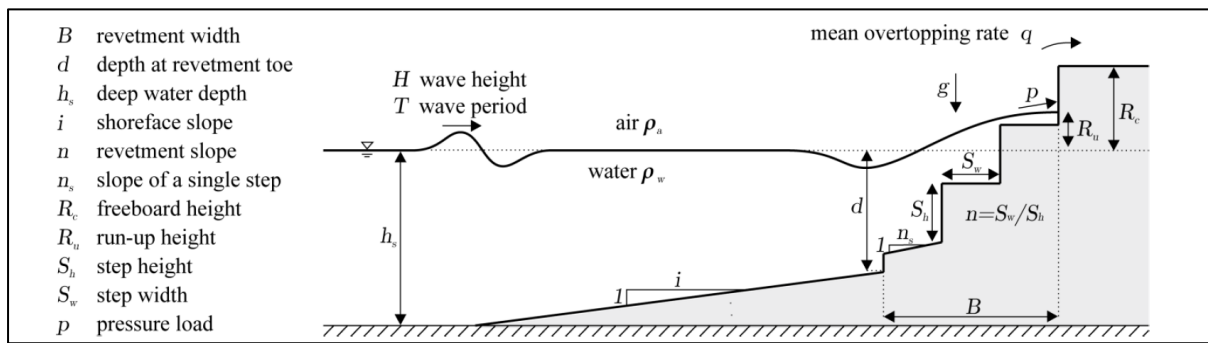


Figure 1.3: Parameter definition (Kerpen and Schlurmann, 2016)

Saville (1955) conducted physical model tests with regular waves on a stepped revetments ( $\cot\alpha=1.5$ ) at a geometric scale of 1:17. Wave run-up and wave overtopping were measured and is analysed and interpreted in Saville (1955, 1956, 1957). He found that wave run-up and wave overtopping increase with higher wave heights, wave periods and surf similarities.

Wassing (1957) reports on wave run-up tests on stepped revetments ( $\cot\alpha=1.5$ ) under regular waves. Two step heights of  $S_h=0.14$  m and  $S_h=0.35$  m were tested, with the larger steps performing only slightly better.

Furthermore, Jachowski (1964) tested wave run-up and overtopping under regular waves on two stepped revetments slopes ( $\cot\alpha=2; 3$ ) with  $S_h=0.19$  m, at a geometric scale of 1:16. He noted that wave run-up and overtopping are larger for surging than for plunging waves.

Nussbaum and Colley (1971) present findings of model tests on wave run-up on both a smooth slope and a stepped slope constructed of soil cement. They found lower wave run-up on the stepped slope compared to the smooth slope and concluded that steeper stepped slopes result in higher run-up heights. In addition they observed that smaller steps were more effective in reducing run-up.

A study by Goda and Kishira (1976) was first to perform experiments with irregular waves on stepped revetments. Their study focused on low crested seawalls and were conducted at a scale of 1:33. In agreement with Nussbaum and Colley (1971), they established that stepped revetments decrease wave overtopping when compared to a smooth slope. However, they found that a stepped seawall requires a crest height 10–20% higher than a vertical seawall. Goda and Kishira (1976) also studied the influence of a foreshore on the wave overtopping performance of stepped seawalls and found that 1:30 foreshore result in overtopping volumes 30 times higher than for a 1:10 slope.

Stoa (1978) analysed data from previous studies (Saville (1955); Jachowski (1964); Nussbaum and Colley (1971)) of run-up at stepped revetments. He established that the relative water depth substantially influenced the wave run-up and found that for flat foreshores, the wave steepness has no meaningful influence on the reduction in wave run-up. A correction factor for scale effects is proposed.

Tabata et al. (1980) compiled existing designs of 107 stepped seawalls around Japan. Most of the revetments had slopes of  $\cot\alpha=3$ , while slopes varied between  $1.5 \leq \cot\alpha \leq 5$ . Step heights were mainly  $S_h=0.2; 0.25; 0.35$ , while 33 designs had step widths of 1.5 m and 21 designs with 1.0 m. In total only 17 structures had horizontal steps, while the others had inclined steps of slopes between 1:2.5 to 1:20. Additionally, the MLW is below the stepped revetment's toe.

In a technical note on seawalls, the United States Army Corps of Engineers (USACE) (1981) discuss stepped seawalls and their potential to dissipate wave forces, to reduce wave reflection, wave run-up and wave overtopping as well as scour.

Takayama et al. (1982) conducted tests with irregular waves to measure wave run-up and overtopping at low crested stepped seawalls. They tested three slopes ( $\cot\alpha=2; 3; 4$ ) with two step heights and a foreshore of 1:30. They found that overtopping volumes for stepped revetments are slightly higher than those of

vertical walls. The results indicate lower reduction in wave overtopping for flatter slopes and higher step ratios ( $S_h/H_{m0}$ ). Furthermore they found that increasing dimensionless wave overtopping lead to lower reduction factors. In other words, for higher relative overtopping, the performance of the stepped structure to reduce wave overtopping becomes less effective.

The Shore Protection Manual, USACE (1984), with reference to Saville (1955) and Saville (1956), describes the advantages of stepped seawalls and their suitability to offer coastal protection against moderate wave conditions.

Heimbaugh (1988) conducted physical model tests on stepped seawalls ( $\cot\alpha=1.5; 2$ ) with step heights of  $S_h=0.024$  at a scale of 1:19 with irregular waves. He measured wave overtopping and wave pressures. The tested structure included a recurve at the structure's crest and thus overtopping results are affected. He established that the maximum wave pressure is experienced within relation to the still water level.

Ward and Ahrens (1992) extended the data base by Heimbaugh (1988) by performing tests with additional wave heights and periods. They noted that stepped revetments dissipate wave energy by inducing more turbulence and thus reducing wave overtopping and derived an empirical formula for predicting wave overtopping of these structures.

For a project for at the Lake Michigan shoreline, for the city of Chicago, Ward (2003) conducted physical model tests at a scale of 1:35 on a stepped revetment with variable step heights to determine key design parameters of step heights and widths, crest level and number of steps. A reanalysis of Krecic and Sayao (2003), comment that the incident wave conditions were not measured at the toe of the structure. They performed a dimensional analysis and derive an empirical prediction.

In a project report, Van Steeg (2012), describes and presents results of model tests conducted on stepped revetment cross-sections with two slopes ( $\cot\alpha=2; 3$ ), each tested with two step heights  $S_h=0.023 ; 0.046$ . He presents reduction coefficients for stepped revetments that can be used in empirical predictions given by TAW (2002).

Xiaomin et al. (2013) conducted a large number of physical model tests to measure wave run-up with regular waves at a scale of 1:10. They tested one slope ( $\cot\alpha=2.5$ ) with five different step heights  $0.010 \leq S_h \leq 0.176$  and a smooth slope as reference to determine the reduction in wave run-up compared to a smooth slope. They found reduction factors between 0.35 and 0.77. Treuel (2013) showed an optimum reduction coefficient in the data of Xiaomin et al. (2013).

Kerpen et al. (2014) developed an empirical prediction for wave overtopping at stepped revetments under regular waves. Two slopes ( $\cot\alpha=2; 3$ ) were tested, each with step heights of  $S_h=0.04$  and  $0.08$  m. They found that relative overtopping rates are 2.5 times higher for  $\cot\alpha=2$  than for  $\cot\alpha=3$ .

Studies by Treuel (2013) and Van Steeg (2012) suggest that the wave height in relation to the step height, called the step ratio ( $H_{m0}/S_h$ ), influence the reduction in wave overtopping.

Table 1.2 gives an overview of the reduction factors and related boundary conditions of the previous studies.

Table 1.2 gives an overview of the reduction factors and related boundary conditions of the previous studies.

*Table 1.2: Summary of key boundary conditions*

Study	Waves	$H_{m0}/S_h$	$\cot\alpha$	$\gamma_f$
Saville (1955)	Regular	2-12	1.5	0.56 -0.80
Jachowski (1964)	Regular	1.3-15.0	2; 3	0.64-0.77
Nussbaum and Colley (1971)	Regular	2.5-8.0	3	0.67-0.82
Goda & Kishira (1976)	Irregular	19-29	2	0.70-0.90
Takayama et al. (1982)	Irregular	16-40	2; 3; 4	0.68-0.90
Heimbaugh (1988)	Irregular	9-10	1.5; 2.0	-
Van Steeg (2012)	Irregular	1.6-6.7	2; 3	0.60-0.90
Xiaomin et al. (2013)	Regular	0.2-8.0	2.5	0.35-0.77
Kerpen et al. (2014)	Regular	0.5-12	2; 3	0.14-0.50

#### 1.4.1.3 Boundary conditions and results of previous studies

In order to establish knowledge gaps, boundary conditions and test results from previous studies were compared (Kerpen and Schlurmann, 2016). Figure 1.4 presents the ranges of boundary conditions that were tested in previous research. Data points with black markers have been conducted with regular waves, while coloured markers present tests with irregular waves. It should be noted that the studies of Saville (1955) and Xiaomin (2013), which produced a lot of data, only included regular waves.

The majority of model tests have been conducted with intermediate water depths and moderate wave steepnesses, Figure 1.4 (a). The literature review also revealed that a range of slopes for stepped revetments were tested, namely slopes of 1:1.5 up to 1:4, Figure 1.4 (b). Even though a wide range of slopes were tested, no single study tested a wide range of slope angles. The influence of the slope angle on the system behaviour of stepped revetments is thus hard to assess since the tests were not performed with the same boundary conditions or scale.

Together the studies cover a wide range of breaker parameters, but again there is no single study that included a wide range of surf similarities (Iribarren numbers), Figure 1.4 (c). The relative step height has been identified as an important parameter that significantly influences the wave run-up and wave overtopping.

Strongly turbulent conditions occur during events of wave run-up and wave overtopping on stepped revetments. Turbulence cannot be scaled correctly in physical model tests and therefore the tests are subjected to scale effects. As a result, it is important to consider the Reynolds numbers (Re) of the model tests to minimise the scale effects due to turbulent conditions. Figure 1.4 (d) presents the Reynolds numbers for the previous studies. All the data sets have Reynolds numbers larger than  $3 \times 10^4$ , thus exceeding the critical limit as defined by Dai and Kamel (1969).

The dimensionless wave run-up versus the surf similarity (Iribarren number) is presented in Figure 1.5(a). The graph presents significant scatter but indicate that the dimensionless wave run-up increases with an increasing breaker parameter.

Figure 1.5(b) expresses the dimensionless overtopping versus the relative freeboard. Significant differences in the findings of studies can be seen, however the results from each study present a distinguishable separate cloud of data points. These differences in magnitude for the dimensionless overtopping for the same relative freeboard, can be explained by different geometric boundary conditions, scales and breaker parameters between studies. Figure 1.5 (c) includes the influence of the different breaker parameters.

The influence factor for roughness versus the relative step height, depending on the structure slope and breaker parameter, is presented in Figure 1.5 (d). The data by Xiaomin (2013) indicates a tentative optimum for the influence factor for roughness. However, this tentative optimum should also be verified by tests with spectral waves to make definitive conclusions.

The results from previous studies indicated that wave run-up ( $R_w$ ) and wave overtopping ( $q$ ) decrease with increasing wave steepness ( $H/L$ ), with decreasing slope ( $n$ ) and increasing freeboard ( $R_c$ ). Also the presence of a foreshore in front of the structure, leads to a decrease in wave run-up and overtopping.

From the comprehensive literature review it is evident that additional research is required to identify and describe the processes that take place during wave run-up and wave overtopping events. A wide range of hydraulic and geometric boundary conditions have to be included to provide generic design recommendations for stepped revetments.

#### *1.4.1.4 Wave loads on stepped revetments*

In contrast to wave run-up and overtopping, only a small number of studies mention wave loads on stepped revetments. USACE (1984) recommends that the forces on stepped seawalls can be calculated with methods derived for vertical seawalls. Heimbaugh (1988) measured wave loads as part of his physical model test campaign at a scale of 1:19. Two stepped slopes ( $\cot\alpha=1.5; 2$ ) with a recurve at their crest were tested. He established that the position of the maximum measured impacts are influenced by the still water level. In a 1:20 scale model of a stepped revetment, Melby et al. (2009) measured the vertical wave impacts at a low sampling rate of 100 Hz, which is considered to be too low to capture peak wave impacts. The authors repeated tests 6 times and calculated the average maximum impacts, to account for loading bias between tests.

#### *1.4.1.5 Scale effects*

Scale models are an effective way to study wave processes on stepped revetments. When applying scaling laws, certain assumptions are made that lead to the incorrect representation of some processes. For studying wave processes on coastal structures, gravitational and inertial forces are dominant and therefore the Froude scaling is applied in most cases (Hughes 1993). When applying the Froude scaling law, viscosity, elasticity and surface tension are not correctly represented in small scale. These incorrect representations may lead to scale effects that contribute to inaccuracies e.g. in the dissipation of energy due to wave breaking and friction (Frostick et al. 2011).

An important factor that contribute to scale effects is air entrainment. Entrained air bubbles in turbulent flows are relatively larger in scale models whereas the air contents is lower. The lower level of aeration lead to less turbulence. Furthermore, air bubbles dampen wave impacts on structures and due to the reduced air content, wave pressures on structures measured in small scale are overestimating the wave impacts when scaled up (Cuomo et al. 2010). In contrast it has been shown that overtopping discharges and wave run-up heights are underestimated (Lykke Andersen et al. 2011).

Highly aerated flows have been observed during the wave run-up process on stepped revetments in small scale stepped revetments. The hypothesis is therefore that measurements taken in small scale model tests on stepped revetments are subjected to significant scale effects. Up to date, no prototype measurements on stepped revetments are available and thus scale effects are undetermined.

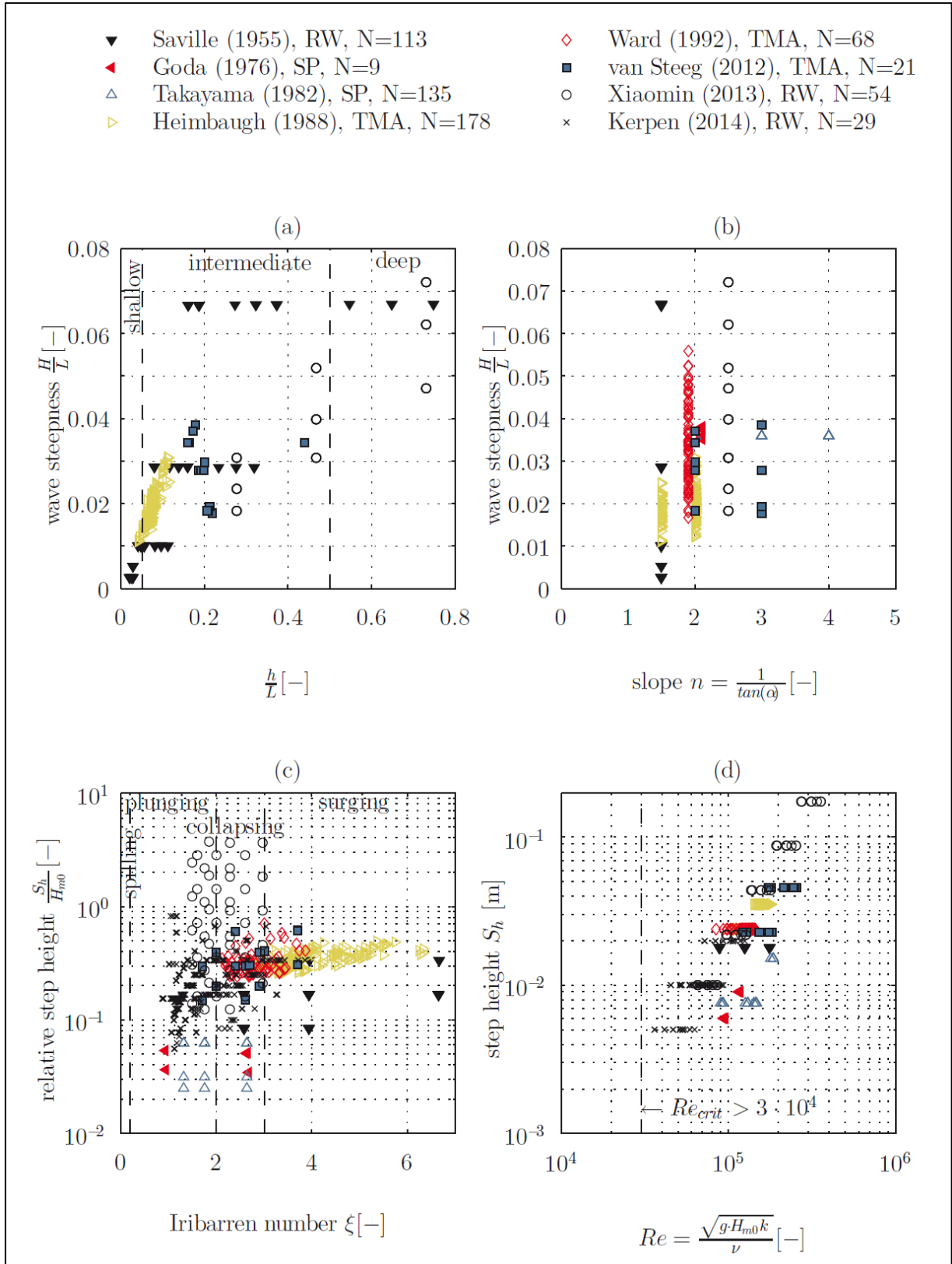


Figure 1.4: Boundary conditions from previous studies (Kerpen and Schlurmann, 2016)

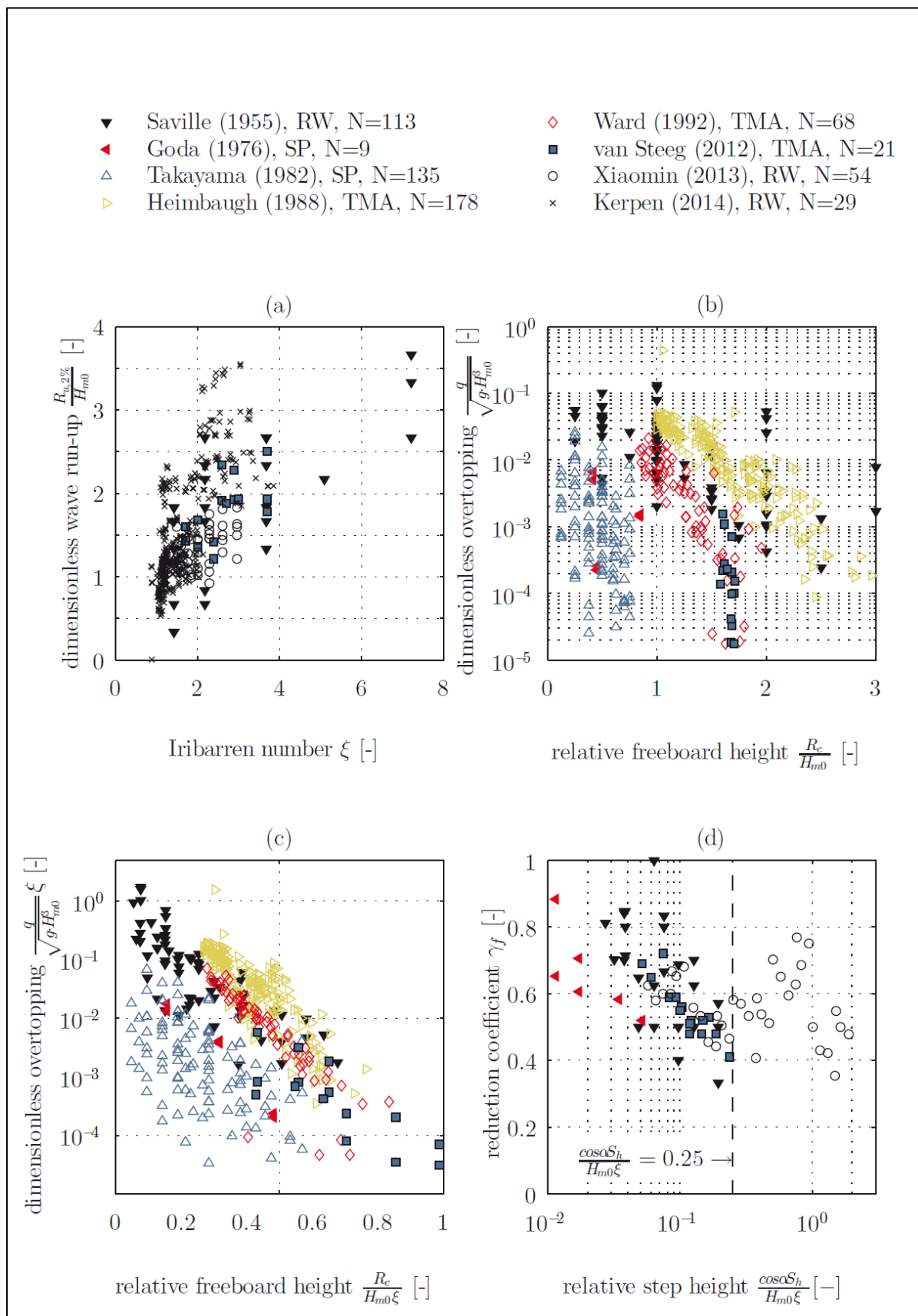


Figure 1.5: Test results from previous studies (Kerpen and Schlurmann, 2016)

#### 1.4.1.6 Knowledge gaps

Limited ranges of boundary conditions have been studied, and as such, a universal understanding of how waves interact with a stepped revetment is lacking. The influence of different step heights, slopes and variable hydraulic parameters on the wave run-up and overtopping of stepped revetments is unknown.

### 1.4.2 WP2: Model tests in current flume

#### 1.4.2.1 Energy dissipation in steady and unsteady flows over macro-roughness elements

Manning's (1895) approach for flow resistance is in fair agreement with Nikuradse's (1926, 1932) approach in case of medium relative roughness, i.e. the roughness related to the flow depth. However, they differ considerably for very rough channels. Consequently, modern studies focusing on the determination of the friction factor related to the flow over macro-roughness have preferred approaches close to the Nikuradse-type equation, where the equation coefficients are just modified to better fit the experimental data. Some examples are the studies on flow over boulders of Rice et al (1998), Pagliara and Chiavaccini (2006) or Oertel and Schlenkhoff (2012) among others; and, for stepped spillways flows: Tozzi (1994), Chamani and Rajaratnam (1999). Further information on the theoretical considerations can be found in Montes (1998) or Pope (2000).

Studies of flow over macro-roughness elements identified different flow regimes, which distinguished upon "rapid" and "stable tumbling" with another region in between named "unstable tumbling" Morris (1968). The tumbling regime is related to lower flow discharges and the rapid flow regime, otherwise, corresponds to larger discharges. When the flow is tumbling, the streamlines are pseudo-parallel to the macro-roughness elements with the free surface displacement mirroring the channel bed perturbations. However, this nomenclature for the flow regimes is not any more in use nowadays and different authors may make a different discrimination. A well accepted notation inspired in the stepped spillway literature is: nappe, transition and skimming flow regimes (Chanson and Toombes, 2002; 2004). The transition from one regime to another is usually expressed in terms of the critical depth and slope has a slight influence (Chanson et al., 2015). Stepped spillway flows may behave as a succession of free-falling nappes at low flows and as skimming flow at large discharges. However, there is a range of intermediate flow rates characterised by a chaotic flow motion associated with intense splashing (Chanson and Toombes, 2004). The nappe flow resembles a successive series of jets impacting against the sequent step face and thus producing some air entrainment. The skimming region is more alike an open channel flow where the steps geometry is "understood" by the flow as roughness elements as opposite to the nappe regime where it constitutes more of a channel bed geometry with the flow parallel to its faces. For the intermediate transition flow region, the dominant feature is the very-strong free-surface aeration, well in excess of observed data in smooth-invert and skimming flows.

Some research has been done on the determination of friction factors under steady conditions; see Rice et al (1998), Pagliara and Chiavaccini (2006) or Oertel and Schlenkhoff (2012) with special mention to the study of Yang and Lee (2007) which investigated Reynolds shear stresses in gradually varied flow over a rough channel. They concluded that despite some deviation from the linear distribution of Reynolds shear stress, the sum of Reynolds shear stress and the momentum flux remains a linear distribution. Yang and Lee (2007) also concluded that small differences occur from accelerating to decelerating flows. These conclusions are of interest since gradually varied flow is the most accessible way to study energy dissipation in a horizontal flume as the one used for WP2.

Graf and Song (1995) determined the shear stress in unsteady flows by using different methods. Song and Graf (1996) studied the flow properties over rough channels by means of an acoustic Doppler Velocity Profiler (ADVP). They obtained instantaneous flow profiles which were later analysed by using the Fourier components method in order to obtain something similar to a mean velocity estimation. Song and Graf (1996) concluded that the commonly accepted theory for steady flows is also applicable to unsteady flows despite some coefficients based on the flow acceleration might be necessary to correct the predictions.

Additionally, Reynolds stress was observed to be larger when the flow is accelerating than when it is decelerating. Dey and Lambert (2005) theoretically developed expressions for the Reynolds stress and the bed shear stress for non-uniform unsteady flow. Dey and Lambert (2005) assumed a logarithmic velocity distribution and used the Reynolds and continuity equations of two-dimensional open channel flows.

Recently, Mrokowska et al (2015) obtained instantaneous velocity information for a dam break type problem. By processing these data using the two dimensional Reynolds and the one dimensional Saint-Venant equations, Mrokowska et al (2015) obtained friction velocity estimations. Similarly to Song and Graf (1996), they used the Fourier components method in order to obtain something similar to a mean velocity estimation. Additionally, depth measurements were smoothed with the Savitzky-Golay filter to obtain smoother the depth derivatives. Soares-Frazão and Fent (2016) conducted some experiments with moderate unsteady flows over mobile beds and were able to determine the friction slope from the measured flow conditions and using three different shallow-water models.

The recent study of Felder and Chanson (2015) made the effort to put together all available datasets on friction factors estimation over stepped spillways (a structure which involves a similar flow as the one on stepped revetments).. Nonetheless, the observed values ranged from 0.02 to 0.70 without a clear trend even for very similar flow conditions.

#### *1.4.2.2 Turbulent boundary layers over rough surfaces*

Development of the turbulent boundary layer is linked to the energy dissipation properties. While flow out of the boundary layer can be considered irrotational with parallel streamlines taking place, as the flow is closer to the solid boundary the streamlines contort and bend forming extremely chaotic paths. The boundary of the layer is not sharp, the transition from the inner rotational flow with the main stream of the fluid is continuous (Landau and Lifshitz, 1987) and subject to intermittent ejections, which may cause the principal momentum transfer. For practical purposes, it is usually employed the boundary layer thickness ( $\delta$ ) as the limit of the boundary layer extent. This value is defined as the location normal to the wall where 99% of the free stream velocity is reached.

Turbulent boundary layer flows are a well-known case of shear flow. The basic knowledge on turbulent boundary layers can be found in classic literature on Fluid Mechanics (Schlichting 1968; Landau and Lifshitz, 1987; Pope 2000; White, 2006). Since the experimental study of Klebanoff (1955), many detailed studies have been published. It has been also object of numerical modelling, being the first Direct Numerical Simulation (DNS) published the one of Kim et al (1987). Other detailed numerical studies have been conducted incrementing, step by step, the Reynolds number up to the latest studies (see Lozano-Durán and Jiménez, 2014); however the interest of these studies remains far from the practical implications pursued by this project.

When studying the flow over a stepped geometry, it has been considered of special interest the studies dealing with boundary layers over rough walls. Recently, Cameron et al (2017) reported turbulent properties measurements for a rough wall boundary layer which have been digitized and compared to the (also digitized) classic data of Nezu and Rodi (1986).

The main differences occurring between the rougher case study of Cameron et al (2017) and the classic of Nezu and Rodi (1986) is comprised to the region closest to the wall ( $z/\delta < 0.2$ ). When the vertical coordinate gets away from source of turbulence production (i.e., the wall) the profiles match reasonably.

Krogstad and Antonia (1999) investigated experimentally the effects of surface roughness on a turbulent boundary layer. Krogstad and Antonia (1999) compared two different rough walls with measurements of a smooth wall. Both rough walls were selected such that the mean velocity profile resulting was the same. They observed that the roughness effects are not confined to the wall region. The turbulent energy production and the turbulent diffusion were found to be significantly different and the diffusion even showed opposite signs at the middle of the boundary layer thickness. Also, differences in terms of velocity spectra were observed despite the mean energy dissipation resulted to be insensitive.

Antonia and Krogstad (2001) kept on with the study of differences induced by different types of roughness which induce the same mean velocity profile but result in different turbulence anisotropy (lower) and observed that larger differences occur for the wall-normal velocity fluctuations.

Despite many advances done during the last decade, Jiménez (2004) probably constitutes the most detailed rough boundary layer review. Jiménez (2004) analysed the available experimental evidences and concluded that the roughness Reynolds number  $k_s^+$  and the ratio of boundary layer thickness to the roughness height are the two parameters of utmost importance.

Leonardi et al (2007) studied the difference between d-type and k-type roughness, concluding that the main difference corresponds to how the frictional and the pressure drag contribute to the total stress.

More recently, the review on turbulent boundary layers of Marusic et al (2010) presented some new ideas and highlighted the unresolved key challenges: scaling, physical understanding, experimental techniques and numerical simulations. When it comes to the roughness effect, Marusic et al (2010) indicated that recent experiments are pointing on the direction of a more complex effect of the roughness towards the flow structure than it has been understood by classic literature. It was mentioned that roughness exerts some effect up to three times its height.

#### *1.4.2.3 Experimental best practices*

Literature related to instrumentation performance, scale effects and wall effects have been studied in order to provide some insight on some relevant experimental settings which could have remained unclear or obscure and still effect the accuracy of the project's final output.

Concerning instrumentation limitations and post-processing techniques, the gross part of the reviewed literature is related to Acoustic Doppler Velocimetry (ADV) data filtering. When it comes to ADV filtering, the most widely used approach is probably the one presented by Goring and Nikora (2002) and its later correction of Wahl (2003). The method proposed by Goring and Nikora (2002) is based on the assumption that the velocity fluctuations and its two first order derivatives may be comprised within an ellipsoid when plotted in three dimensional space. After removing the detected outliers, a spike replacement approach is necessary before iteratively starting a new round of signal despiking. Wahl (2003) presented minor modifications which would make the prior method more consistent and robust and would eliminate the need to proceed iteratively over the velocity signal.

A different approach to ADV data post-processing is the one presented by Hurther and Lemmin (2001). Their study investigate how, by producing one redundant velocity measurement, the noise spectra can be induced and subsequently subtracted from all the other velocity estimations.

One big drawback of ADV is its inability to make velocity estimations even for low air concentrations (see study of Frizell 2000). Under aerated conditions, optical fibre or conductivity probes become the best choice.

Another remarkable study is that of Koca et al (2017) which investigated the effect of a solid contour on the ADV signal. Koca et al (2017) found little improvement by using approach of Hurther and Lemmin (2001); however they noticed that only some of the bins of the ADV are to be considered in order to produce reliable flow properties estimations, i.e.: sweet spot (close to the centre bin of the profile) +/- 8 bins to ensure < 10% error in the mean velocity estimation, +/- 4 bins for < 10% error in the turbulence kinetic energy estimation and +/- bin for the estimation of the power spectra fulfilling -5/3 Kolmogorov decay.

Concerning scale effects, special interest has been put on the effect of aeration as it is probably the most restrictive factor to be scaled. The literature studied is not excessively optimistic (see Felder and Chanson, 2009; Heller, 2011, Pfister and Chanson, 2012) being probably the recent study Felder and Chanson (2017) which suggests that even for large scale prototype structures some of the flow variables are not fully scale independent.

Additionally to the other issues reviewed which may affect the experimental results accuracy, when estimating the friction factor of the stepped geometry it is usually also implicitly accounted for the effect of the glassed walls of the chute as it is only obtained the overall friction factor. This would directly imply that the same two experiments conducted with two different widths would result in two completely different bed friction factor estimations. This may partially explain the large scatter commented on friction factor estimation on stepped spillways observed by Felder and Chanson (2015). In this regard the most interesting approach found in literature is the one presented by Guo (2014). This approach is based on the Einstein (1934; 1948) sidewall correction but despite the latter, it derives an explicit expression based on the Lambert function which is easy to use. It subtracts the glass sidewall effect from the total friction factor; consequently isolating the bed friction factor.

## 1.5 Cooperation with other institutions

As part of WP1 and WP2 no cooperation with other institutions were initiated. For WP3 the tests were conducted at the Forschungszentrum Küste (FZK). The GWK tests in WP3 were closely planned and executed together with FZK employees.

## 2 Project results: Work Package 1 and 3

### 2.1 Experimental setups

To study the wave run-up and overtopping of stepped revetments, three sets of wave flume experiments were conducted. The first two sets were investigated in small scale and focussed on a general understanding of the wave run-up process on stepped revetments with variable cross-sections. In the final setup, large scale model tests were performed to establish whether the results of the small scale tests are affected by substantial scale effects.

#### 2.1.1 WKS dataset

The physical model tests conducted in the Schneiderberg wave flume (WKS) at the Ludwig Franzius Institute. The flume is 110 m long, 2.2 m wide and 2 m deep with a maximum operational depth of 1.2 m. Waves were generated with a piston type wave maker with a total stroke of 0.6 m and a maximum velocity of 1.2 m/s. At a distance of 75 m from the wave maker, the flume was divided in three parallel sections over a distance of 11 m, each with a width of 0.7 m. The model sections had different slopes (1V:1H; 1V:2H; 1V:3H) but the same step height. Two configurations were tested, the first with step heights of  $S_h = 0.05$  m and the second with  $S_h = 0.30$  m. Figure 2.1 shows a side view of the model setups. Additionally, a third configuration was tested with smooth slopes to serve as reference case. Further details on the model setups are described in Kerpen (2017).

The surface elevation was measured by an array of 3 ultrasonic sensors with an additional sensor at the toe of each of the model sections. Resistance wave gauges, each 1 m in length, were installed to measure wave run-up. An overtopping container was placed behind all three of the model sections in which overtopped water was collected and measured with load cells. Wave induced pressures were measured on the 1V:2H slopes, see Figure 2.2 for their locations.

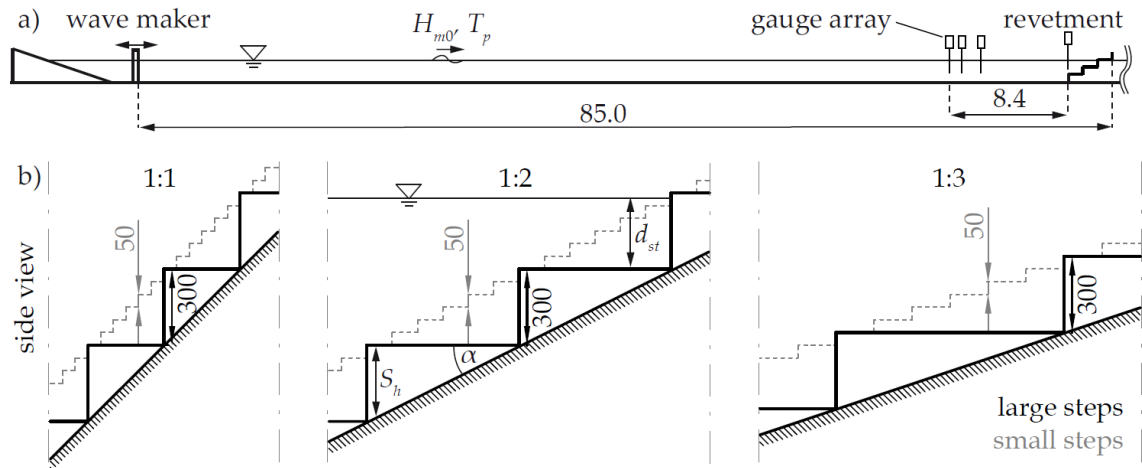


Figure 2.1. Side view of model setup for the WKS dataset. Three different slopes (1V:1H; 1V:2H; 1V:3H) and two step heights ( $S_h=0.05; 0.3$  m) were tested. (Kerpen et al. 2019)

An overview of the test condition ranges is given in Table 2.1. The generated spectra was selected to represent North Sea wave conditions and therefore JONSWAP spectra with a peak enhancement factor of 3.3 were selected. To be statistically reliable, at least 1000 waves were generated for each test. Both breaking and non-breaking waves ( $1.6 \leq \xi_{m-1,0} \leq 7.7$ ) were tested and a wide range of step ratios considered.

Table 2.1. Overview of test conditions for the WKS dataset

Parameter	Symbol	Value	Unit
Wave height	$H_{m0}$	0.06-0.30	m
Peak wave period	$T_p$	1.1-2.9	s
Spectral wave period	$T_{m-1,0}$	1.3-2.1	s
Water depth	$d$	0.92-1.10	m
Step height	$S_h$	0.05; 0.3	m
Slope angle	$\alpha$	45.00; 26.57; 18.43	degrees
Freeboard	$R_c$	0.12-0.30	m
Wave steepness	$s_{m-1,0}$	0.020-0.07	-
Surf similarity	$\xi_{m-1,0}$	1.6-7.7	-
Step ratio	$H_{m0}/S_h$	0.2-4.0	-
Relative freeboard	$R_c/H_{m0}$	0.85-4.50	-

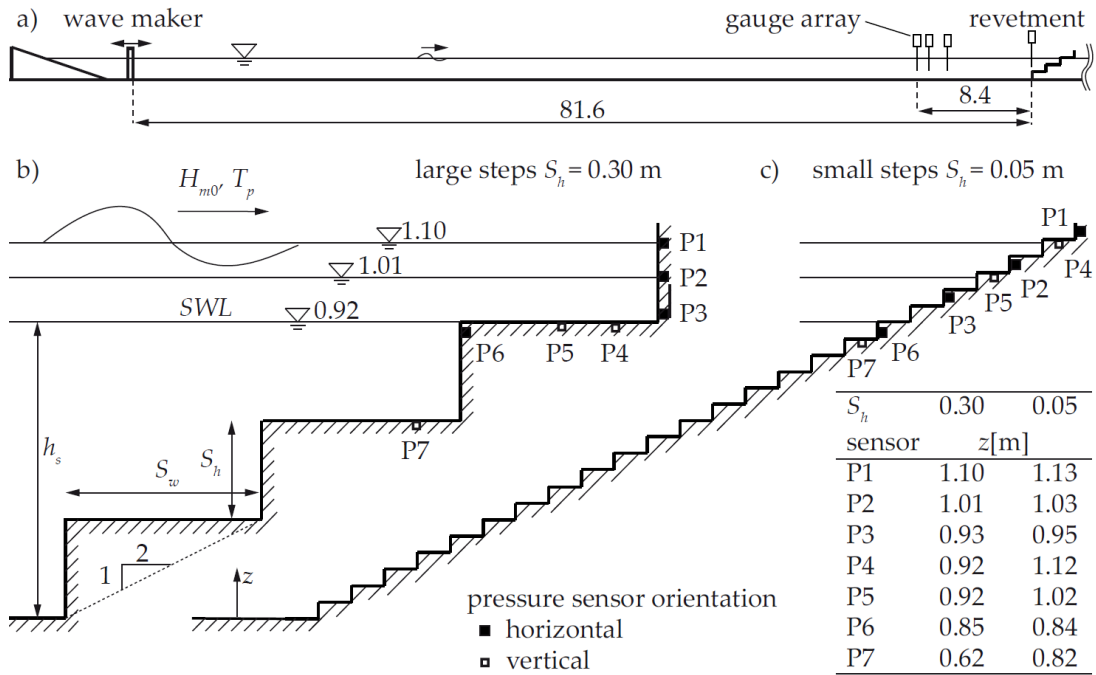


Figure 2.2: Side view of model setup for the WKS dataset with indication of pressure transducer locations. (Kerpen et al. 2018)

### 2.1.2 1V:6H dataset

Previous studies on stepped revetments focused exclusively on steeper stepped slopes ranging from 1V:0.58H (Gallach Sanchez 2018) to 1V:4H (Takayama et al. 1982), but mostly slopes of 1V:2H or 1V:3H (e.g. Van Steeg et al. 2018) were studied. To resemble a typical seaward dike slope along the German coast, it was decided to also study a gentler stepped revetment with a 1V:6H slope. In addition, results for a gentler slope provide valuable theoretical insights in terms of a global system understanding of the wave processes.

The physical model tests were also conducted in the Schneiderberg wave flume (see Section 2.1.1). The model was placed at a distance of 73 m from the wave maker and was constructed from premanufactured frames and step elements that stretched across the flume width. The structure consisted of a total of 24 steps elements, each with a step height ( $S_h$ ) of 0.05 m and a step width of 0.30 m (Figure 2.3).

The surface elevation was measured with ultrasonic sensors (USS) at four locations to determine the incident and reflected wave conditions (Figure 2.4). Water that overtopped the structure crest enters the overtopping container via a 0.7 m wide chute. The overtopping container consisted of an inner and outer shell. A load cell, placed underneath the inner shell, was installed to measure the time series of the wave overtopping. Furthermore, a pump discharged the overtopped water in the event that the overtopping container reached its capacity. A trigger signal was recorded to determine the time intervals for which the pump was running.

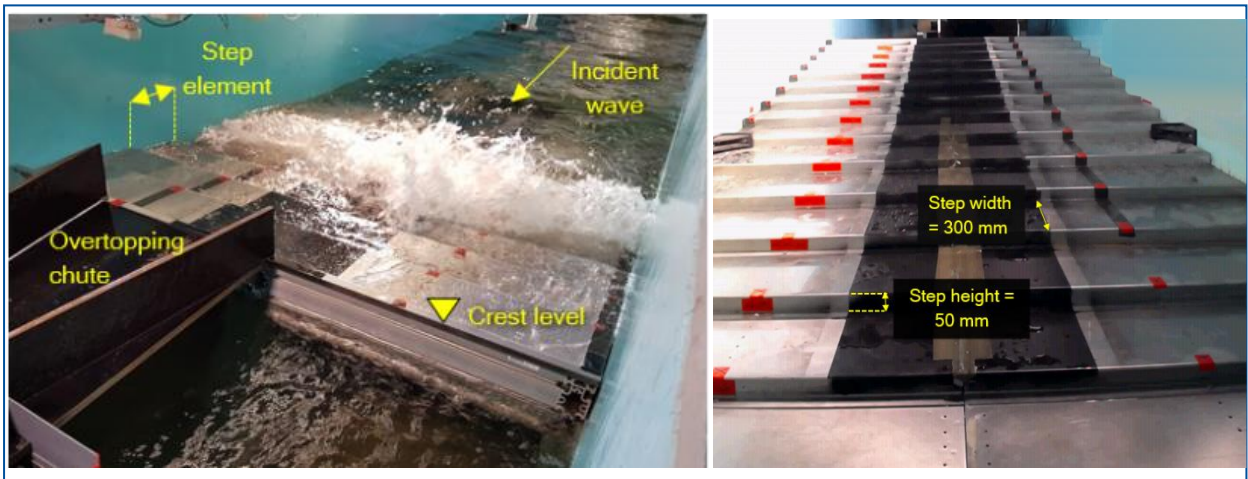


Figure 2.3: Experimental setup for the 1V:6H stepped revetment in the Schneiderberg wave flume (Schoonees et al. 2018)

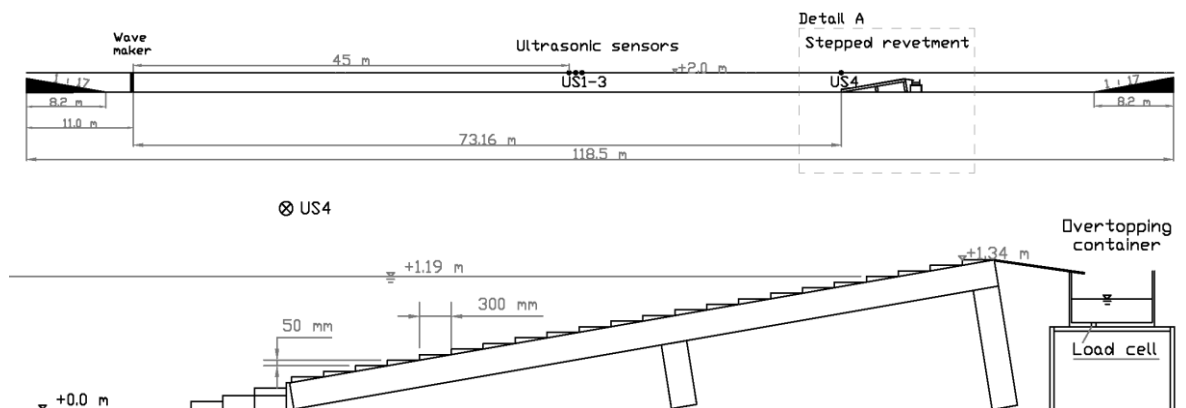


Figure 2.4: Side view of modelled stepped revetment with 1V:6H and step heights  $S_h$  of 0.05 m (Schoonees et al. 2018)

Waves were generated with a standard JONSWAP spectrum with a test duration of minimum 1000 waves (based on 1000 times the peak period,  $T_p$ ). The ranges of test conditions are given in Table 2.1. Due to the gentle slope of 1V:6H, all test conditions result in plunging waves ( $\xi_{m-1,0} < 1.8$ ).

Table 2.2. Overview of test conditions for the 1V:6H dataset

Parameter	Symbol	Value	Unit
Wave height	$H_{m0}$	0.16-0.23	m
Peak wave period	$T_p$	1.86-3.03	s
Spectral wave period	$T_{m-1,0}$	1.75-2.75	s
Water depth	$d$	1.14-1.19	m
Step height	$S_h$	0.05	m
Slope angle	$\alpha$	9.46	degrees
Freeboard	$R_c$	0.15-0.20	m
Wave steepness	$S_{m-1,0}$	0.023-0.044	-
Surf similarity	$\xi_{m-1,0}$	0.79-1.08	-
Step ratio	$H_{m0}/S_h$	3.10-4.62	-
Relative freeboard	$R_c/H_{m0}$	0.73-1.04	-

### 2.1.3 GWK dataset

Model tests were conducted in the Large Wave Flume (GWK) of the Coastal Research Centre (FZK) in Hannover. The aim of the large scale tests was to investigate the influence of scale effects. The flume is 307 m long, 5 m wide and 7 m deep, with a maximum operational water depth of 5m. Regular waves, soliton and wave spectra can be generated with a piston type wave maker equipped with active wave absorption.

Two model configurations were tested; namely, Config. 1 with 13 large steps ( $S_h = 0.50$  m) and Config. 2 with 33 small steps ( $S_h = 0.17$  m). By testing two step heights, a wide range of step ratios ( $H_{m0}/S_h$ ) could be tested, which was identified as a key parameter influencing the wave overtopping and wave impacts on stepped revetments (Van Steeg et al. 2018; Kerpen et al. 2019). The model configurations were constructed of precast concrete step elements and placed on an under layer of gravel that covered a sand-filled core. Both are constructed to a slope of 1V:3H and stretch across the flume width.

Figure 2.5 shows the full scale models of the stepped revetments as tested in the GWK.

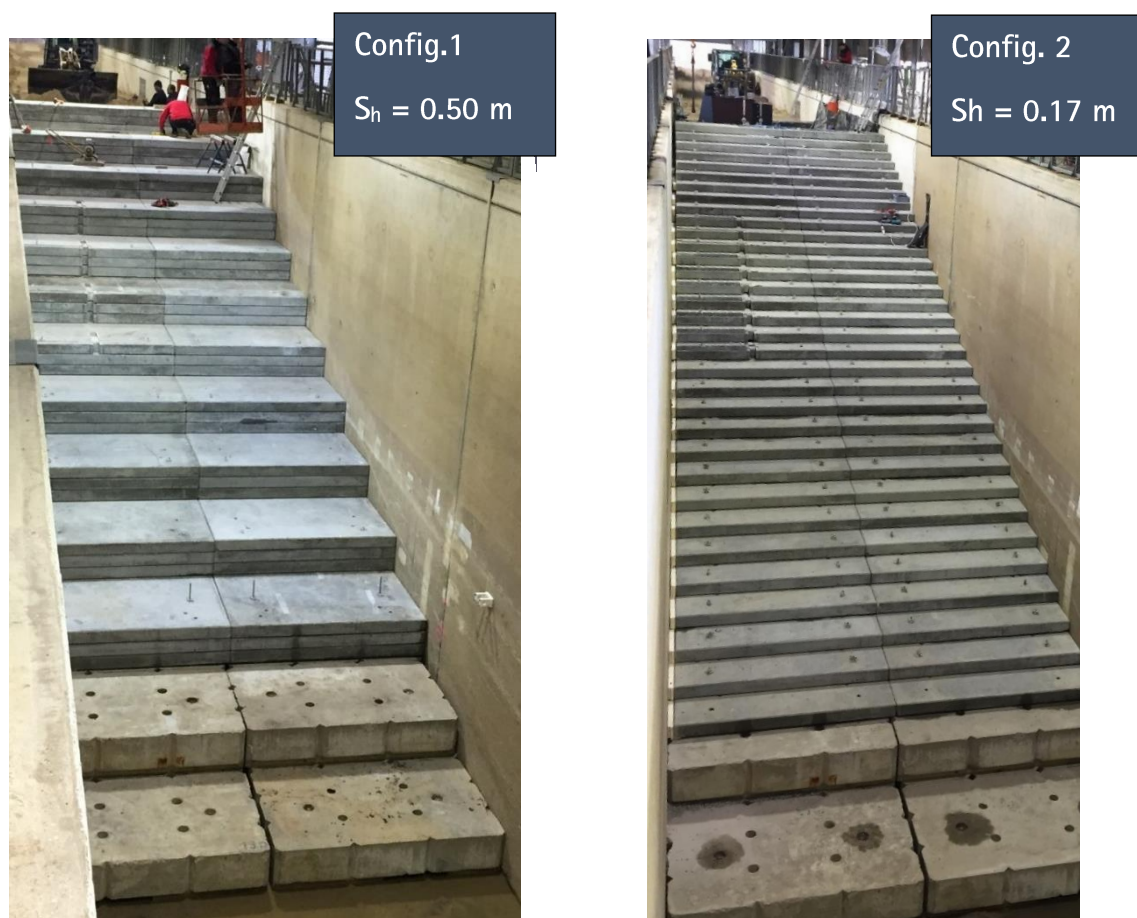


*Figure 2.5: Setup of the two model configurations in the GWK*

The models were placed at a distance of 210.8 m from the wave maker. Resistance wave gauges measured the surface elevation at nine positions along the flume. The first array of wave gauges, consisting of four gauges (WG 1.1 to WG 1.4), was installed between 50 to 60 m from the wave maker, while another four (WG 2.1 to 2.4) were installed between 160 to 170 m from the wave board. The last wave gauge, WG 9, was placed at the toe of the structure. For the two arrays of wave gauges the incident and reflected wave conditions could be calculated offshore and close to the structure. Figure 2.6 indicates the position of the wave gauges and the model.

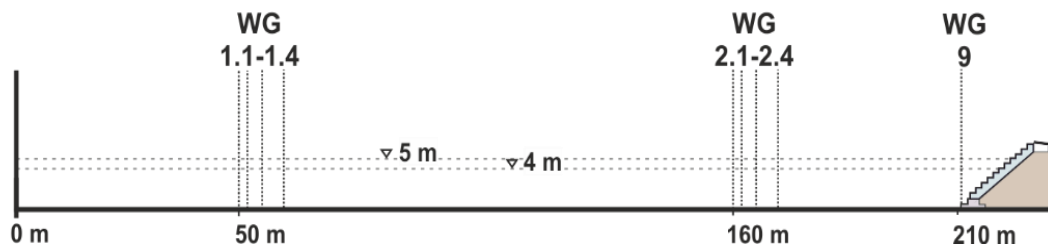


Figure 2.6: Side view of flume: wave gauge and model positions

Figure 2.7 and Figure 2.8 schematically show the instrumentation and model stepped revetments for Configuration 1 and Configuration 2, respectively. Two video cameras were used as visual documentation of all conducted tests. The surface elevation, and thus the wave run-up profiles, were measured in real time by a 2D laser scanner (Sick scanner in Figure 2.7 and Figure 2.8). Pressure sensors were employed on the stair treads (horizontal surface) and risers (vertical surface) just below the 4 m water level up to the 5 m water level. For Configuration 1, a total of 15 pressure sensors were employed, measuring pressures by two upwards-facing pressure sensors and three forward-facing pressure sensors per step. Due to the smaller steps in Configuration 2, only one forward-facing and one upwards-facing pressure sensor were employed. Furthermore, velocities along the steps were measured by 6 velocity probes.

Water that overtopped the crest of the structure was discharged by a channel into a container. The container was placed on four load cells that measured the overtopping throughout the test. Two pumps were installed to discharge the water in the event that the container reached its capacity. A trigger signal was recorded to determine the time periods that the pumps were running.

An overview of the test conditions is presented in. For this data set also standard JONSWAP spectra of minimum 1000 waves were generated. Mainly two water levels (approx. 4 m and 5 m) were simulated for these tests. With the lower water level, the focus was placed on measuring the wave run-up and wave impacts on the stepped revetments, whereas wave overtopping was the main focus with the higher water level.

Table 2.3. Overview of test conditions for the GWK dataset

Parameter	Symbol	Value	Unit
Wave height	$H_{m0}$	0.3-1.0	m
Peak wave period	$T_p$	2.7-7.1	s
Spectral wave period	$T_{m-1,0}$	2.1-6.4	s
Water depth	$d$	4.02-5.06	m
Step height	$S_h$	0.17; 0.50	m
Slope angle	$\alpha$	18.43	degrees
Freeboard	$R_c$	1.5-2.5	m
Wave steepness	$S_{m-1,0}$	0.014-0.035	-
Surf similarity	$\xi_{m-1,0}$	1.9-2.6	-
Step ratio	$H_{m0}/S_h$	0.9-6.2	-
Relative freeboard	$R_c/H_{m0}$	8.3-1.5	-

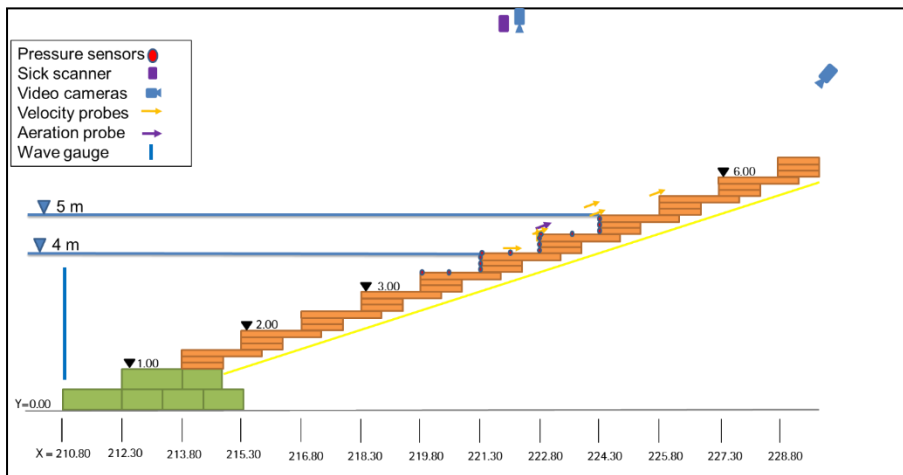


Figure 2.7: Instrumentation overview for Config. 1

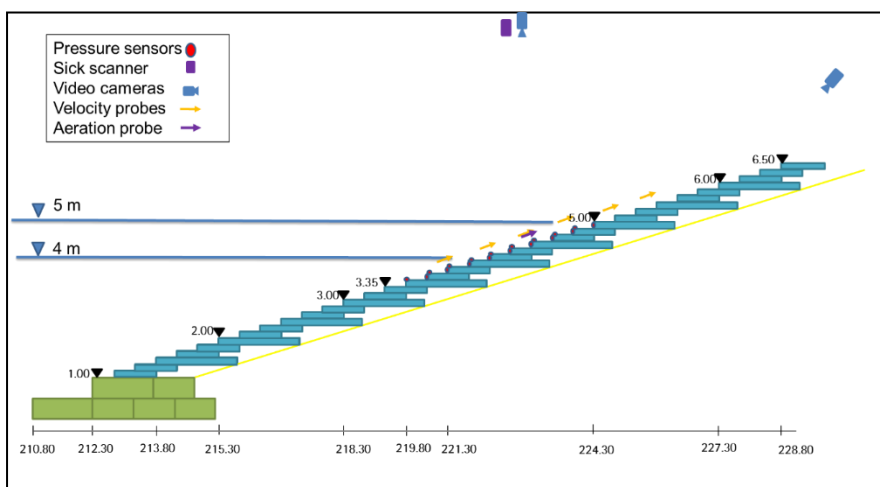


Figure 2.8: Overview of instrumentation for Config. 2

## 2.2 Wave run-up

### 2.2.1 Background

The vertical distance between the still water level (SWL) and the highest point to which a wave runs up a slope, is known as the wave run-up height. Most commonly the wave run-up height exceeded by 2% waves ( $R_{u2\%}$ ) was considered in the crest level design of dikes or coastal embankments (EurOtop 2018). Recent designs are more often based on allowable wave overtopping rates, thus making wave run-up predictions less important in engineering practice. Nevertheless, important insights on a structure's performance can be gained from investigating and understanding the wave run-up process. The  $R_{u2\%}$  also gives an indication of the percentage of waves that will overtop the structure (EurOtop 2018) and can be used to better plan structure maintenance and ensure public safety in the case of accessible structures such as stepped revetments.

EurOtop (2018) gives the following prediction for wave run-up on a slope:

$$\frac{R_{u2\%}}{H_{m0}} = 1.65 \cdot \gamma_b \cdot \gamma_f \cdot \gamma_\beta \cdot \xi_{m-1,0} \quad (2.1)$$

with a maximum of:

$$\frac{R_{u2\%}}{H_{m0}} = 1.00 \cdot \gamma_{fsurging} \cdot \gamma_\beta \cdot \left(4.0 - \frac{1.5}{\sqrt{\gamma_\beta \cdot \xi_{m-1,0}}}\right) \quad (2.2)$$

$$\gamma_{fsurging} = \gamma_f + (\xi_{m-1,0} - 1.8) \cdot (1 - \gamma_f) / 8.2 \quad (2.3)$$

in which  $\gamma_b$  is the influence factor for a berm,  $\gamma_f$  is the influence factor for roughness and  $\gamma_\beta$  is the influence factor for oblique wave attack. In this project perpendicular waves were considered and no berm was present, therefore  $\gamma_b = \gamma_\beta = 1$ . The influence factor for roughness quantifies the reduction in wave run-up due to slope roughness, thus for a smooth slope  $\gamma_f = 1$ . A higher influence factor for roughness,  $\gamma_{fsurging}$ , applies for surging wave conditions ( $\xi_{m-1,0} > 1.8$ ) as the run-up reduction due to roughness becomes less effective with increasing surf similarity. From  $\xi_{m-1,0} = 1.8$  to  $\xi_{m-1,0} = 10$  the influence factor for roughness increases linearly up to  $\gamma_f = 1$ .

The steps of stepped revetments act as roughness elements that induce turbulence and dissipate energy. The reduction in wave run-up heights at stepped revetments can thus be quantified with the factor  $\gamma_f$ . The aim of measuring the wave run-up was to determine the magnitude of  $\gamma_f$  to be applied in Equations (2.1) to (2.3) to predict wave run-up heights for stepped revetments.

## 2.2.2 Measurements and data analysis

The measurement of wave run-up on a stepped revetment proved to be more challenging than on a smooth slope where maximum wave run-up heights are easier distinguishable. As waves run up a stepped slope, frequent splash ups occur as waves interact with the step risers, thus making it difficult to determine accurate wave run-up heights. It is more prevalent for larger step heights ( $H_{m0} < S_n$ ) as the behaviour is analogues to vertical walls at which run-up measurements is not meaningful.

In the WKS dataset wave run-up was measured by wave gauges. For the small steps ( $S_n = 0.05$  m), the wave gauges were placed inclined following the structure slope, thus measuring the wave run-up at the step edges. For the large steps ( $S_n = 0.3$  m) the wave gauges were placed in a vertical position parallel to the step risers. This posed some difficulty as the gauges were unable to measure the run-up right against the step riser, with the implication that run-up heights could be slightly underestimated. Spikes from the measurements were removed by applying a second order polynomial Savitzky-Golay smoothing filter (Kerpen 2017). The wave run-up height was determined for every incident wave and only tests consisting of more than 1000 waves were considered in calculating the  $R_{u2\%}$ . Visual validation confirmed that the wave run-up heights were of sufficient accuracy.

In the GWK the wave run-up profile over the stepped revetment was measured by a 2D laser scanner at a sampling rate of 25 Hz. As for the WKS dataset, the measurements are influenced by splash ups as waves interact with step risers. To eliminate the effects of splashes, the run-up height was determined by applying a moving median filter for each time step across each revetment step. Subsequently the highest run-up height for each wave was determined based on the median water-level across each step. Visual validation was used to verify the reliability of the applied data processing.

Incident wave conditions ( $H_{m0}$ ;  $T_{m-1,0}$ ) for all datasets were determined by employing the *WaveLab* software, developed by the Aalborg University, Denmark.

## 2.2.3 Results and discussion

The wave run-up measurements for the WKS and the GWK datasets are presented in Figure 2.9(a) and (b), respectively. The relative wave run-up ( $R_{u2\%}/H_{m0}$ ) is plotted against the surf similarity ( $\xi_{m-1,0}$ ) with reference

lines of the EurOtop (2018) empirical predictions for a smooth ( $\gamma_f = 1$ ) and rough slopes ( $\gamma_f = 0.3$ ;  $\gamma_f = 0.6$ ;  $\gamma_f = 0.7$ ). The transition from plunging to surging wave conditions is indicated at  $\xi_{m-1,0}=1.8$ . It can be observed from both datasets that stepped revetments effectively reduce wave run-up when compared to a smooth slope as the data points fall well below the  $\gamma_f = 1$  prediction.

The WKS dataset covers a large range of surf similarities ( $1.65 \leq \xi_{m-1,0} \leq 7.68$ ). In general the relative run-up increases with increasing surf similarity. As described by Kerpen (2017), the step ratio ( $H_{m0}/S_h$ ) substantially influence the stepped revetment's performance. In Figure 2.9(a) it can be seen that cases with smaller step ratios ( $H_{m0}/S_h < 1$ ) in the range  $0.26 \leq H_{m0}/S_h \leq 0.78$  have an estimated  $\gamma_f$ -value of 0.6. These data points correspond to the tests conducted with  $S_h=0.3$  m. The large steps are thus less effective in reducing wave run-up when compared to the test conducted with small steps ( $S_h=0.3$  m;  $H_{m0}/S_h \geq 1$ ). When the wave height is equal or larger than the step height, the structure more effectively reduce the wave run-up height ( $1.5 \leq H_{m0}/S_h \leq 3.2$ ) and has an approximate  $\gamma_f$ -value of 0.3.

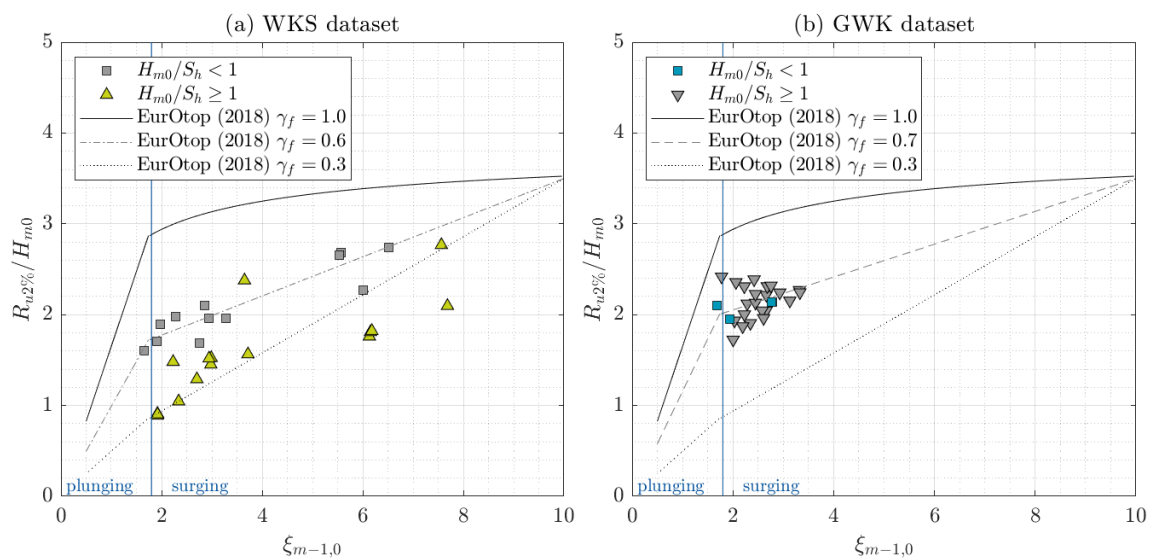


Figure 2.9. Wave run-up results of the (a) WKS and (b) GWK datasets. The wave run-up predictions as given in EurOtop (2018) for a smooth slope ( $\gamma_f = 1$ ) and rough slopes ( $\gamma_f = 0.7$ ;  $\gamma_f = 0.6$ ;  $\gamma_f = 0.3$ ) are given as reference.

The large scale test data in Figure 2.9(b) show that most data points are between  $\gamma_f = 0.6$  and 0.8, thus showing that the stepped revetment is less effective in wave run-up reduction than is suggested by the small scale data. Only three tests were conducted with smaller step ratios ranging between  $0.89 \leq H_{m0}/S_h \leq 0.94$  and fall closely around a  $\gamma_f$ -value of 0.7. For the larger step ratios ranging from ( $1.5 \leq H_{m0}/S_h \leq 5.2$ ), the data points scatter around a  $\gamma_f$ -value of 0.7. Consequently, the results from the large-scale data do not show a clear distinction between the different ranging of step ratios as has been identified by the WKS dataset in Figure 2.9(a).

## 2.2.4 Conclusions

Relative wave run-up for stepped revetments increases with increasing surf similarities. Compared to a smooth slope, step revetments effectively reduce wave run-up heights. Based on the WKS dataset, a reduction in relative wave run-up between 40 % ( $H_{m0}/S_h \geq 1$ ) and 70 % ( $H_{m0}/S_h < 1$ ) can be achieved. The GWK dataset shows only an approximate reduction of 30 % for all step ratio ranges. The differences between the WKS and GWK datasets can partly be attributed to different measurement techniques and partly to scale effects. Based on findings by Stoa (1978) wave run-up heights tend to be underestimated in small scale. It is thus recommended that a  $\gamma_f = 0.7$  is applied in Equations (2.1) to (2.3) to predict the wave run-up of step revetments with step ratios in the range of ( $0.89 \leq H_{m0}/S_h \leq 5.2$ ). It should also be noted that for surging waves ( $\xi_{m-1,0} > 1.8$ ), the reduction in run-up becomes less and Equation (2.3) for

$\gamma_{f,surg}$  applies. At a  $\xi_{m-1,0}=10$  it is expected that slope roughness no longer reduce wave run-up when compared to smooth slope and  $\gamma_{f,surg}$  becomes 1 (EurOtop 2018).

## 2.3 Wave overtopping

### 2.3.1 Background

When wave run-up heights exceed a structure's freeboard, water is discharged over its structure. The water that passes over the structure's crest due to wave action, is known as wave overtopping and is measured in m<sup>3</sup>/s per m of structure crest. The wave overtopping of a structure is key in determining its crest level as it gives the average volume of water discharged over a structure's crest, as opposed to wave run-up heights which only give a crest level height exceeded by 2% of waves. Additionally, in the case of stepped revetments, the measurement of wave overtopping volumes in the laboratory is arguably easier and more accurate. The primary focus of project waveSTEPS was thus in determining wave overtopping rates for stepped revetments.

The latest guidelines for predicting wave overtopping for slopes or embankments as given in EurOtop (2018) are:

$$\frac{q}{\sqrt{g \cdot (H_{m0})^3}} = \frac{a}{\sqrt{\tan\alpha}} \cdot \gamma_b \cdot \xi_{m-1,0} \cdot \exp \left[ - \left( b \frac{R_c}{\xi_{m-1,0} \cdot H_{m0} \cdot \gamma_b \cdot \gamma_f \cdot \gamma_\beta \cdot \gamma_v} \right)^{1.3} \right] \quad (2.4)$$

with a maximum of:

$$\frac{q}{\sqrt{g \cdot (H_{m0})^3}} = a \cdot \exp \left[ - \left( b \frac{R_c}{H_{m0} \cdot \gamma_{f,surg} \cdot \gamma_\beta \cdot \gamma^*} \right)^{1.3} \right] \quad (2.5)$$

where  $q$  is defined as the average overtopping discharge [m<sup>3</sup>/(s.m)],  $H_{m0}$  is the spectral significant wave height [m],  $R_c$  is the crest freeboard [m],  $a$  and  $b$  are empirical coefficients,  $\gamma_b$  depicts the influence factor for a berm [-],  $\gamma_f$  is the influence factor for the roughness elements on a slope [-],  $\gamma_\beta$  is the influence factor for oblique wave attack [-],  $\gamma_v$  is the influence factor for a wall at the end of a slope [-],  $\gamma^*$  is a combined factor for all kind of geometrical influences and  $\xi_{m-1,0}$  is the breaker parameter [-].

Only  $\gamma_f$ , the influence factor for the roughness, is considered while  $\gamma_b=\gamma_\beta=\gamma_v=\gamma^*=1$ . As for wave run-up, the slope roughness of a stepped revetment reduce the wave overtopping when compared to a smooth slope. The objective of the overtopping model tests was to determine the  $\gamma_f$  for stepped revetments to be applied in Equations (2.4) to (2.5).

### 2.3.2 Measurements and data analysis

The same measurement techniques and methodology were applied for the WKS, 1V:6H and GWK datasets. JONSWAP spectra with at least 1000 waves were considered in determining average overtopping rates. Time series of load cell measurements were analysed to determine the total volume of water that entered the overtopping container during a test. Additionally the volume of water pumped out during a test was calculated and added. The total volume was then divided by the test duration and the chute width, to determine the average overtopping discharges per m of crest,  $q$ . Also see Kerpen et al. (2019) and Schoonees et al. (2018) for details of the WKS and 1V:6H datasets, respectively.

The incident wave conditions ( $H_{m0}$ ;  $T_{m-1,0}$ ;  $\xi_{m-1,0}$ ) were determined with the *WaveLab* software. As described in Kerpen et al. (2019), reference tests with a smooth slope were conducted to calibrate the empirical coefficients,  $a$  and  $b$ , in Equations (2.4) and (2.5). For the 1V:6H and GWK datasets a calibration was not possible, since no reference tests with smooth slopes were performed and therefore the coefficients as given in EurOtop (2018) were applied. Table 2.4 summarises the empirical coefficients applied in Equations (2.4) and (2.5).

Table 2.4. Empirical coefficients for overtopping prediction

Dataset	cot $\alpha$	$\xi_{m-1,0}$ [-]	$a$ [-]	$b$ [-]	Equation
WKS	1	$> 1.8$	0.08	1.4	(2.5)
WKS	2	$> 1.8$	0.09	1.2	(2.5)
WKS	3	$> 1.8$	0.09	1.3	(2.5)
WKS	3	$< 1.8$	0.023	2.3	(4.1)
1V:6H	6	$< 1.8$	0.023	2.7	(4.1)
GWK	3	$> 1.8$	0.09	1.5	(2.5)

With the measured overtopping rate, wave conditions and freeboard known, the  $\gamma_f$  for stepped revetments can be determined. Note that a distinction is made between tests with plunging or breaking waves, i.e.  $\xi_{m-1,0} \leq 1.8$ , and surging or non-breaking waves i.e.  $\xi_{m-1,0} > 1.8$ . For plunging waves, Equation (2.4) applies, in which the surf similarity also influences the relative overtopping. For surging or non-breaking waves, Equation (2.5) gives the prediction for relative overtopping. The relation between  $\gamma_{f,surging}$  and  $\gamma_f$  is given in Equation (2.3). By rearranging Equations (2.4) and (2.5), the following equations are obtained to determine the influence factors for roughness:

$$\gamma_f = \frac{b \cdot R_c}{\xi_{m-1,0} \cdot H_{m0} \cdot \left[ -\ln\left(\frac{q\sqrt{\tan \alpha}}{a \cdot \xi_{m-1,0} \sqrt{g \cdot (H_{m0})^3}}\right) \right]^{10/13}} \quad (2.6)$$

with a maximum of:

$$\gamma_{f,surging} = \frac{b \cdot R_c}{H_{m0} \cdot \left[ -\ln\left(\frac{q}{a \sqrt{g \cdot (H_{m0})^3}}\right) \right]^{10/13}} \quad (2.7)$$

### 2.3.3 Results and discussion

Breaking wave conditions, where overtopping was measured, only occurred in small scale in the WKS and 1V:6H datasets. Figure 2.10 shows the relative overtopping against relative freeboard for breaking waves. Firstly it can be observed that the relative overtopping decreases for increasing relative freeboards. As no smooth slope tests were available for the 1V:6H dataset, the EurOtop (2018) smooth slope was taken as reference. The best fit smooth slope for the 1V:3H data is also shown in Figure 2.10. Overall, both test series show a decrease in relative overtopping of about 35 % when compared to the smooth slope reference curves. The 1V:3H dataset shows a larger reduction, since its reference curve is higher than the EurOtop (2018) smooth slope prediction. A reduction coefficient of  $\gamma_f = 0.65$  was established for the 1V:6H data.

The wave overtopping caused by surging waves are presented in Figure 2.11 for (a) small scale and (b) large scale tests. The tested stepped revetments for both small and large scale have proven to effectively reduce wave overtopping when compared to the smooth slope best fit curves. However, some data points in Figure 2.11 (a) indicates that in some instances the overtopping for stepped revetments exceed the average overtopping rates for smooth slope. On closer investigation this occurs for large relative freeboards ( $R_c/H_{m0} > 3$ ) and for tests with steeper slopes (1V:1H). In contrast, the 1V:2H and 1V:3H datasets show consistently substantial reductions in wave overtopping discharges.

## Breaking waves

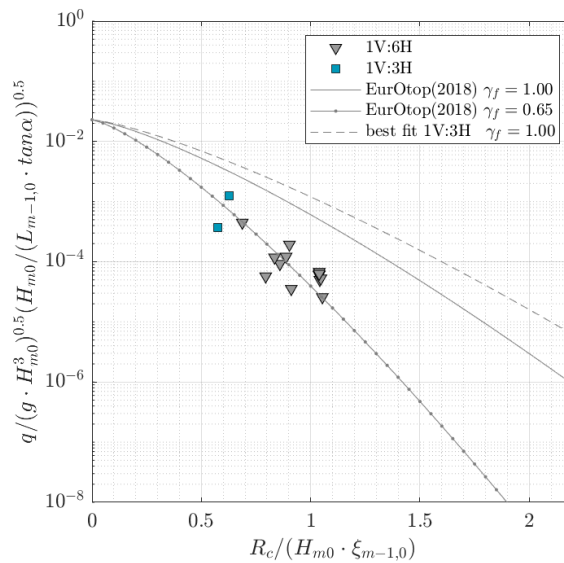


Figure 2.10. Breaking waves: relative wave overtopping against relative freeboard. The calibrated smooth slope curve for 1V:3H and EurOtop (2018) reference curves for  $\gamma_f = 1$  and  $\gamma_f = 0.65$ .

Figure 2.11 (b) displays substantial reductions in wave overtopping for both configurations. The stepped revetment with larger step heights ( $S_h = 0.50$  m) has higher slope roughness, lower overtopping rates and consequently require a lower crest level to ensure coastal safety. Its influence factor for roughness is around  $\gamma_f = 0.5$ . Although less effective in overtopping reduction than the larger steps, the stepped revetment with smaller steps ( $S_h = 0.17$  m) still substantially reduce wave overtopping with a  $\gamma_f = 0.7$ .

As found by Van Steeg et al. (2018) and Kerpen et al. (2019) the step ratio ( $H_{m0}/S_h$ ) also influences a stepped revetment's performance in reducing wave overtopping. By applying Equation (2.6) for breaking waves and Equations (2.7) and (2.3) for surging waves, the corresponding  $\gamma_f$  for each test was calculated. Figure 2.12 presents the  $\gamma_f$  against the characteristic step height ( $\cos\alpha \cdot S_h/H_{m0}$ ) which considers the aspect ratio of the steps and incident wave heights. Figure 2.12 (a) shows  $\gamma_f$  for the small scale datasets, WKS and 1V:6H. An optimum reduction is observed at  $\cos\alpha \cdot S_h/H_{m0} = 1.2$ . The  $\gamma_f$  decreases for increasing characteristic step heights up to  $\cos\alpha \cdot S_h/H_{m0} = 1.2$ , whereas the  $\gamma_f$  increases linearly up to 0.93 at  $\cos\alpha \cdot S_h/H_{m0} = 4.2$ . The corresponding approximate optimal step ratios for different slopes are given in Table 2.5.

Table 2.5. Approximate optimal step ratios based on Figure 2.12(a)

Slope	Optimal $S_h/H_{m0}$
1V:1H	1.18
1V:2H	0.93
1V:3H	0.88

Figure 2.12 (b) shows that the influence factor for roughness for the GWK dataset decrease for increasing characteristic step heights. The prediction derived by Van Steeg et al. (2018), based on tests with stepped revetment slopes of 1V:2H and 1V:3H and  $S_h = 0.023$  and 0.046 m, is given as comparison and is valid for  $0 < \cos\alpha \cdot S_h/H_{m0} < 0.6$ . The prediction shows mainly lower  $\gamma_f$ -values than what was found in both the small and large scale data. It should be kept in mind that the Van Steeg et al. (2018) prediction was developed for the TAW (2002) overtopping formulae and not for the EurOtop et al. (2018) predictions.

A closer look at the roughness factors results, in the range of  $0 < \cos\alpha \cdot S_h/H_{m0} < 0.6$ , is given in Figure 2.13. Except for the outliers from the 1V:1H dataset, the data overall show a decrease in roughness for increasing characteristic step height. Here no distinct scale effects can be identified. Although when comparing the GWK dataset to the prediction by Van Steeg et al. 2018, the roughness factors are underestimated.

### Non-breaking waves

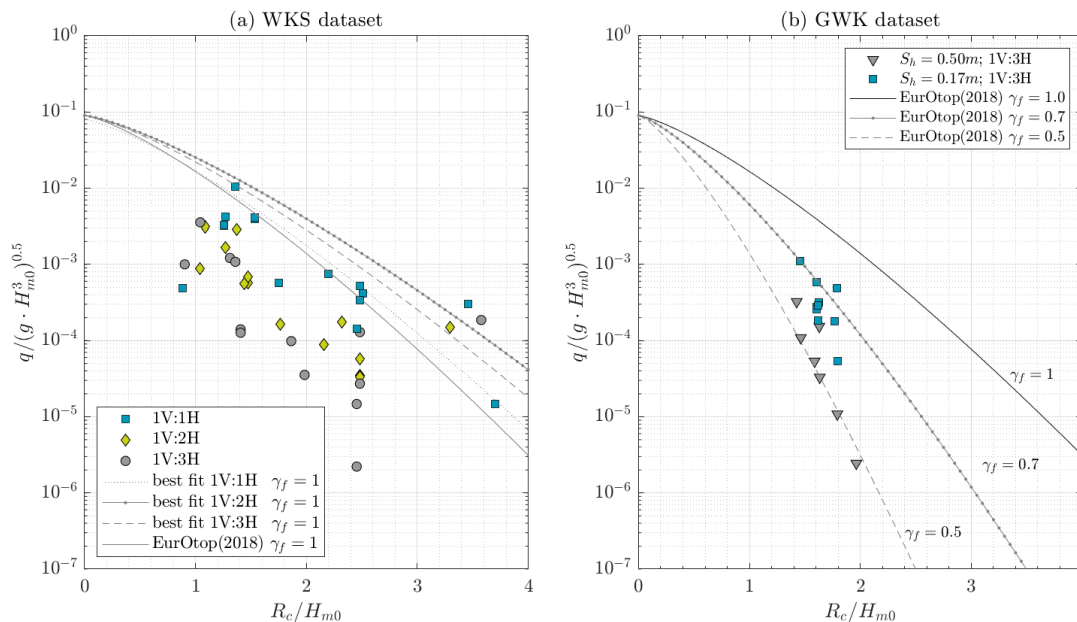


Figure 2.11. Surging waves: wave overtopping results at stepped revetments. The WKS overtopping dataset in (a) shows reference for calibrated smooth slope curves and EurOtop (2018)  $\gamma_f=1$ . In (b) GWK overtopping dataset is shown with reference lines ( $\gamma_f=1$ ;  $\gamma_f=0.7$ ;  $\gamma_f=0.5$ ) of EurOtop (2018).

### 2.3.4 Conclusions

Compared to smooth slopes, stepped revetments effectively reduce wave overtopping for both breaking and non-breaking waves. The reduction in overtopping is quantified by the influence factor for roughness,  $\gamma_f$ . It was established that the  $\gamma_f$  is a function of the characteristic step height ( $\cos\alpha \cdot S_h/H_{m0}$ ). An optimum reduction in wave overtopping of 65 % can be achieved for a characteristic step height of  $\cos\alpha \cdot S_h/H_{m0} = 1.2$ . For the GWK dataset it was found that approximate reductions of  $\gamma_f=0.7$  and  $\gamma_f=0.5$  can be achieved for a stepped revetment with  $S_h=0.17$  m and  $S_h=0.50$  m, respectively.

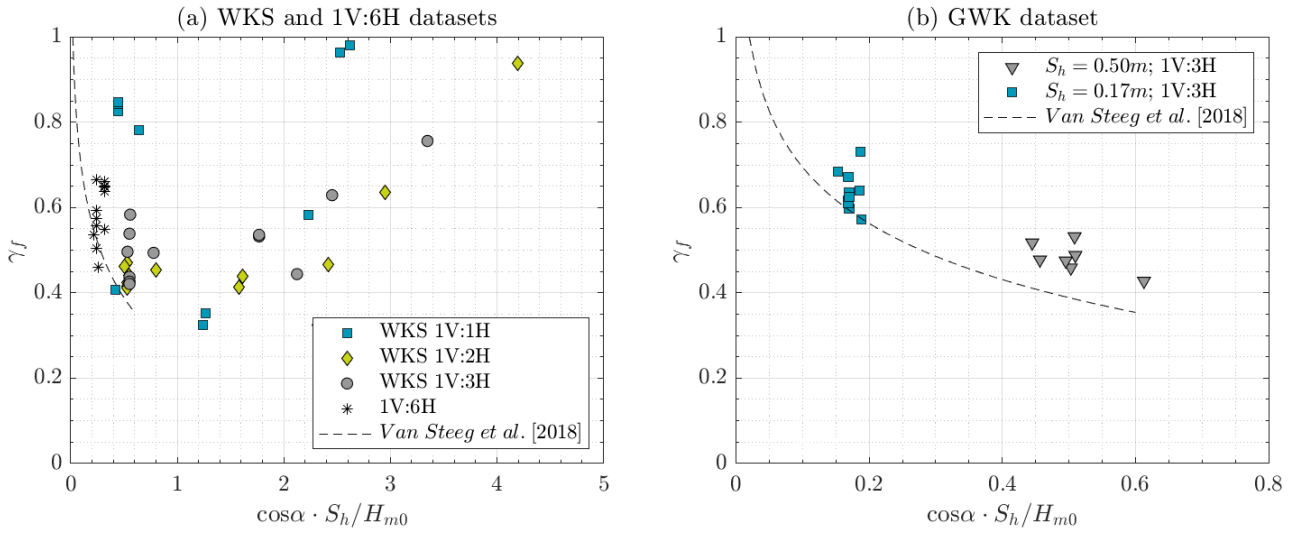


Figure 2.12. Influence factors for roughness for stepped revetments tested in (a) small and (b) large scale. A prediction formula by Van Steeg et al. (2018) for comparison.

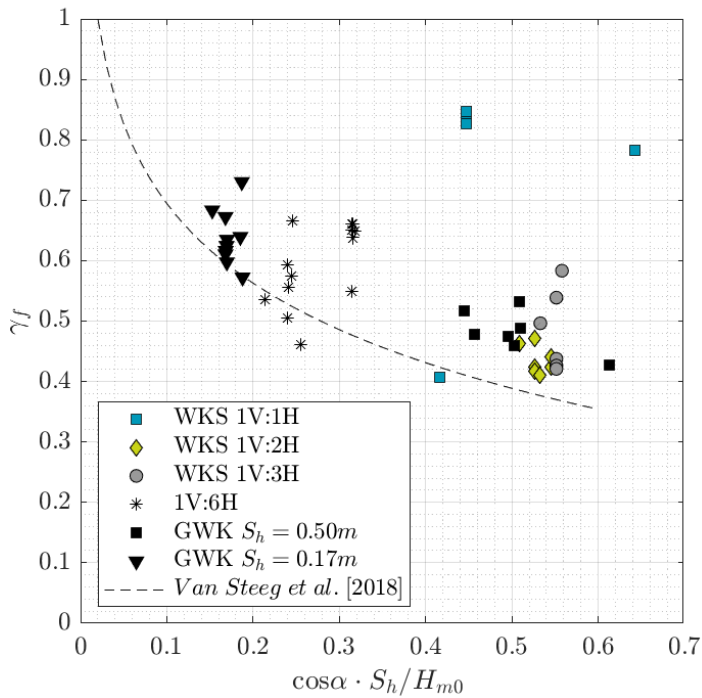


Figure 2.13. Comparison of influence factors for roughness between small and large scale tests

## 2.4 Wave impact pressures

For the WKS dataset wave impacts on horizontal and vertical step fronts of stepped revetments was investigated for step ratios  $0.3 < H_{m0}/S_h < 3.5$  and a revetment slope of 1:2. Details on the pressure measurements and results are given in Kerpen et al. (2018). Führböter (1966), Weggel (1971) and Führböter (1986) found that wave impact pressures on slopes follow a log normal distribution. Figure 2.14 shows the wave pressures the log-normal distribution for test 103 and test 209 for small ( $S_h=0.05$  m) and large step heights ( $S_h=0.3$  m), respectively. Spectral wave heights of  $H_{m0} = 0.084$  m and  $H_{m0} = 0.089$  m (for test 103 and 209, respectively) and a corresponding Iribarren number of  $\xi_{m-1,0} = 2.9$  (2.8 for test 209) were generated. For the small steps ( $H_{m0} > S_h$ ) the pressures closely follow a log-normal distribution. The 10% highest impacts of the larger steps ( $H_{m0} < S_h$ ) are not well presented by a log-normal distribution, as they are substantially higher. This increase in wave impacts for larger steps could be due to the absence of a water layer that dampens the impacts as is the case for smaller steps. Therefore in the case of the larger steps, the wave impact pressures is similar to vertical walls.

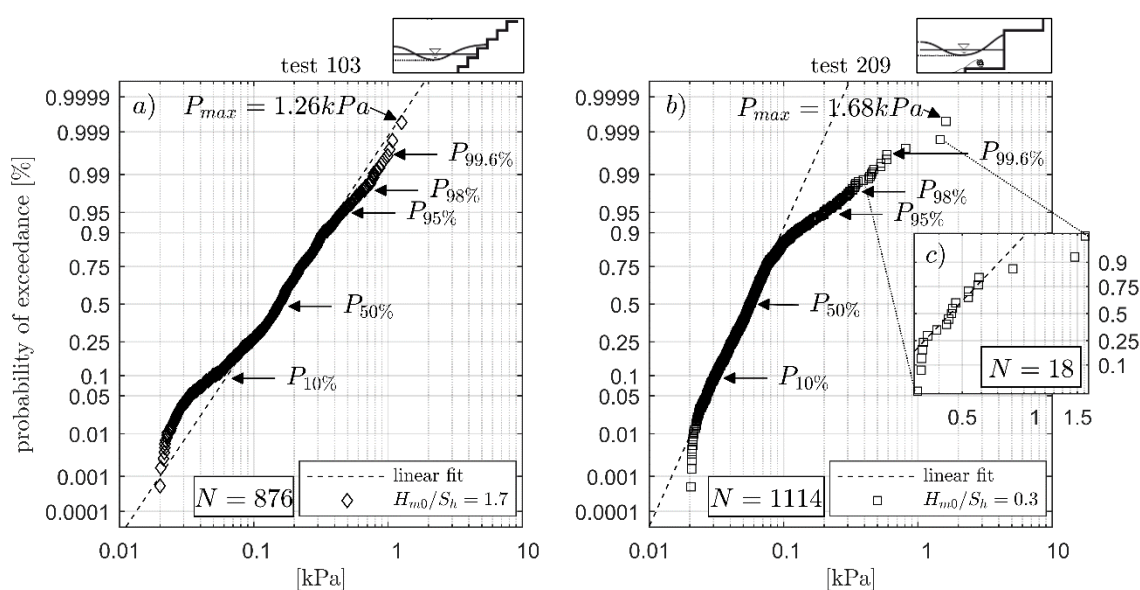


Figure 2.14. Recorded pressure impacts and log-normal probability distributions of the maximum impact pressures for (a) small step heights (test 103,  $H_{m0}/S_h = 1.7$ ) and (b) large step heights (test 209, pressure sensor P2,  $H_{m0}/S_h = 0.3$ ). (c) Gives a detail of the log-normal probability distribution of the 18 largest impacts in test 209 (Kerpen et al. 2018).

Figure 2.15 gives the relative position to the SWL ( $z/H_{m0}$ ) of the maximum pressure impact ( $P_{99.6\%}$ ) normalized by water density  $\rho$ , gravity  $g$ , and spectral wave height. Following Cuomo (2010), the maximum wave impact pressure is described by  $P_{99.6\%}$ . The maximum pressure impacts for both step heights are located close to the SWL Kerpen et al. (2018) derived envelope curves in Equation (2.8) with coefficients  $a$ ,  $b$  and  $c$  in Table 2.6 for the best fit of data (coefficient of determination:  $R^2 = 0.62$ ,  $STD = 0.189$ ). The equation is valid for  $0.01 < P_{99.6\%}/(\rho g H_{m0}) \leq 3.6$ .

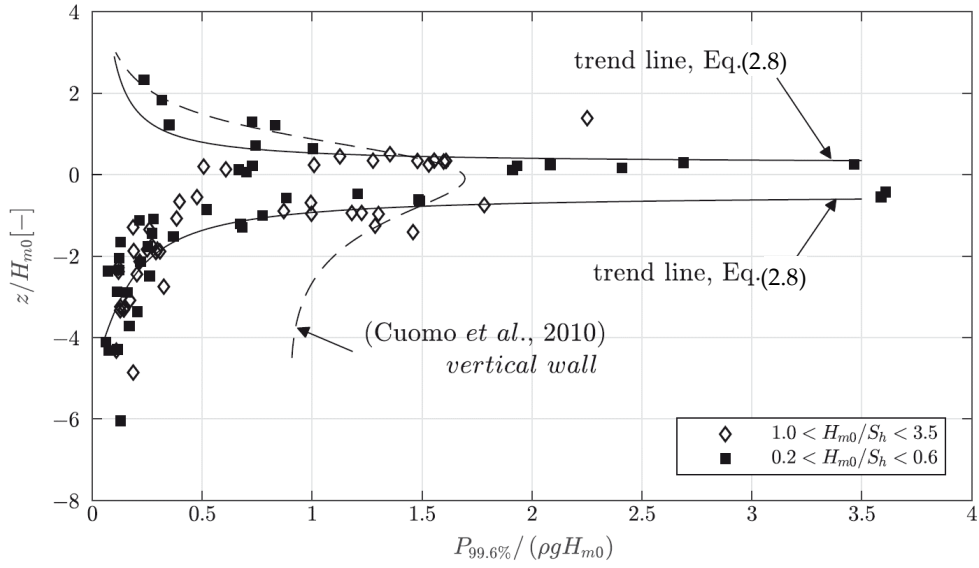


Figure 2.15. Normalized pressure impact relative to the SWL ( $z = 0$ ) for a 1:2 inclined stepped revetment (Kerpen et al. 2018).

$$\frac{P_{99.6\%}}{\rho g H_{m0}} = \min \left\{ \tan \left[ \frac{z/H_{m0} + a}{b} \right] / c, 3.6 \right\} \quad (2.8)$$

Table 2.6. Coefficients  $a$ ,  $b$ , and  $c$  for Equation (2.8).

$z$ (SWL at $z = 0$ )	$a$	$b$	$c$
$z \geq 0$	-1171.64	745.72	-2831.66
$z < 0$	4.97	-2.87	-6.15

## 3 Project results: Work Package 2

### 3.1 Experimental setups, instrumentation and data analysis

#### 3.1.1 Presentation

Three different experimental models have been prepared at the FH Aachen Hydraulics Laboratory, bearing in mind that the final goal of the experimental tests was to disclose the flow structure within stepped revetment cavities, to later properly address the energy dissipation during wave run-up. Additional measurements were conducted together with Leibniz University Hannover to better establish the link between steady and transient flow dynamics over stepped cavities (Section 3.6).

All experimental setups at FH Aachen were installed in a horizontal flume (12 m long, 0.58 m wide) and were partially modified to include additional setups (i.e. two step heights, aerated flows and grass-steps transition). Flow rates were usually increased in steps of 5-10 l/s, which implies that results cluster around the specific flow rates shown in Table 3.1. Different instrumentation was used to study flow depths and velocities. These measurements allow insight on the mean and turbulent behaviour of flows over stepped cavities and yield accurate estimations of energy dissipation.

*Table 3.1. Common flow conditions studied in the setups installed in the horizontal flume of FH Aachen.  $Q$  for the absolute flow rate,  $q$  for the specific flow rate (flow rate per width),  $Re$  for the Reynolds number ( $4q/\nu$ , with  $\nu$  the kinematic viscosity  $1.005 \cdot 10^{-6} \text{ m}^2/\text{s}$ ).*

$Q$ (m <sup>3</sup> /s)	0.020	0.030	0.040	0.050	0.060	0.070	0.080	0.090	0.100
$q$ (m <sup>2</sup> /s)	0.034	0.052	0.069	0.086	0.103	0.121	0.138	0.155	0.172
$Re$ (10 <sup>5</sup> )	1.37	2.06	2.74	3.43	4.12	4.80	5.49	6.18	6.87

#### 3.1.2 Experimental setup

##### *Basic setups*

The main goal of this study was to investigate the flow structure and energy dissipation over three stepped cavity geometries: 1V:2H, 1V:3H, and 1V:6H (Figure 3.1) with 10 cm step height. Additionally, a smaller step size, i.e. 5 cm, was installed for one of the setups (1V:2Hs). The main geometry properties are presented in Table 3.2. Exemplary images of the flows occurring over these geometries are shown in Figure 3.2.

*Table 3.2 Geometrical description of the different cavity geometries studied.*

ID	Horizontal extension (cm)	Vertical extension (cm)	Revetment slope (°)	Number of steps (-)	Extension (m)
1V:2H	20	10	26.57	12	2.68
1V:2Hs	10	5	26.57	23	2.68
1V:3H	30	10	18.43	8	2.53
1V:6H	60	10	6.46	6	3.65

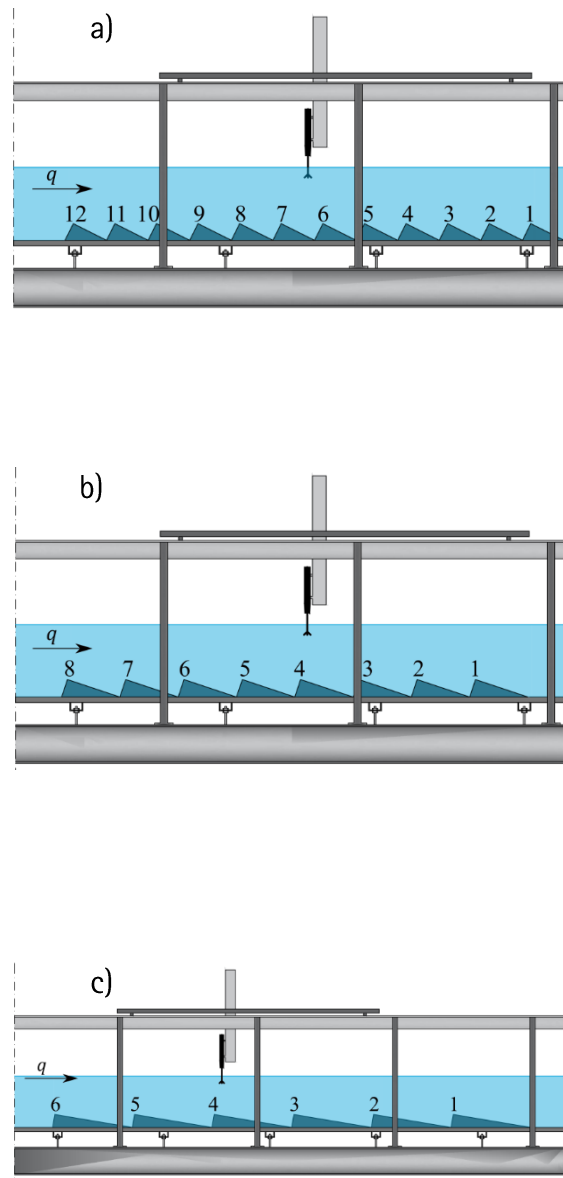


Figure 3.1. Sketch of the different setups conducted at FH Aachen and step numbering: a) model 1V:2H, b) model 1V:3H and c) model 1V:6H (flow from left to right).

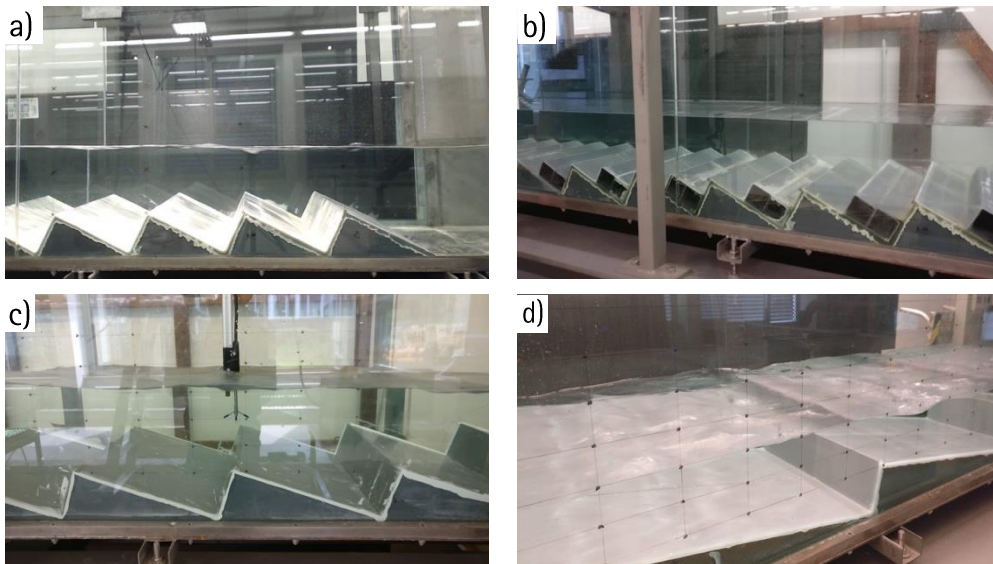


Figure 3.2. Flow over the different studied models: a) 1V:2H, b) 1V:2Hs, c) 1V:3H and d) 1V:6H (flow from left to right).

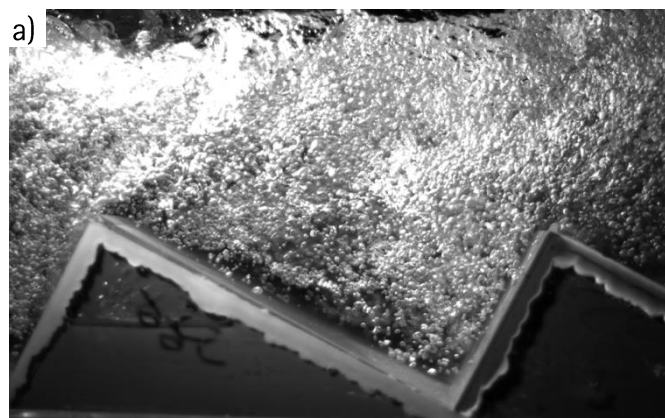
#### Air-water flows

In addition to the flow structure and energy dissipation for single-phase water flow, supercritical aerated flows were investigated. A sluice gate was placed over the edge of the first step, thus accumulating energy upstream and resulting in a high velocity jet downstream. The gate opening was in the range of 4 to 8 cm. Figure 3.3 shows some exemplary images of the aerated flow for setups 1V:2H\_AW, 1V:3H\_AW and 1V:6H\_AW (Air-Water flow). Measurements were conducted using a phase detection probe in the channel centreline and images were recorded with a high-speed camera through the side wall (penetration depth of roughly 2 cm, ultimately depending on the aeration level, with a focus depth of 1.5 cm).

#### Grass-steps interface

At prototypes, grassed surfaces are typically found side by side with stepped revetments. The accessibility of these types of structures makes grass as a suitable companion at areas of lower risk. For all three main setups considered (1V:2H, 1V:3H and 1V:6H), grassed surfaces of roughly 3 cm height were installed both over the step edges and at the cavity through level (see Figure 3.4 and Figure 3.5), resulting in a total of six studied configurations: 1V:2H\_GE, 1V:3H\_GE and 1V:6H\_GE (Grass Edge), and 1V:2H\_GN, 1V:3H\_GN and 1V:6H\_GN (Grass Niche).

The intention of these experiments was to analyse the turbulent stresses occurring at the grass-step interface, allowing determination of safer installation at prototype scale. The measurements were conducted with an ADV profiler through an entire cross-section, allowing insight on both, the stepped and grassed areas and the transition between them.



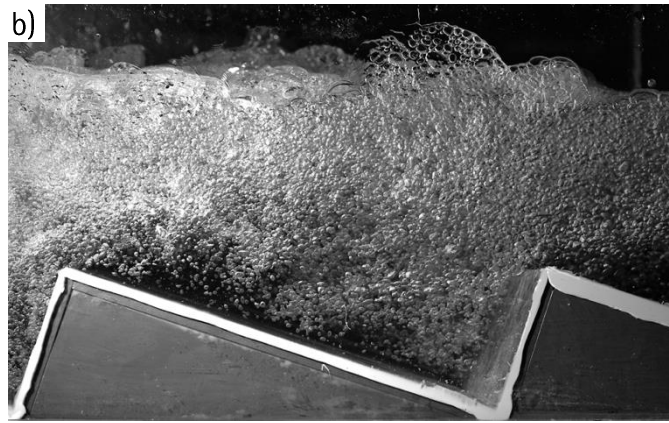


Figure 3.3. Air-water flow over the different studied models: a) 1V:2H\_AW, b) 1V:3H\_AW and c) 1V:6H\_AW. Images obtained with the high-speed camera (flow from left to right).





Figure 3.4. Flow over the different studied models with grass over the stepped edges: a) 1V:2H\_GE, b) 1V:3H\_GE and c) 1V:6H\_GE (flow from left to right).

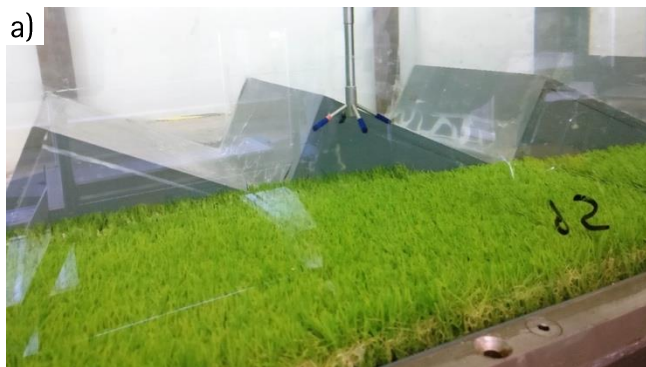


Figure 3.5. Flow over the different studied models with grass at the niches level: a) 1V:2H\_GN, b) 1V:3H and c) 1V:6H\_GN (flow from left to right).

### 3.1.3 Instrumentation and data analysis

#### Ultrasonic sensors (USS)

Flow depths were recorded using ultrasonic sensors (USS). Available ultrasonic sensors at FH Aachen are presented in Table 3.3. The sensors were mounted in fixed bars over the different setups and plugged to HBM QuantumX 840A amplifiers. Data was recorded as raw voltage using the Catman Easy software by HBM and later analysed using MATLAB®, obtaining mean and fluctuating flow depths through a linear calibration function measured in situ.

Table 3.3. Basic operational parameters of the available ultrasonic sensors (accuracy as provided by the manufacturer). A comparison with laboratory accuracy estimations can be found in Figure 3.6.

Model	Response time (ms)	Blind zone (cm)	Operating range (cm)	Accuracy (mm)	Detection cone (cm)
mic+25/IU/TC	32	3	25	0.025 – 0.100	5
mic+35/IU/TC	64	6.5	35	0.025 – 0.170	10
mic+130/IU/TC	92	20	130	0.180 – 0.570	15

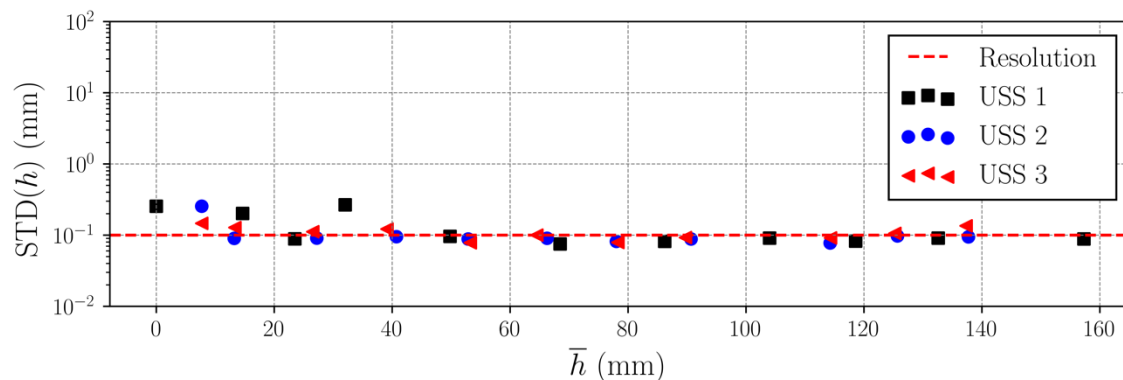


Figure 3.6. Accuracy levels for three different mic+25/IU/TC sensors over the sampling distance range corresponding to different mean flow depths ( $\bar{h}$ ); measured over several static levels and estimated as the standard deviation  $STD$  of the (expected) static measurement.

USS operate on a pulse-echo principle. Echoes are focused in a narrow zone and time delay is measured when the echo is successfully recovered by the USS. The zone where the echoes are successfully recovered for a flat surface normal to the detection axis is known as detection cone (Figure 3.7a). Some echoes can be lost when the angle between the normal of the free surface and the axis of the measuring cone ( $\beta$ ) is over  $13^\circ$  approximately (see Figure 3.7). When the echo is lost, an unrealistic voltage is provided by the sensor which results in a larger standard deviation ( $STD$ ) of the distance estimations.

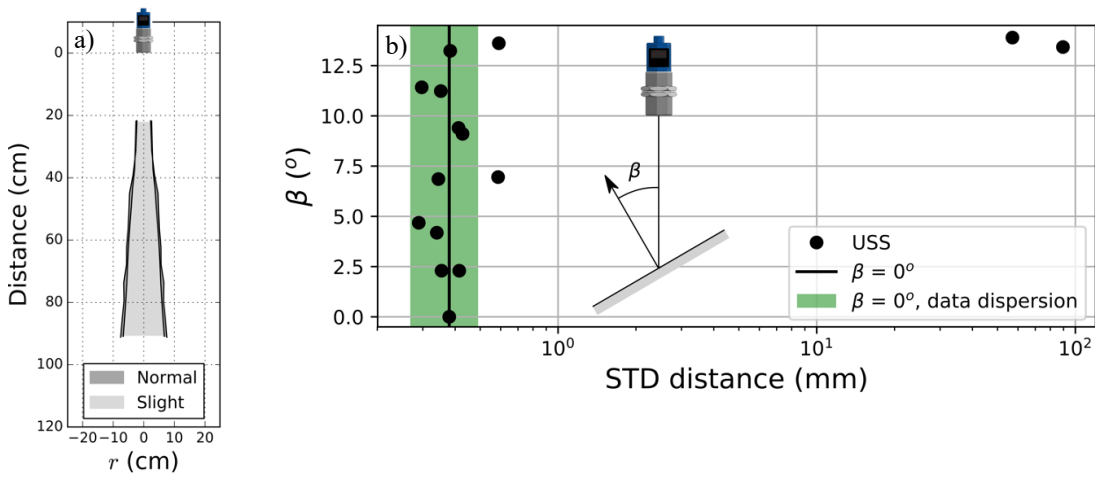


Figure 3.7. Detection properties of the USS. a) Detection cone as a function of the radial distance ( $r$ ) for a mic+130/IU/TC measured in the laboratory (two manufacturer options tested: normal and slight, with negligible differences) and b) limiting measurable steepness of the free surface.

The USS estimations are also sensitive to temperature differences. All recordings were conducted with the laboratory windows closed after one hour of sensors heating, based on temperature dependence observations (see Figure 3.8).

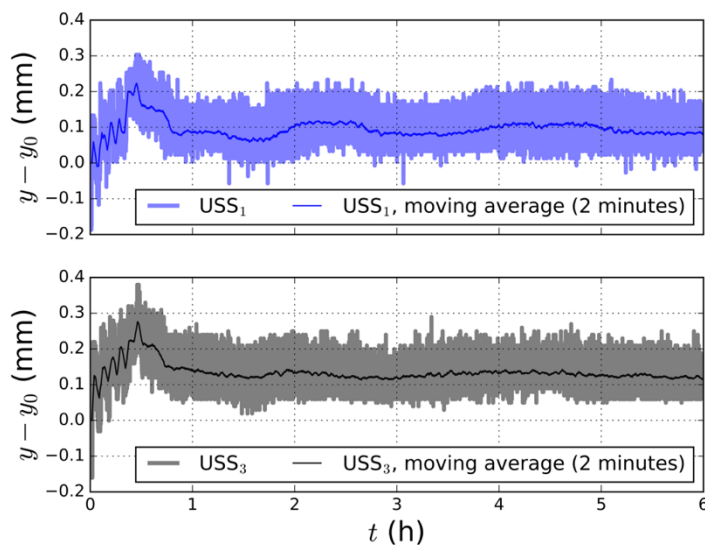


Figure 3.8. Temperature dependence of two different USS,  $y$  for the instantaneous recording (distance to a fixed location), which is shifted by the initial distance measurement  $y_0$ .

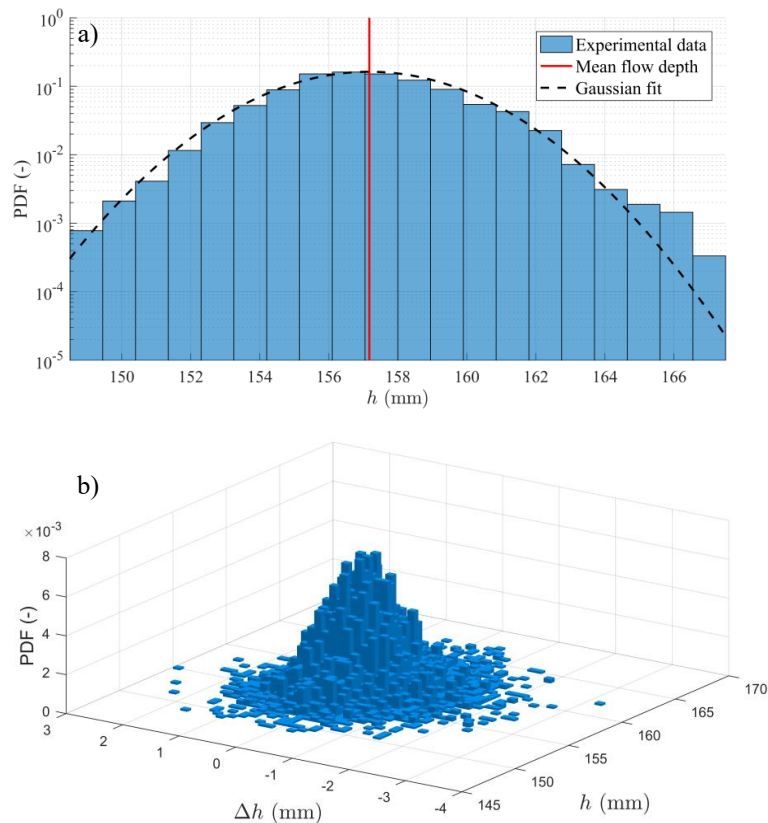


Figure 3.9. Probability Density Function (PDF) of the flow depth  $h$ , measured in the model 1V:2H over the step 5 at flow rate  $Q = 70$  l/s. Note that this is one of the highest discharges investigated with lower flow depth, resulting on higher turbulence quantities. a) Mean and Gaussian fit, and b) 2D PDF, including data of the depth differences ( $\Delta h$ ).

The measured flow depths usually showed good clustering, without noticeable outliers (see Figure 3.9a). Further insight on the outliers' structure can be gained through the observation of the variable differences (Goring and Nikora 2002), which for this application, also showed good clustering (see Figure 3.9b). Nonetheless, filtering was implemented to reduce the impact of random outliers sampled with the data. The filtering technique used for the flow depth data is the Robust Outlier Cutoff (ROC) presented in Appendix A.1. It must be noted that filtered data percentages are usually small; for instance, the data presented in Figure 3.9 hold a 0.011 % rejection rate.

#### ADV Vectrino Profiler (ADV)

Acoustic Doppler Velocimetry (ADV) has been extensively used in the past for point velocity determination in very diverse applications related to hydraulics, oceanography, and sediment transport. In this study, instantaneous velocities were measured with an ADV profiler (Vectrino II, Nortek) with the 4-beam down-looking probe (Figure 3.10) connected by a 1 m flexible cable and firmware version: 2779/1.32.

The ADV profiler was mounted over an *ise*/standardized profile, which is positioned using a Computerized Numerical Control (CNC) system with an accuracy of 0.1 mm. The measuring range of the ADV profiler comprehends 3 to 7 cm. Several researchers have observed that, when using a Vectrino profiler, sweet-spot (SS) data are the most reliable (Thomas et al. 2017; Koca et al. 2017; Brand et al. 2016; MacVicar et al. 2014). The SS is located within the sampling volume where the overlap of the four acoustic beams is largest (Thomas et al. 2017; Koca et al. 2017). Thomas et al. (2017) observed that noise varies parabolically with a minimum close to the SS. Brand et al. (2016) and Koca et al. (2017) observed that a  $-5/3$  power spectra slope is only obtained using SS data. The SS corresponds approximately to the 12th bin in a Vectrino profiler.



Figure 3.10. Four-beam down-looking probe of the ADV Vectrino Profiler interacting with the free surface. Note the wake occurring downstream of the probe, resulting in a trough that can eventually trap air (flow from left to right).

Data was sampled using the Nortek Vectrino Profiler software and directly converted into MATLAB® format for post processing. A time sensitivity analysis for flow velocity measurements can be found in Appendix A.2. ADV data may contain outliers, which can be due to different reasons (Thomas et al. 2017). Temporal filtering has been proposed in the past, with the works of Goring and Nikora (2002) and Wahl (2003) being widely embraced by the community.

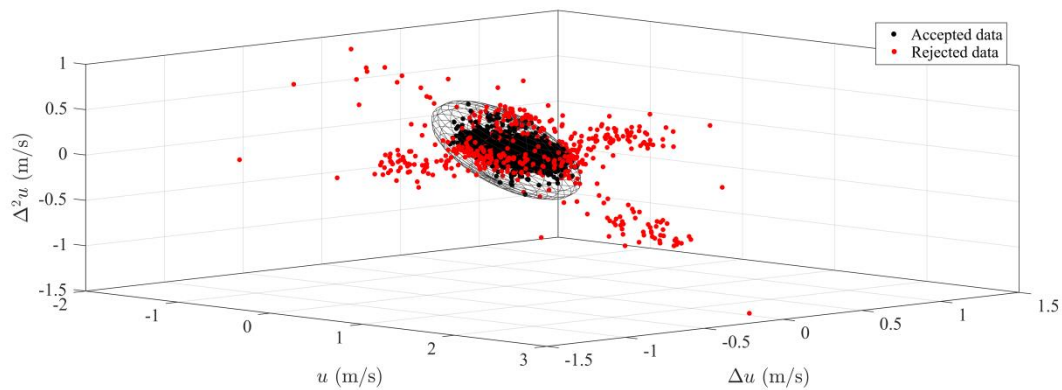


Figure 3.11. Ellipsoid (mesh) resulting from application of Goring and Nikora (2002), as modified by Wahl (2003), to data gathered at  $q = 0.086 \text{ m}^2/\text{s}$ , over step 6 at 7 cm depth for model 1V2H.

The Goring and Nikora (2002) despiking method, as modified by Wahl (2003), was implemented in MATLAB® and applied to all velocity measurements without any replacement strategy (i.e. outliers were discarded). Goring and Nikora (2002) proposed a filtering technique based on the observation that "good data" tend to cluster inside an ellipsoid, defined in the coordinate system built using the temporal velocity data and its finite differences up to the second order ( $u$ ,  $\Delta u$ , and  $\Delta^2 u$ , respectively). Wahl (2003) proposed some modifications to Goring and Nikora (2002), such as using robust estimators for velocity-expected value and variance and rejection of all velocity components when an outlier is detected at least in one of the velocity components. Exemplary Goring and Nikora (2002) and Wahl (2003) filtering is shown in Figure 3.11. Additionally, data presenting SNR below 5 dB and correlation below 60% were rejected, similar to Leng and Chanson (2015). The expected value of the velocity was taken as the median of the temporal velocity signal.

After obtaining all temporally filtered velocities, a moving median has been computed for each  $i$  measurement with a spatial window of 37.5 % of the bins range (i.e., ~11 mm). Additional spatial filtering

was developed for these experiments and can be found in Valero and Bung (2018b). A comprehensive flow chart of the filtering process is presented in Figure 3.12. The data was spatially filtered only in the region  $z > 0.10 \bar{h}$ .

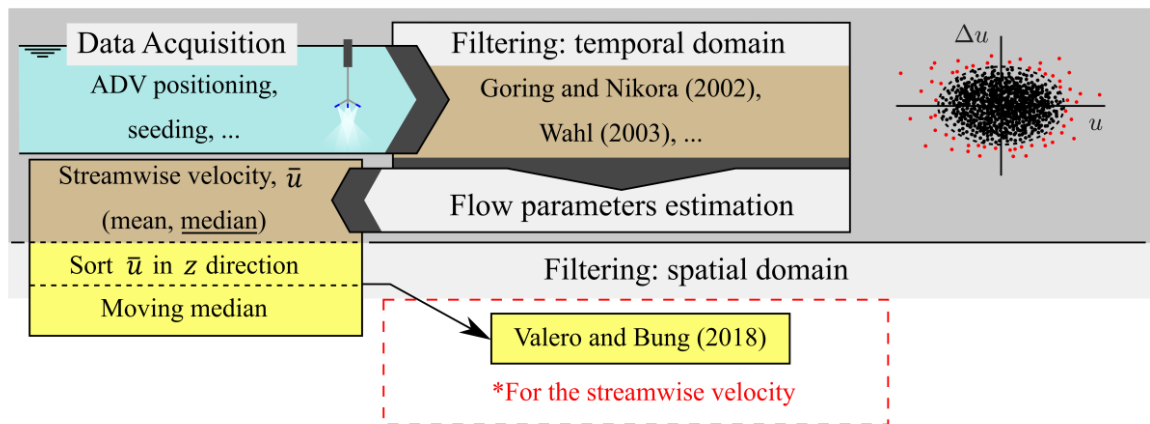


Figure 3.12. Filtering flow chart for the velocity data recorded with the ADV profiler.

### Conductivity probe (CP)

In air-water flows, even the measurements of the most basic flow properties are difficult. Detection of the strongly disturbed free surface in highly aerated open channel flows is as challenging as the determination of flow velocities for which the presence of air bubbles prevents the use of classical mono-phase flow instrumentation such as Pitot tubes, Acoustic Doppler Velocimetry (ADV), laser-supported Particle Image Velocimetry (PIV), Laser Doppler Velocimetry (LDV), etc. If the void fraction is larger than about 3 % (Chanson 2013), intrusive phase-detection (conductivity or optical fibre) probes for determination of local void properties are the most recognized instrumentation (Jones and Delhaye 1976; Cartellier and Achard 1991; Chang et al 2003) being commonly employed in many studies on air-water flows from chemical, nuclear and civil engineering disciplines. These sensors are positioned in the air-water flow, facing the main flow direction intrusively.

The two tips of a phase-detection needle probe (Figure 3.13), denoted as leading and trailing tips, allow simultaneous phase detection at two fixed locations, separated by a streamwise distance. The probe yields two signals at a sampling rate  $f_s$  that, ideally, would be identical, but shifted by  $\Delta t$ . A simple method to obtain "water" and "air" phase signals from the raw voltage output is the single-threshold technique (Cartellier and Achard 1991), which results in binary time series ( $S_1$  and  $S_2$ ), taking the value 0 (water) and 1 (air).

Both phase detection signals can be cross-correlated, thus obtaining a function of their similarity which is depending on the lag time. The most probably lag time  $\Delta t$  can be obtained by identifying the lag time where the cross-correlation function peaks. Thus, a mean velocity can be estimated as:

$$\bar{u} \approx \frac{\Delta x}{\Delta t} \quad (3.1)$$

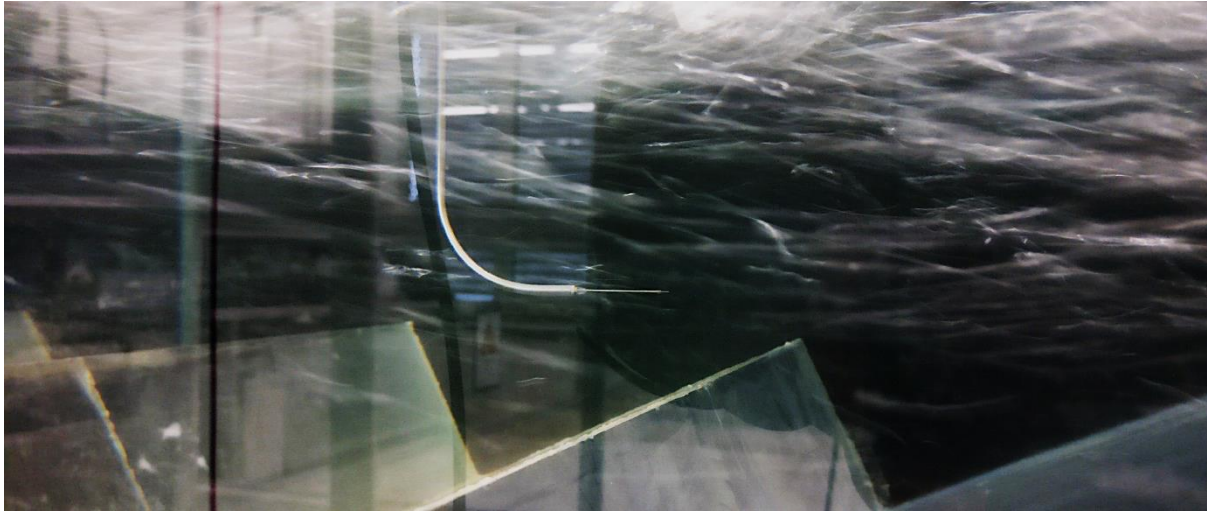


Figure 3.13. Phase detection conductivity probe mounted over the stepped model 1V:2H for a low aeration flow (notice the white "stripes" of the image, which are the moving bubbles).

### High-Speed Camera (HSC)

High-speed videos have been captured with a Phantom M120 camera supplied by LaVision. The camera's maximum resolution is  $1920 \times 1200$  px while the maximum frame rate ( $f_s$ ) is 730 Hz. In order to enhance the contrast, the backside of the flume was equipped with a black PVC wall. Flow illumination was achieved by using a pulsed LED lamp. Exemplary images were presented in Figure 3.3. Data acquisition was carried out using Davis software.

Traditionally, HS cameras have been used to record moving particles coupled with a laser sheet, to later extract information on the displacements through the Particle Image Velocimetry (PIV) method (Adrian and Westerweel 2011). In air-water flows, bubbles can be used as tracers when a slip-free bubble transport is assumed and the flow velocity is much higher than the bubble rise velocity. This PIV modification is oftentimes called Bubble Image Velocimetry (BIV). However, PIV-based methods are limited to a minimum spatial resolution. In this study, to overcome this issue, the Optical Flow (OF) method is applied in this study to determine velocity fields in aerated flows. OF yields dense velocity fields giving data at each pixel. It was recently shown that OF can provide data with similar accuracy as BIV in aerated flows (Bung and Valero 2016a,b). The open-source toolbox FlowCV (Bung and Valero 2017) is applied.

## 3.2 Flow depths

### 3.2.1 Introduction

Flow depths have been measured across different setups, with the focus to study spatial depth derivatives. The large amount of measured depths also allowed insight on the turbulent properties of the flow. Depths have been measured at a total of 800 locations for 180 seconds (7.2 M instantaneous depths measured) which yield a nearly negligible uncertainty due to time sampling. The range of resulting Froude and Reynolds numbers is shown in Figure 3.14, and the range relative flow depths and submergences in Figure 3.15, with  $\bar{h}$  the mean flow depth,  $h_c$  the critical flow depth and  $k_v$  the cavity height.

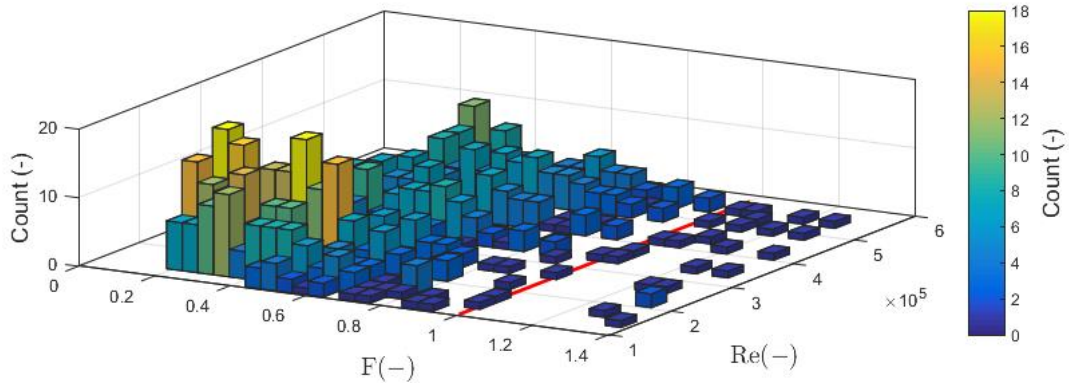


Figure 3.14. Distribution of Froude ( $F$ ) and Reynolds ( $Re$ ) numbers of the measured flow depths (red line dividing sub- and supercritical flows).

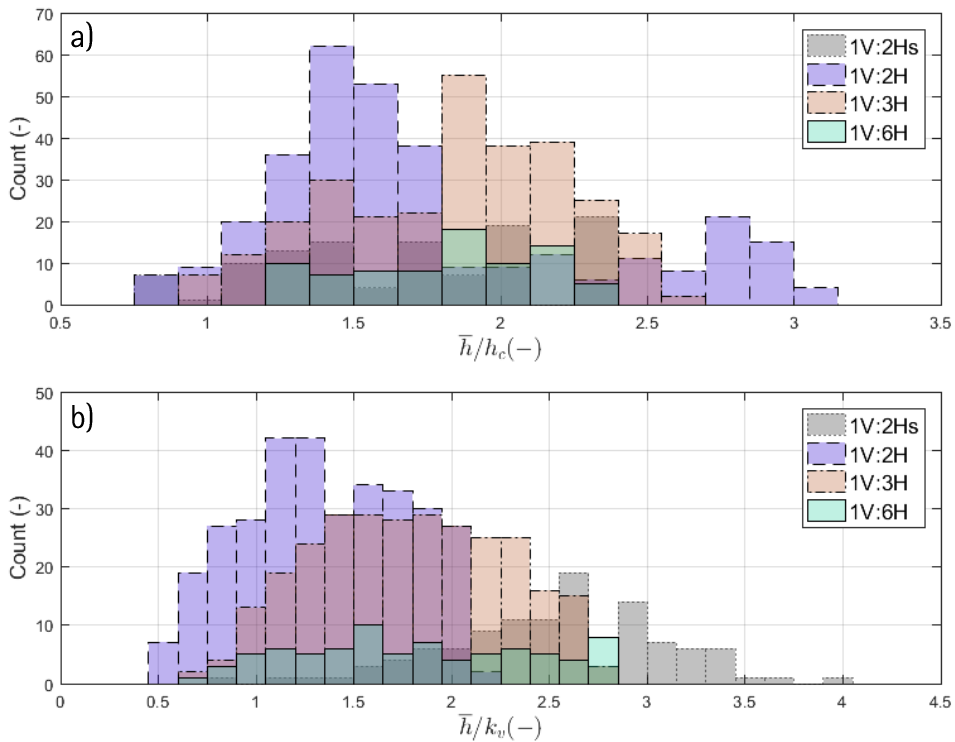


Figure 3.15. Distribution of a) flow depths and b) flow submergences of the measured flow depths.

### 3.2.2 Mean flow depths

The type of backwater curve corresponds to H2 (Montes 1998), as sketched in Figure 3.16, holding the following characteristics:

$$\bar{h}(x = x_c) = h_c \quad (3.2)$$

being  $x_c$  the coordinate at which the critical depth  $h_c$  takes place. For large distances  $x_c$ , the slope flattens:

$$\frac{d\bar{h}}{dx} \rightarrow \varepsilon \quad \text{for } x \rightarrow -\infty \quad (3.3)$$

$\varepsilon$  being a small quantity, that would null when the normal depth would establish (note that in a horizontal channel as in current experiments, uniform flow does not set in). See Figure 3.16 for an exemplary (ungated) flow where the critical depth occurs due to free outflow.

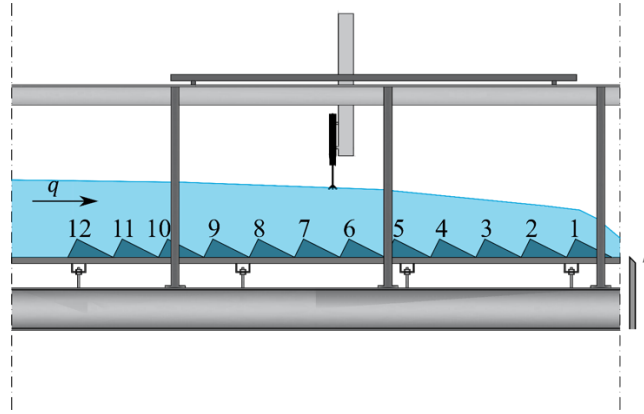


Figure 3.16. H2 drawdown curve as a result of the free discharge over the last step (exemplary setup 2H:1V). Note the downstream gate, which can be operated as to affect the flow depth over the last step.

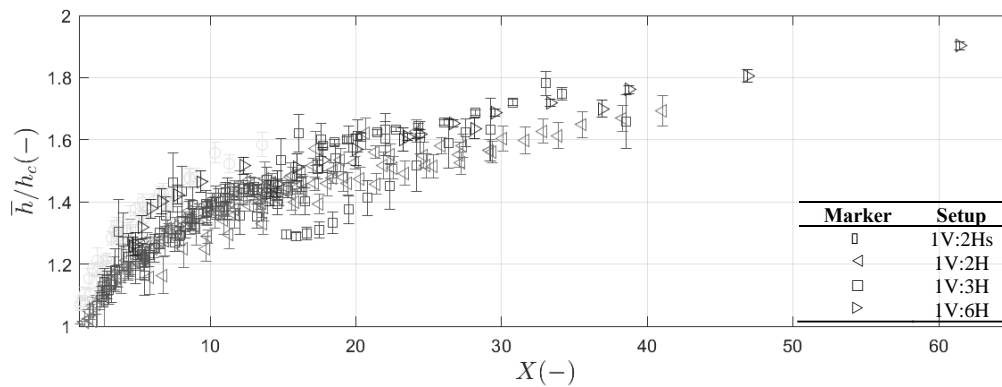


Figure 3.17. H2 drawdown curve, only data with critical depth at the outlet (darker colour for bigger steps, flow from right to left).

A slightly wavy drawdown curve is observed, as it is also known for broad crested weirs. In order to not disturb the gradients and smooth the curves, the data should satisfy the following condition:

$$\frac{d}{dx} \left( \frac{d\bar{h}}{dx} \right) < 0 \quad (3.4)$$

A simple function that fulfils the previous conditions is:

$$Y = a X^b \quad (3.5)$$

with  $Y = \bar{h}(x)/h_c$ ,  $\bar{h}(x)$  the mean flow depth at a distance  $x$  from the critical section at the outlet and  $X = (x_c - x)/h_c$ .

Using the data where a critical depth occurs naturally at the outlet (see e.g. Figure 3.8 for 1V:2H),  $a$  and  $b$  can be easily estimated using a robust fit method (LAR, MATLAB®). Data for  $X > 1$  has been also ignored, as this is the position where the sensor holds larger uncertainty in its estimation due to the free surface curvature. Results for coefficients fitting are presented in Table 3.4.

Table 3.4. Mean flow depth best fit, 95 % intervals for  $a$  [ $a_{min}$   $a_{max}$ ] and for  $b$  [ $b_{min}$   $b_{max}$ ], and goodness of fit  $r^2$  (R-square) and RMSE (root mean squared error).

Setup	$a$	$b$	$a_{min}$	$a_{max}$	$b_{min}$	$b_{max}$	$r^2$	RMSE
1V:2Hs	1.0430	0.1600	1.036	1.0510	0.1556	0.1644	0.9937	0.01069
1V:2H	0.9526	0.1530	0.9374	0.9679	0.1467	0.1592	0.9512	0.03655
1V:3H	0.9335	0.1714	0.8868	0.9802	0.1528	0.1900	0.7859	0.07754
1V:6H	0.9854	0.1574	0.9401	1.0310	0.1424	0.1725	0.9486	0.03913

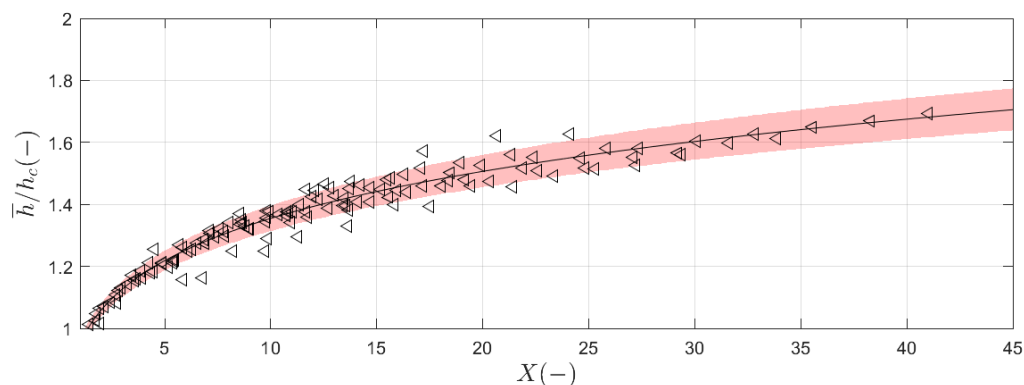


Figure 3.18. H2 drawdown curve, only data with critical depth at the outlet and 1V:2H. Best fit and uncertainty bounds (95 %) in red (flow from right to left).

### 3.2.3 Mean flow depth gradients

Flow depth gradients have a more direct connection to the energy dissipation. It is interesting to show how flow depth varies on the streamwise coordinate. In the previous section, only the drawdown curves starting at a critical depth inside the flume were shown (free outflow). However, numerous tests were run with a downstream gate modifying the tail-water level, which would mean that the critical depth would virtually take place out of the flume (large  $x_c$ ).

Equation 3.4 can be derived as:

$$\frac{d}{dx} \left( \frac{\bar{h}}{h_c} \right) \equiv \frac{1}{h_c} \frac{d\bar{h}}{dx} = \frac{a b}{h_c} \left( \frac{x_c - x}{h_c} \right)^{b-1} \quad (3.6)$$

$h_c$  nulls at both sides of the equality, and  $x$  coordinate can be removed by using Eq. (3.5), thus resulting in:

$$\frac{d\bar{h}}{dx} = a b \left( \left[ \frac{\bar{h}}{a h_c} \right]^{1/b} \right)^{(b-1)} = \frac{b}{a^{1/b}} \left( \frac{\bar{h}}{h_c} \right)^{(b-1)/b} \quad (3.7)$$

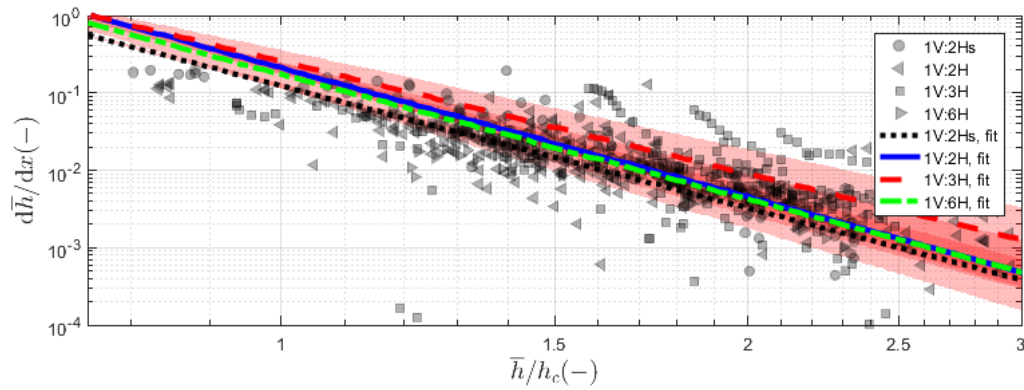


Figure 3.19. Flow depth gradients. In red shadow, the uncertainty estimation related to 95 % confidence bounds of each setup.

As shown in Figure 3.19, it seems as there is no significant difference between the considered slopes. Also, results with smaller steps fall within the uncertainty of the bigger scale model.

### 3.2.4 Flow depth fluctuations

Turbulence reaches the free surface, distorting it, resulting in some characteristic turbulence fluctuations. The link between velocity and free surface turbulence fluctuations is not straightforward, but larger turbulent energy in the flow will result in larger fluctuations at the free surface, eventually leading to self-aeration (Valero and Bung 2018a).

As shown in Figure 3.20, most of the free surface fluctuations fall below 2 % and there is a clear trend with the flow depth: smaller flow depths are more prone to oscillate around the mean value. This can also be related to the fact that all investigated flow depths correspond to a H2 draw down curve, which presents higher flow depths at the beginning of the steps, where flow is still not fed with the cavity turbulence.

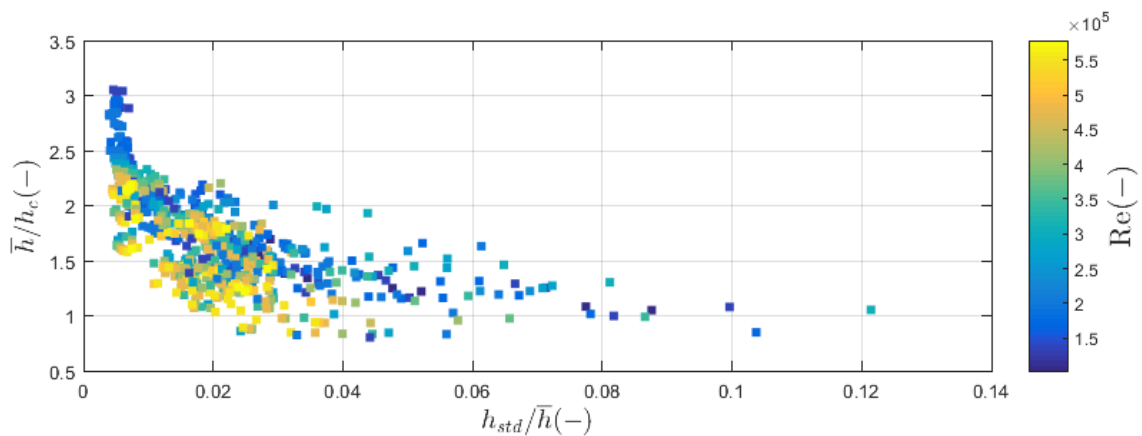


Figure 3.20. Flow depth fluctuations over different  $X$  locations and flow rates.

### 3.2.5 Conclusions

Flow depths have been obtained for a wide range of flow conditions, considering all setups 1V:2Hs, 1V:2H, 1V:3H and 1V:6H. The mean flow depths (and its gradients) show a consistent trend for a H2 drawdown curve. The flow gradients are slightly smaller for 1V:2Hs than for 1V:2H, which may highlight potential scale effects. All the other three setups show nearly identical flow depths gradients (within the 95 % uncertainty bounds). The case 1V:3H showed slightly larger gradients with considerably bigger uncertainty.

### 3.3 Flow velocities

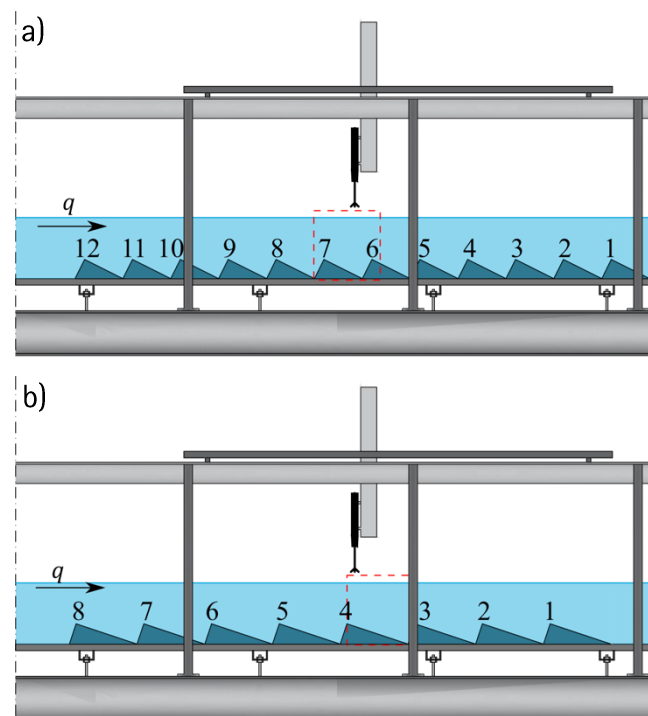
#### 3.3.1 Velocity determination techniques

Flow velocities were obtained using three techniques. For clear-water flows, an Acoustic Doppler Velocimeter (ADV) was employed allowing for intrusive determination of three-dimensional velocities. The probe was set up in the central step of each setup, and was moved in the streamwise and normalwise directions (central plane) to obtain velocities across the entire step cavity. Additionally, transversal measurements were carried out over the grassed setups (perpendicular to the central plane). Seeding was added when the signal-to-noise ratio and correlation values dropped. The available ADV probe (i.e. ADV profiler) provides velocity profiles in short distance to the probe head. A sampling time of 300 s was chosen after a deep sensitivity analysis as shown in Appendix A.2. As recommended by Koca et al. (2017), data analysis included data from the Sweet-Spot (SS)  $\pm 8$  bins only in order to limit potential uncertainty below 10 %. All data was temporally filtered using the established Goring and Nikora (2002) technique, as modified by Wahl (2003) and spatially filtered using the method of Valero and Bung (2018b). Data for which the SNR or mean correlation dropped below 5 dB or 60 %, respectively, were eliminated from the instantaneous series.

For air-water flows, the Optical Flow (OF) method using high-speed images is employed. This air-water flow data is compared to velocity data from the intrusive conductivity probe (CP). It is known from the literature that optical velocity measurements (BIV and OF) tend to underestimate data from intrusive measurements (CP), which is most likely a consequence of wall effects. However, it will be shown that velocity fields are qualitatively unaffected and resulting velocity gradients, and thus friction factors, may be extracted with sufficient accuracy.

#### 3.3.2 Measuring locations

For each setup, a single step was considered for detailed velocity measurements. These steps were located at roughly half distance from the inlet to the macro-roughness section in the flume in order to have a flow situation being undisturbed from inlet and outlet conditions. Studied steps are highlighted in Figure 3.21.



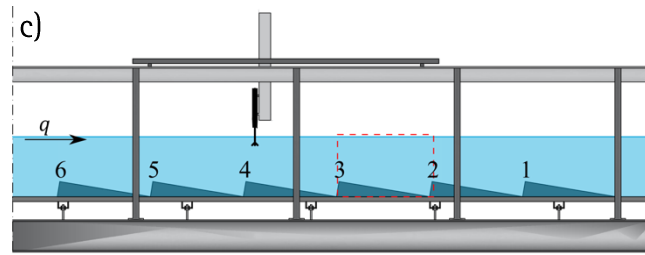


Figure 3.21. Cavities for detailed velocity measurements at each of the setups, a) 1V:2H, b) 1V:3H, c) 1V:6H (flow from left to right).

ADV data were gathered with high spatial resolution. Table 3.5. Main flow parameters and measuring point spacing ( $\Delta x$ ,  $\Delta z$ ). Table 3.5 presents the measuring point spacing at investigated step cavities for all setups.

Table 3.5. Main flow parameters and measuring point spacing ( $\Delta x$ ,  $\Delta z$ ).

Model	Flow rate (m <sup>3</sup> /s)	$h$ (m)	$U$ (m/s)	$F$ (-)	$D_h$ (m)	$k_v/D_h$ (-)	$\Delta x$ (m)	$\Delta z$ (m)
1V:2H	0.020	0.150	0.230	0.19	0.395	0.1131	0.020	0.020
	0.030	0.150	0.345	0.28	0.395	0.1131	0.020	0.020
	0.050	0.130	0.663	0.59	0.359	0.1246	0.020	0.020
	0.070	0.160	0.754	0.60	0.412	0.1084	0.020	0.020
1V:3H	0.030	0.160	0.323	0.26	0.412	0.2300	0.025	0.020
	0.050	0.160	0.539	0.43	0.412	0.2300	0.025	0.020
	0.070	0.160	0.754	0.60	0.412	0.2300	0.025	0.020
1V:6H	0.030	0.154	0.336	0.27	0.402	0.2452	0.040	0.020
	0.070	0.165	0.731	0.58	0.421	0.2345	0.040	0.020

### 3.3.3 Mean velocity fields

In order to evaluate the bottom friction, flow velocities within the boundary layer near the pseudo-bottom, formed by the step edges, are of particular interest. Subsequently, the flow case 1V:3H (slope) and  $Q = 50$  l/s is illustrated, representing a medium slope and discharge from the range of all setups. Figure 3.22 and Figure 3.23 are presented in a dimensionless form.

For subcritical flows (sampled using ADV), a downstream gate was used to control drawdown conditions. It must be noted that supercritical flow conditions were necessary to generate aerated flows in the given setup (obtained by an upstream gate with 4 cm gate opening), yielding higher absolute flow velocities and thus, lower flow depths when compared to the non-aerated tests for identical discharges. The free surface level is included in Figure 3.22 for the ADV measurements while  $h_{90}$ , i.e. the air-water level with 90 % air concentration is shown for the OF data (Figure 3.23). The latter is obtained from the conductivity probe (exemplary air concentration data is presented in Appendix A.3).

The figures demonstrate that velocity fields are similar for both flow situations, i.e. the non-aerated and aerated case. This finding suggests that the velocity gradient and thus, the bottom friction are similar despite the aeration. In this case, resulting friction factors from the comprehensive ADV data set (gathered in non-aerated flows) may be considered to be applicable for the aerated case as well. Dimensionless velocity profiles and resulting gradients are analysed in more detail in the next section.

The presented velocity fields in Figure 3.22 and Figure 3.23 are typical for the conducted range of experiments. However, it was found that for a given discharge, the flow tends to penetrate more into the cavity if the cavity length increases. In turn, the same effect is found for decreasing discharges and constant cavity size. This phenomenon is known from stepped spillway research as the transition from so-called skimming flow (in which the flow in the outer flow region is mostly parallel to the pseudo-bottom

(Chanson 2002) for decreasing  $h_c/s$  (ratio of the critical depth over the step height). In this case the flow reattaches quickly downstream of the upstream step edge and impacts the downstream step face, instead of producing an active, large recirculation region which would dissipate energy across a larger scale. Case 1V:6H represents an extreme case of this situation. In such geometry, only a small part of the cavity is working as a recirculation region whereas the flow reattaches parallel to the "smooth" face of the step, which justifies lower friction factors. A detailed analysis of resulting flow resistances is presented in Section 3.4.

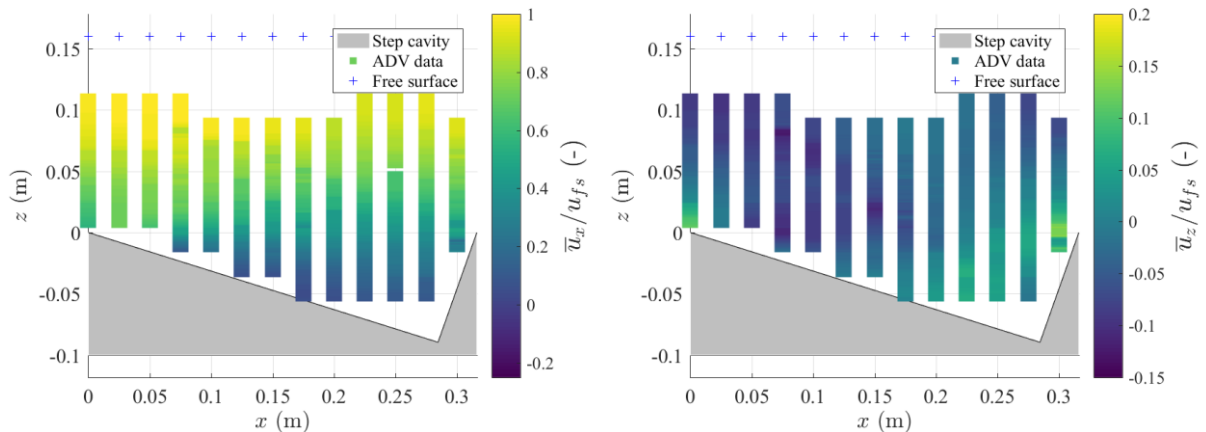


Figure 3.22. Mean velocity fields for 1V:3H and  $Q = 50$  l/s (velocity data is related to the free-stream velocity  $u_{fs}$ ), a) streamwise, b) normalwise, flow from left to right.

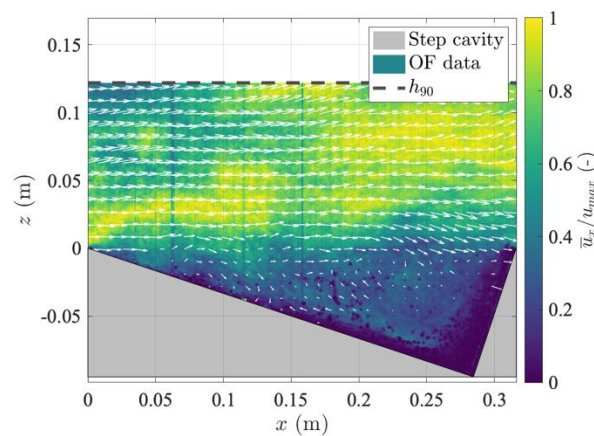


Figure 3.23. Velocity magnitude field for 1V:3H and  $Q = 50$  l/s, including velocity vectors indicating streamwise and normalwise components (only every 40<sup>th</sup> velocity vector is illustrated for better legibility). Velocity data is related to the maximum velocity  $u_{max}$  in the free-stream region (flow from left to right).

### 3.3.4 Velocity gradients

In Figure 3.24, velocity profiles are extracted from the boundary layer with thickness  $\delta$  for different flow cases (including different slopes and discharges) and all employed measuring techniques. The results support the hypothesis from the previous section, i.e. a self-similarity for the velocity gradients and thus, bottom friction is found. It is acknowledged that the velocity profiles from the OF method differ for the region near the boundary ( $z/\delta < 0.1$ ). However, this data is affected by averaging (smoothing) velocity data from a pixel ensemble, thus including null velocity data from the non-moving step cavity in the images.

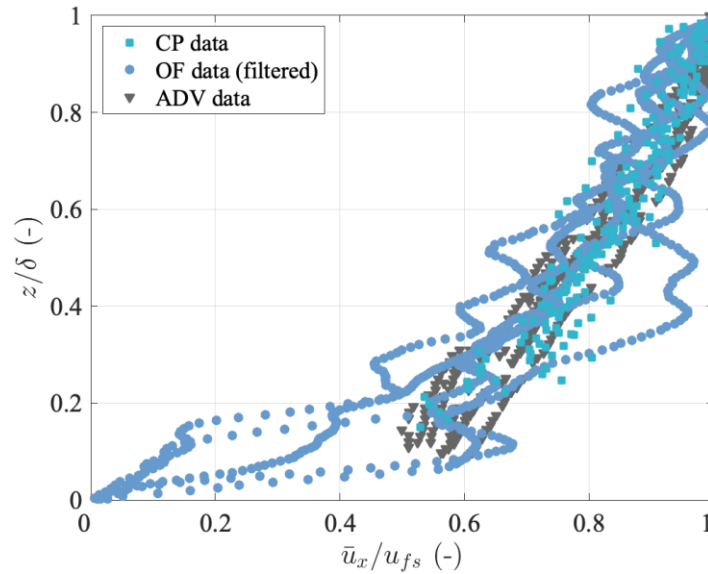


Figure 3.24. Dimensionless velocity profiles obtained with three different measuring techniques for different aerated (ADV) and non-aerated flow cases (OF and CP).

### 3.3.5 Turbulence and shear stresses

Streamwise fluctuations reach around 35 % of the free stream velocity. Normalwise and spanwise are in the same order, reaching up to 20 %, which is in the same order of magnitude of common boundary layers over rough beds. Essentially, the flow kinetic energy is accumulated in the streamwise component. The flow interaction with the step cavity leads to large turbulent exchanges in the normalwise direction, also transferred into the transverse direction. The flow is greatly anisotropic with a negative transfer of momentum from the mean flow to the step cavity, especially for large aspect ratios and large velocities.

A completely different shearing was observed for 1V:2H and 1V:3H when compared to the 1V:6H case, where there is a peak of shearing (around 0.2) over the edge and decreases afterwards. The 1V:2H and 1V:3H cavities present a more uniform distribution of shearing, produced by the vortex formation inside the cavity. For the small aspect ratio, the flow reattaches and flows parallel to the smooth faces of the steps (see Figure 3.25), hence resulting in a reduced energy dissipation.

$\overline{u_x' u_y'}$  are considerably lower. Note that, differently from  $u_y$ , velocity fluctuations do not necessarily null due to symmetry.  $u_y'$  may fluctuate positively or negatively independently of the sign of  $u_x'$  fluctuation. Same for  $\overline{u_y' u_z'}$ , which remains at  $10^{-3}$  times the free stream velocity (for practical purposes, null).

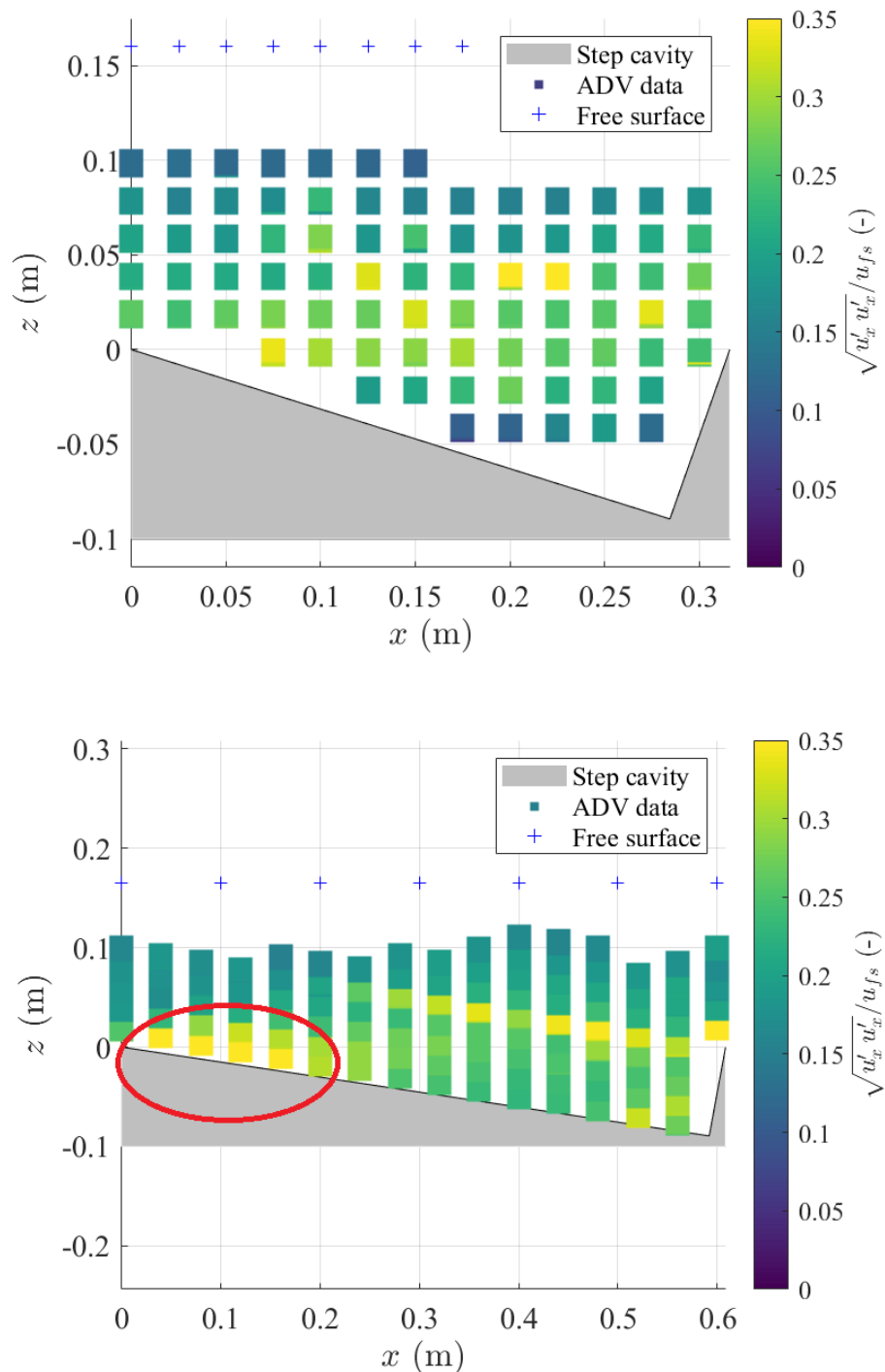


Figure 3.25. Turbulence structure in a 1H:3V step cavity (top) and 1H:6V step cavity (bottom) with the reduced recirculation region marked in red. Both cases with  $Q = 70$  l/s.

### 3.3.6 Conclusions

Different measuring techniques were employed. i.e. three-dimensional ADV measurements in clear-water flows with high temporal and spatial resolution, time-resolved 2D high-speed camera investigations in aerated flows as well as time-averaged 1D measurements with a conductivity probe in aerated flows. It was shown that time-averaged dimensionless velocity fields and profiles are similar between the different geometries as well as for the different cases, i.e. non-aerated and aerated flows.

Turbulence characteristics were analysed using the ADV data only. From this analysis, it may be concluded that turbulence quantities occurring over steps are generally in the order of magnitude of those in boundary layer flows over macro-roughness. Nonetheless, the flow structure changes for the larger cavity

studied (1V:6H) where the flow reattaches over the horizontal face and recirculation is considerably harmed, thus impacting energy dissipation properties.

The role of the cavity is to create a big roller structure, which causes large streamline curvature and leads to enhanced energy dissipation. Consistently, the step geometry defines (or influences) this vortex formation and it seems safer to design with small aspect ratios.

Additionally, all the turbulence stresses were experimentally disclosed in this research, which assisted on better understanding the role of the cavity. It does not only create an increased energy dissipation and turbulence quantities but also increases flow anisotropy, which produces intense transverse turbulence momentum fluxes. The shearing mechanism changes with increasing aspect ratio, which, as above-mentioned, influences the change in the energy dissipation properties.

### 3.4 Energy dissipation

#### 3.4.1 Introduction

The purpose of the present study is to evaluate the energy dissipation during wave run-up at a stepped revetment. In this case, energy dissipation will compose of 1) the wave tip impacting the step faces (in turn causing local losses until the niche is filled with water) and 2) the bottom friction which is predominant when the steps are filled with water. The presented data considers the second phase of the process and thus, ignores potential wave impact effects. However, the presented data helps to better understand the turbulent, physical processes leading to energy dissipation.

#### 3.4.2 Friction factors from flow depth data

The water surface equation in gradually varied, steady open channel flows, over horizontal bed can be written as:

$$\frac{\partial \bar{h}}{\partial x} = -\frac{1}{8}f \frac{F^2}{1-F^2} \quad (3.8)$$

with  $f$  the friction factor and  $F$  the Froude number. Note that due to the critical section being present at the flume outlet, flow depth measurements in non-aerated flows have been mainly performed in subcritical flow conditions (see Figure 3.14).

By assuming that flow depths (reasonably) follow a power law expression, Eq. (3.7) can be used to estimate the water surface gradient:

$$\frac{\partial \bar{h}}{\partial x} = -ab \left( \frac{x_c - x}{h_c} \right)^{b-1} \quad (3.9)$$

Given that flow depths are measured all over the steps, gradients could be obtained through finite differences. In consequence, the friction factor can be easily computed if the water surface gradient is known:

$$f = -8 \frac{(1-F^2)}{F^2} \frac{\partial \bar{h}}{\partial x} \quad (3.10)$$

and thus:

$$f = 8 \frac{(1-F^2)}{F^2} ab \left( \frac{x_c - x}{h_c} \right)^{b-1} \quad (3.11)$$

By using a power law expression, small uncertainties and wavy profiles at inlet region are not transferred directly to the friction factor estimation. Note that this errors could lead, sometimes, to the occurrence of

negative friction factors (as far as a downstream flow depth, due to wave formation, is bigger than the subsequent one). Conversely, a systematic error is introduced by assuming the shape of the complete drawdown curve. Thus, only the median value of the friction factor is reported for each water table measured. Resulting friction factors are presented in section 3.4.4.

However, in the derivation of the presented friction factor equation Eq. (3.11) assumes a wide channel with the hydraulic diameter  $D_H = 4\bar{h}$  and thus neglects contribution to the total friction caused by the flume sidewalls. To obtain the friction factor of the stepped revetment ( $f_b$ ), it is necessary to correct the previously presented friction factors ( $f$ ). Hence, to obtain  $f_b$ , (bed), friction factors ( $f$ ) are applied the Einstein–Johnson correction, following the exact approach of Guo (2016). All values are presented in Figure 3.27, a representative value for each setup is presented in Table 3.6.

Table 3.6. Median friction factors by setup.  $k_v$  for the cavity depth,  $D_h$  for the hydraulic diameter.

Setup	1V:2Hs	1V:2H	1V:3H	1V:6H
$f_b$	3.37	4.78	2.58	3.25
$k_v/h$	0.390	0.748	0.565	0.569
$k_v/D_h$	0.136	0.264	0.223	0.227

### 3.4.3 Friction factors from velocity gradients

The differential form of the mean velocity equation over a rough surface can be written as (Monin and Yaglom 2007; Nikora et al. 2002):

$$\frac{d\bar{u}_x(z)}{dz} = \frac{u^*}{\kappa(z + d_r)} \quad (3.12)$$

with  $\bar{u}_x$  the mean (time –averaged) streamwise velocity,  $\kappa$  ( $= 0.40$ ) is the von Kármán coefficient,  $z$  the vertical coordinate over the step edges (see Figure 3.26),  $d_r$  the displacement length (virtual distance at which eddies feel the bed roughness), and  $u^*$  the shear velocity.

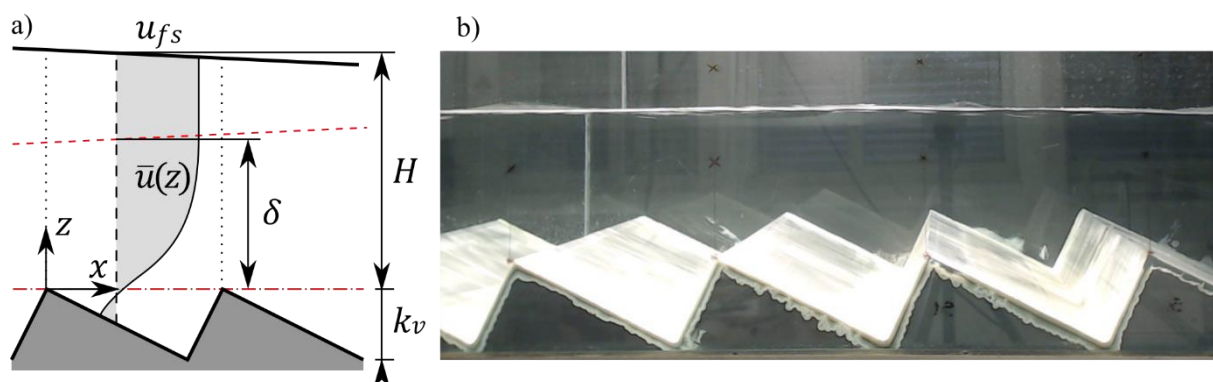


Figure 3.26. Flow structure and main variables. a) sketch and b) laboratory flow over the 1V:2H setup.

The shear velocity is a shear stress in velocity dimensions:

$$u^* \equiv \sqrt{\tau_b/\rho} \quad (3.13)$$

Likewise, the friction factor can be computed as (Pope 2000):

$$f = 8 \left( \frac{u^*_b}{U} \right)^2 \quad (3.14)$$

In Table 3.7,  $u^*_b$  was extracted from the velocity gradient, as well as  $d_r$ . The free stream velocity  $u_{fs}$  was extracted by extrapolating the mean velocity gradient while satisfying mass conservation (using the flow rate value, integrating velocity up to the flow depth level).  $\delta$  is obtained from the same computation.

*Table 3.7. Friction velocity and factors estimated using ADV, SS +/- 4 bins data. Cavity averaged (in the  $x - z$  plane) parameters, except  $\delta$  which corresponds to the flow over the frontal edge of the cavity.*

Model	$Q$ (m <sup>3</sup> /s)	$h$ (m)	$\delta$ (m)	$U$ (m/s)	$u_{fs}$ (m/s)	$u^*_b$ (m/s)	$d_r$ (m)	$k_v/D_h$ (-)	$f_b$ (-)
1V:2H	0.020	0.15	0.15	0.230	0.3455	0.1014	0.091	0.1131	1.555
	0.030	0.15	0.15	0.345	0.5654	0.1490	0.077	0.1131	1.495
	0.050	0.13	0.13	0.663	0.9293	0.2238	0.046	0.1246	0.932
	0.070	0.16	0.09	0.754	0.9472	0.2009	0.023	0.1084	0.553
1V:3H	0.030	0.16	0.0776	0.323	0.3816	0.2101	0.155	0.2300	3.385
	0.050	0.16	0.0824	0.539	0.6770	0.1838	0.083	0.2300	0.930
	0.070	0.16	0.1600	0.754	1.0057	0.1027	0.013	0.2300	0.148
1V:6H	0.030	0.154	0.0778	0.336	0.3560	0.0440	0.0208	0.2452	0.137
	0.070	0.165	0.1200	0.731	0.8549	0.0533	0.0163	0.2345	0.043

#### 3.4.4 Comparison to open-channel flows over macro-roughness elements

The data gathered here corresponds to a considerably large Reynolds number (Figure 3.27), which for common macro-roughness would imply fully rough regime (independent of the Reynolds number).

Cheng (2017) extended the Manning-Strickler formula to flows over large-scale roughness. Cheng (2017) proposed that when flow is constricted by macro-roughness, the resistance increases with a different power law, related to the flow obstruction. Cheng presented the following formula:

$$f_b = 0.18 \left( \frac{k_s}{D_H} \right)^{1/3} \left( 1 - 1.5 \frac{k_s}{D_H} \right)^{-16/3} \quad (3.15)$$

This formula is an analytical modification of the MS formula, by accounting the area of the flow obstructed by the roughness and accounting for the corresponding increase in the flow velocity.

Herein obtained data best fits the expression:

$$f_b = K \left( \frac{k_s}{D_H} \right)^{10} \quad (3.16)$$

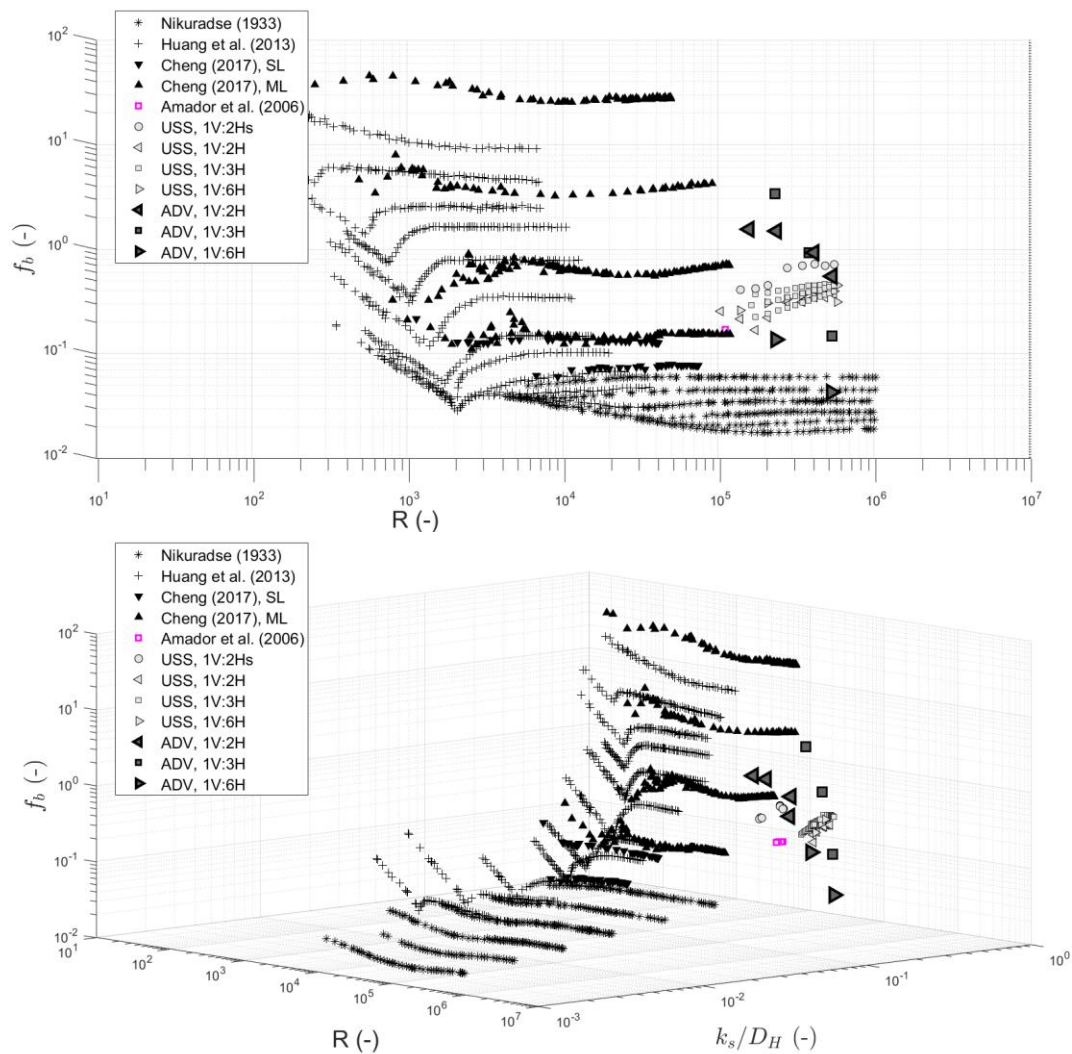
with  $K$  taking the values (obtained using ADV data only):  $4.18 \cdot 10^8$  (1V:2H),  $3.59 \cdot 10^6$  (1V:3H), and  $1.49 \cdot 10^5$  (1V:6H). USS data served to define the slope of Eq.(3.15), but given the scatter, only the data from the ADV was used to calibrate  $K$ . The scatter in the USS data may be attributed to the uncertainty related to the hypotheses done when deriving the friction factors. The scatter is clearly larger than data for pipe flows (Figure 3.28), however it is comparable to that scatter shown by Cheng (2017) for gravel bed data and to previously reported data on stepped spillways (Chanson et al. 2015).

### 3.4.5 Conclusions

The flow structure inside the three different cavities has been studied, both for single phase flow and aerated flows. Different techniques have been used for this purpose, including ADV, conductivity probe and high speed camera.

The results show that the flow structure changes with increasing length of the steps, which directly leads to decreased energy dissipation. Energy dissipation was also obtained through flow depths measurements, which required additional assumption of hydrostatic flow conditions (not met in reality). Yet, friction factor values were in the same order of magnitude of those obtained through velocimetry, thus endorsing those observations. Previous formulas for bed friction over macro-roughness (e.g., Eq.(3.15), see Cheng 2017) may fail to provide a realistic estimation of the friction factor since the cavity may not fulfil the role as macro-roughness once the flow reattaches in the case of large aspect ratios. Those estimations may result unsafe and thus Eq. (3.16) is recommended, which can account for the *smoothing* effect of this macro-roughness structures with large aspect ratios.

It may further be recommended that, when energy dissipation is to prime, the steps in coastal protection revetments should be designed with small aspect ratios (1V:2H, or 1V:3H).



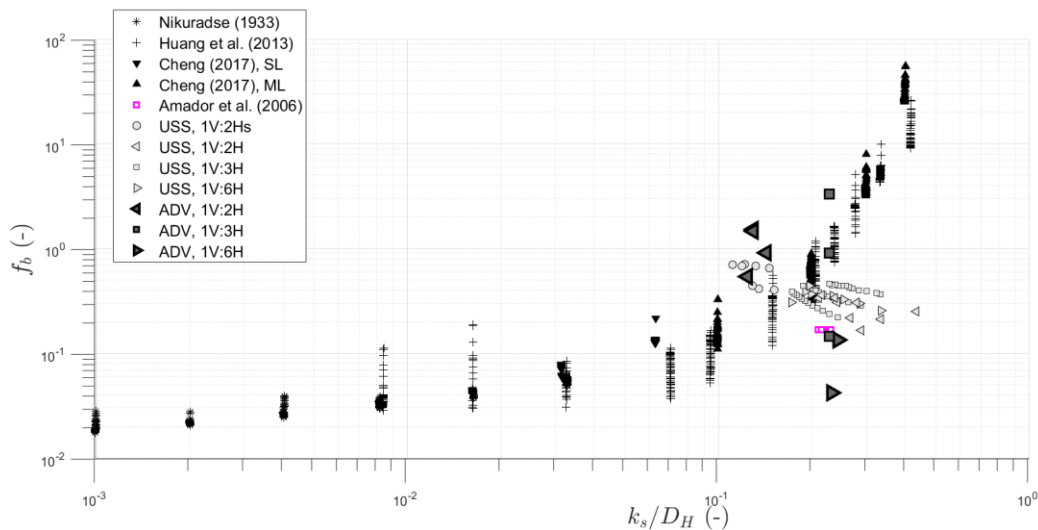


Figure 3.27. Friction factor of the stepped geometry, including Reynolds number effect. Data from USS and ADV. Previous data on macro-roughness for reference (SL: for single layer and ML for multi-layer). Data of Amador et al. (2006) corresponds to a stepped spillway.

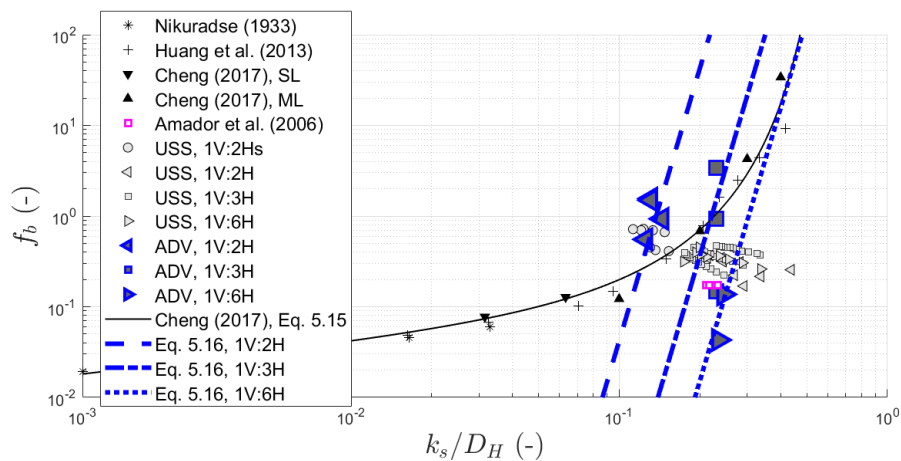


Figure 3.28. Friction factor of the stepped geometry, using Reynolds independent data. Data from USS and ADV. Previous data on macro-roughness for reference (SL: for single layer and ML for multi-layer). Data of Amador et al. (2006) corresponds to a stepped spillway and Cheng (2017) for rough pipe flows.

### 3.5 Grass-step interface

#### 3.5.1 Introduction

In order to evaluate occurring stresses and resulting erosion potential at the transition from a stepped revetment to an existing grass dike, additional tests have been performed using artificial grass of roughly three centimetres height (see. Figure 3.4 and Figure 3.5). Two different installations have been considered, i.e. the grass layer being 1) levelled with the step edges (setup GE) and 2) levelled with the step niche (setup GN).

All previously analysed cavities were tested for both grass setups again. In all tests, the grass covered half of the flume (i.e. 29 cm in width). It must be noted that no friction factor estimation has been performed for these cases, but instead this part of study focuses on the determination of turbulence and shear stresses occurring at the transition. Given the fact that the conductivity probe (1D) and imaging techniques (2D) are not capable to detect 3D effects and that a three-dimensional flow is expected at the transition, only the ADV probe has been used for this effort. As recommended by Koca et al. (2017), all data has been gathered considering the Sweet-Spot (SS) +/- 4 bins only as the ADV profiler performance

is known to be affected in the outer range of the profile when analysing turbulent quantities. Flow depths are again measured with Ultrasonic Sensors.

All velocity measurements presented in the subsequent section were obtained at the edge cross-section of the same step where ADV velocities were measured in the past section.

### 3.5.2 Results

All data is presented in a dimensionless form, relating the local quantities to the maximum free-stream velocity  $u_{fs}$  present at the cross-section.

Mean velocity fields are presented in Figure 3.29 for the GE setup, again exemplarily for the case with 1V:3H slope and  $Q = 50$  l/s discharge. It is found that the streamwise mean flow velocities  $\bar{u}_x$ , particularly at the bottom with  $z \approx 0$ , are lower over the grass than over the step cavity while no significant spanwise velocities  $\bar{u}_y$  occur (thus showing a 2D time-averaged flow field). The maximum free-stream velocity is found over the cavity.

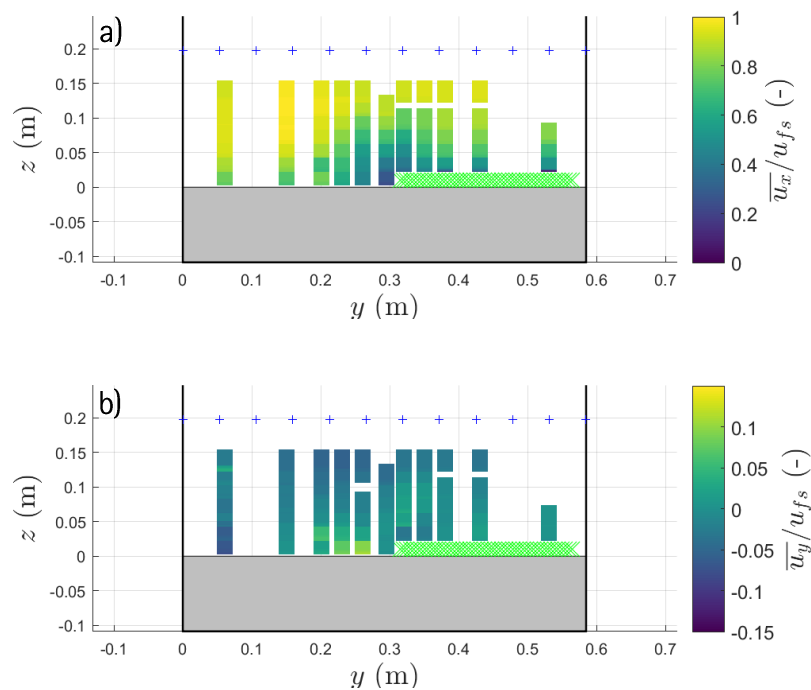


Figure 3.29. Mean velocity fields obtained with the ADV for 1V:3H and  $Q = 50$  l/s for experiments with grass at the step edge level (GE), velocities related to the centreline free-stream velocity, a) streamwise velocities, b) spanwise velocities

Figure 3.30 presents the mean velocity data for the GN setup and identical discharge and slope. The maximum free-stream velocity has shifted, now occurring over the grass. The water level remains unchanged, thus indicating a lower mean flow velocity in the cross-section (given the larger cross-section available). At the grass level low, relatively low flow velocities are found. As for the GE setup before, the spanwise velocities are about null across the cross-section.

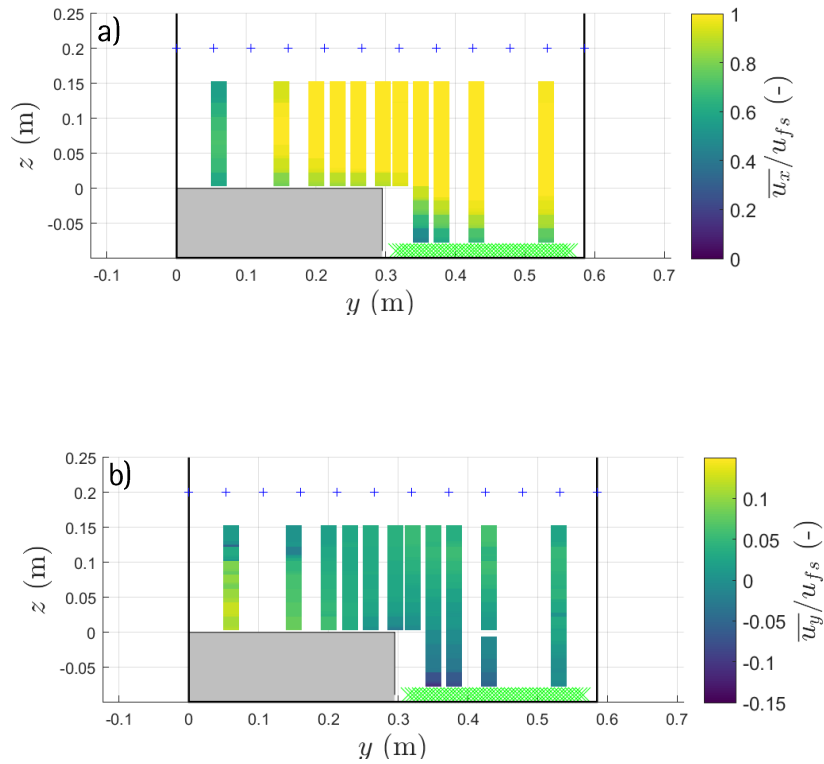
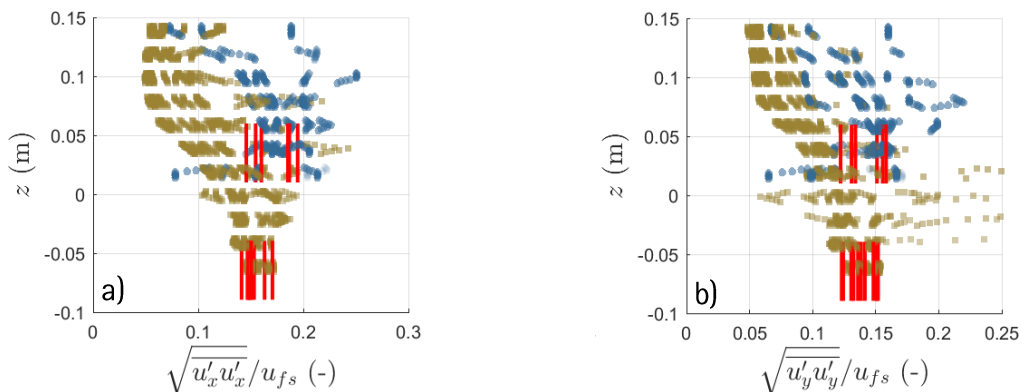


Figure 3.30. Mean velocity fields obtained with the ADV for 1V:3H and  $Q = 50$  l/s for experiments with grass at the step niche level (GN), velocities related to the centreline free-stream velocity, a) streamwise velocities, b) spanwise velocities

For both setups, the streamwise flow velocities near the grass level are constant in  $y$ -direction (setup GE) or even smaller at the direct vicinity of the transition when compared to the outer region at  $y = 0.58$  m (setup GN). This may suggest that bottom shear forces are of the same order or even smaller than on grass dikes without a stepped revetment. However, to address this question, turbulent quantities need to be analysed as well.

Figure 3.31 presents the turbulent normal stresses (Figure 3.31a-c) and turbulent kinetic energy (Figure 3.31d). Brown markers indicate the results for the GN setup and blue marker for the GE setup. Average stresses and turbulent kinetic energy at the grass level are shown as red lines for all cavities. The results suggest that turbulent quantities at the grass level are of the same order for both setups. In consequence, it appears that the setup has no influence on the erosion potential at the transition from the revetment to the grass dike.



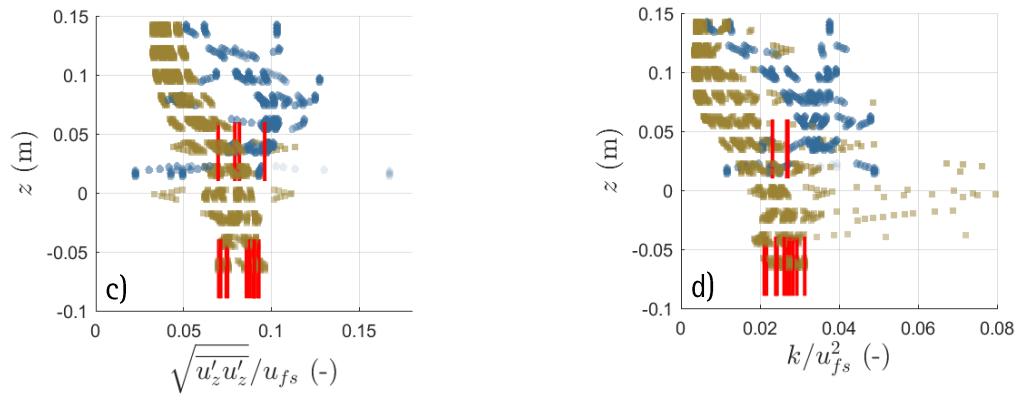


Figure 3.31. Turbulent normal stresses: a) streamwise, b) spanwise and c) normalwise; d) turbulent kinetic energy.  $u_{fs}$  corresponding to the maximum streamwise velocity measured in the complete section, squared (brown) markers for GN setups and circled (blue) markers for GE setups. Red bars correspond to the average normal stress (or turbulent kinetic energy) at the grass level for each setup.

Compared to the outer region, turbulent quantities are of the same order and it may be concluded that the stepped revetment should not generate additional erosion or scouring potential over the grassed surface (see Figure 3.32).

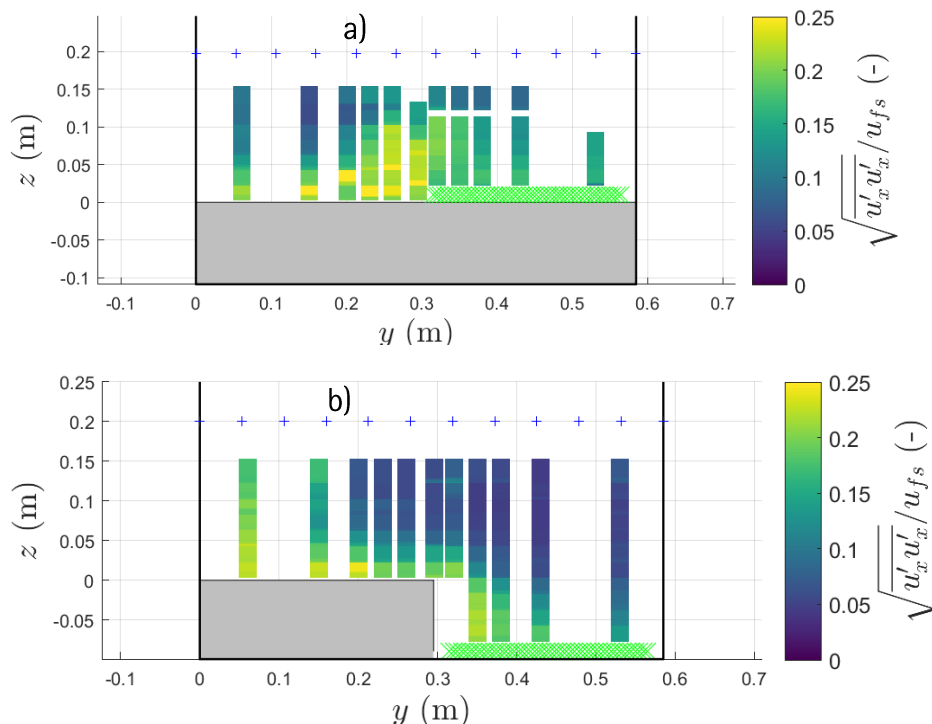


Figure 3.32 Streamwise (a) and spanwise (b) turbulence fields obtained with the ADV for 1V:3H and  $Q = 50$  l/s for experiments with grass at the step niche level (GN), data related to the centreline free-stream velocity

### 3.5.3 Conclusions

Compared to the outer region, turbulent quantities are of the same order and it may be concluded that the stepped revetment should not generate additional erosion or scouring potential over the grassed surface.

The results in Figure 3.32 (including data in the grass-step interface for all setups) suggests that peak turbulence (and thus stresses) values are relatively similar. Turbulence is not significantly higher with transition at step or niche levels.

### 3.6 Flow parameters of stepped revetments under regular waves

#### 3.6.1 Introduction

Small scale model tests were conducted in a wave flume to gain insight into the real flow conditions occurring when waves run up over the steps. Specific instrumentation for air-water flows (Conductivity Probe, CP) and Phantom M120 high-speed camera was installed at a 1V:2H stepped revetment setup.

The tests were carried out with regular wave conditions to tighten the flow parameters studied on steady flow conditions at FH Aachen. As a side goal, influence of some wave parameters (e.g., wave period, wave height and wave type) on the detailed air-water flow features was studied, over and below the Still Water Level (SWL) at different locations (Figure 3.35).

#### 3.6.2 Experimental setup and instrumentation

The physical model tests were conducted in the Schneiderberg wave flume (110 m long, 2.20 m wide, 2 m deep, see Section 2.1.1). The model was constructed from two premanufactured frames and several step elements, stretching across the whole flume width (Figure 3.33). For these tests a stepped revetment with a 1V:2H slope and step height  $S_h=0.05$  m was tested. The model was placed at a distance of 26.5 m from the wave maker next to the flume's observation window (Figure 3.34).

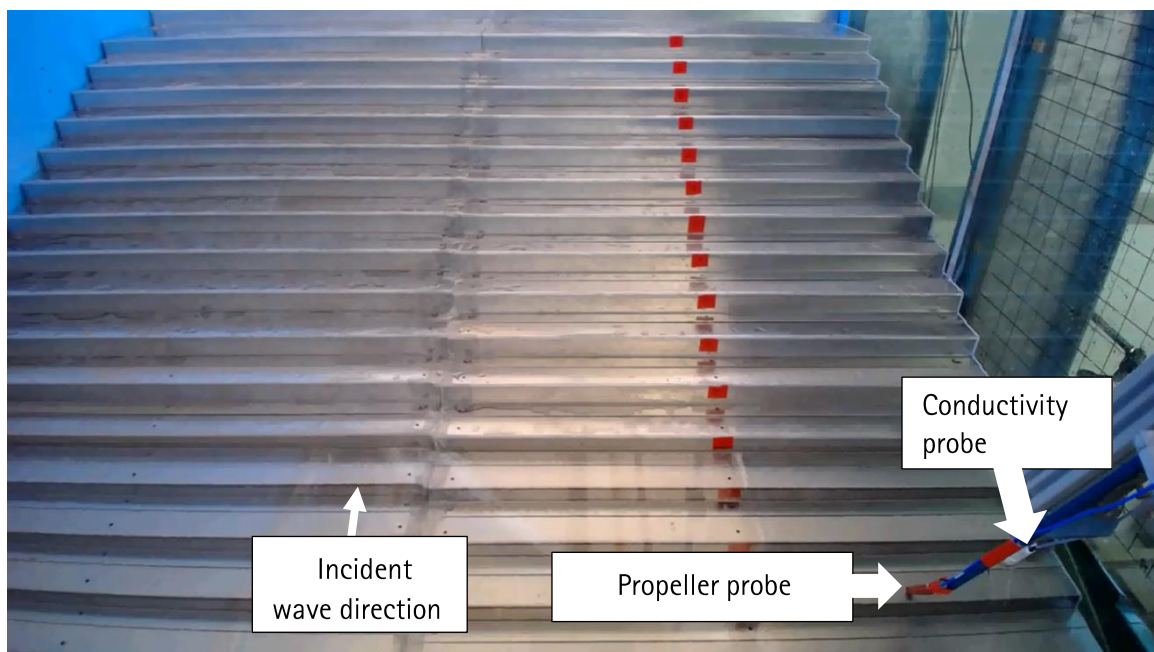


Figure 3.33: Stepped revetment  $S_h=0.05$  m model construction

#### Ultrasonic sensors (USS)

The surface elevation was simultaneously measured by a total of 10 ultrasonic sensors (USS) at a sampling frequency of 100 Hz. To measure the incident wave conditions, three of the USS were deployed to record the surface elevation half way between the model and the wave maker. Another USS was placed to measure the wave height at the toe of the structure, while the other 6 USS were placed on adjacent steps to measure the surface elevation during run-up events. Figure 3.35 indicates over which steps relative to the still water level, the USS (USS 2 to USS 7) were installed. The steps are numbered relative to the still

water level and the crest of the structure, i.e. step -2/13 is the second step below the still water level and the 13<sup>th</sup> step below the structure's crest.

#### Conductivity probe

The conductivity probe (CP) working principle is based upon a double simultaneous recording of the electric conductivity properties of the flow in contact with the probe. Cross-correlation of both signals allow the determination of the most probable lag time, which all together with the separation of the tips allow the interfacial velocity determination.

As only one conductivity probe could be used, the probe was moved to different locations between tests (Figure 3.35). In this way measurements at a range of locations along the wave run-up profile could be measured.

#### Velocity probe

A propeller probe was installed next to the conductivity probe to measure the velocity during wave run-up events. The utilisation of a propeller probe has limitations in these model tests, since it takes time to react with increasing and decreasing velocities. Also the change of flow direction between run-up and run-down influences the readings.

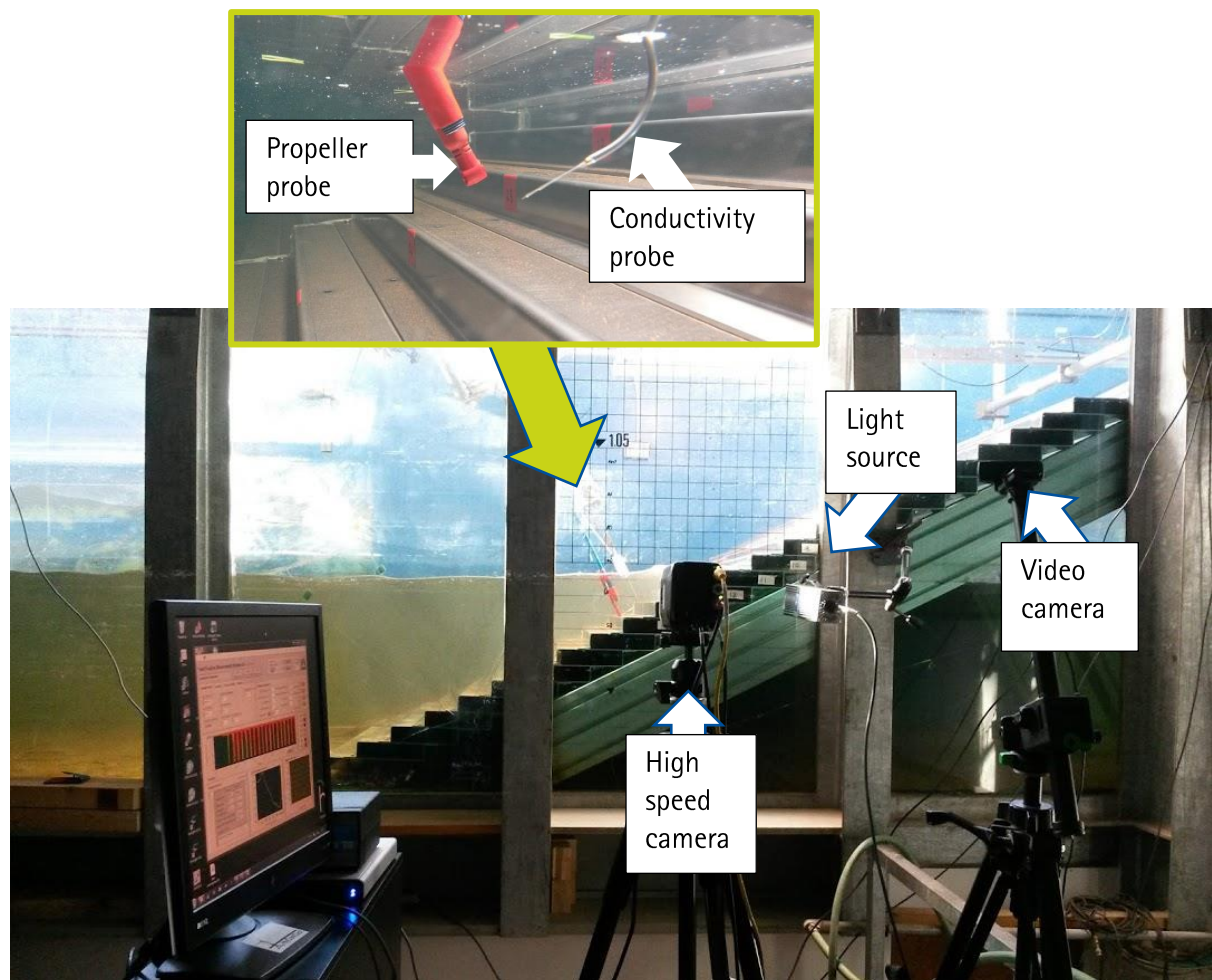


Figure 3.34: Instrumentation and view from observation window

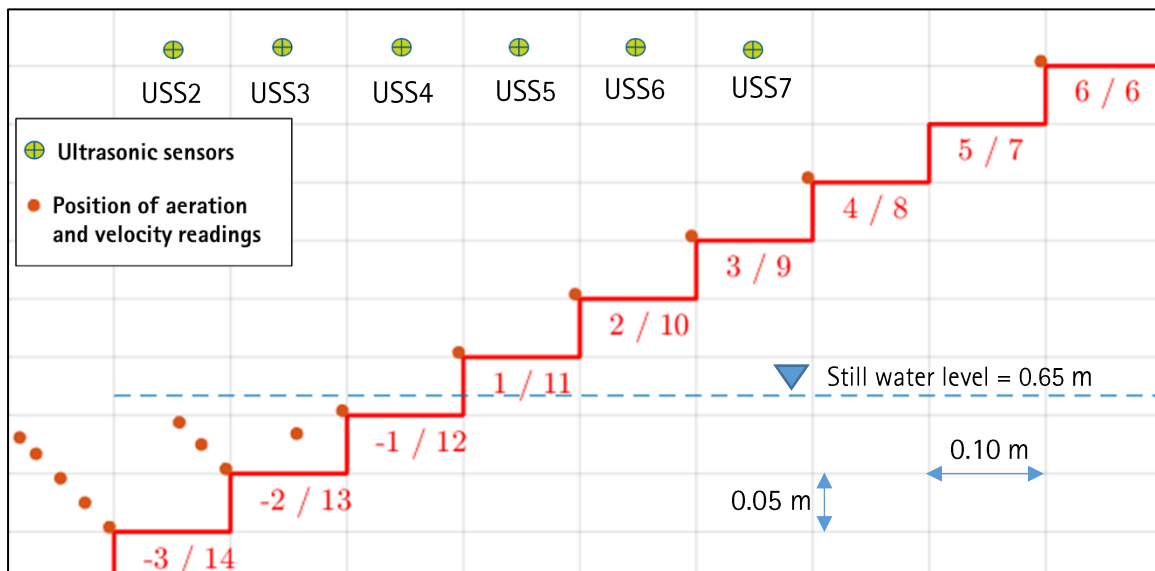


Figure 3.35: Overview of locations where the conductivity and propeller were installed

### 3.6.3 Test conditions

A total of 42 physical model tests with regular waves were conducted. The generated boundary conditions are in the following ranges:

$$1.7 < \xi < 3.4$$

$$3.4 < \frac{H}{S_h} < 5.1$$

$$0.02 < \frac{H}{L} < 0.08$$

$$0.08 < \frac{h}{L} < 0.24$$

Where,  $\xi = \tan\alpha/(H/L)^{1/2}$  is the surf similarity,  $H$  is the regular wave height,  $S_h$  is the step height,  $L$  is the wave length and  $h$  is the water depth.

### 3.6.4 Flow processes

Several waves were captured in each recording, thus allowing ensemble averaging of the results. The first wave was always discarded as wave impact hydrodynamics and aeration is not representative of the "expected" flow. The ten subsequent waves were taken into account for the data analysis and the following ones were again discarded as they could be affected by wave reflection (no wave absorption during the tests).

An exemplary regular waves test is shown in Figure 3.36 and Figure 3.37, with wave height  $h_s = 0.65$  m and wave period  $T_p = 2.21$  s; the measuring tips of the conductivity probe are located at the SWL. In Figure 3.36, several snaps of the run-up process can be observed. With the wave impact, the highest levels of aeration occur. After that, the concentration levels are slowly decaying, likewise the run-up flow velocity decreases. With lower flow velocities, the air transport capacity of the flow also drops and hence bubbles rise easily, thereby deaerating the flow. During the run-down process, the flow initially shows a

jet regime having small jets impacting from step to step with a small recirculation region occurring in the inside of the cavity. Quickly, the falling flow develops into a skimming flow regime (Figure 3.36d).

Analysis of the data gathered with the CP allows insight into the bubble/droplets dynamics. When the probe is surrounded by water, the measured voltage remains at an upper level. Otherwise, when the tip is surrounded by air, the voltage drops to a lower level crossing a threshold value which has been taken as 0.5 by default. When the probe is initially surrounded by water, the test corresponds to a measurement below the SWL. In that case, the first wave is noted as the first air–water interface is detected ( $t = 8.45$  s in Figure 3.37). The impacting flow is highly aerated with a decreasing concentration as time advances. After roughly 0.60 s, the run-up has reached the highest potential energy level and starts reversing: the run-down process starts. After the last interface is detected, the wave is completely over. Waves are detected following this strategy and then later analysed individually allowing a final ensemble averaging of the results. A similar strategy was also established for the analysis of the data gathered over the SWL, being the CP initially in contact with air.

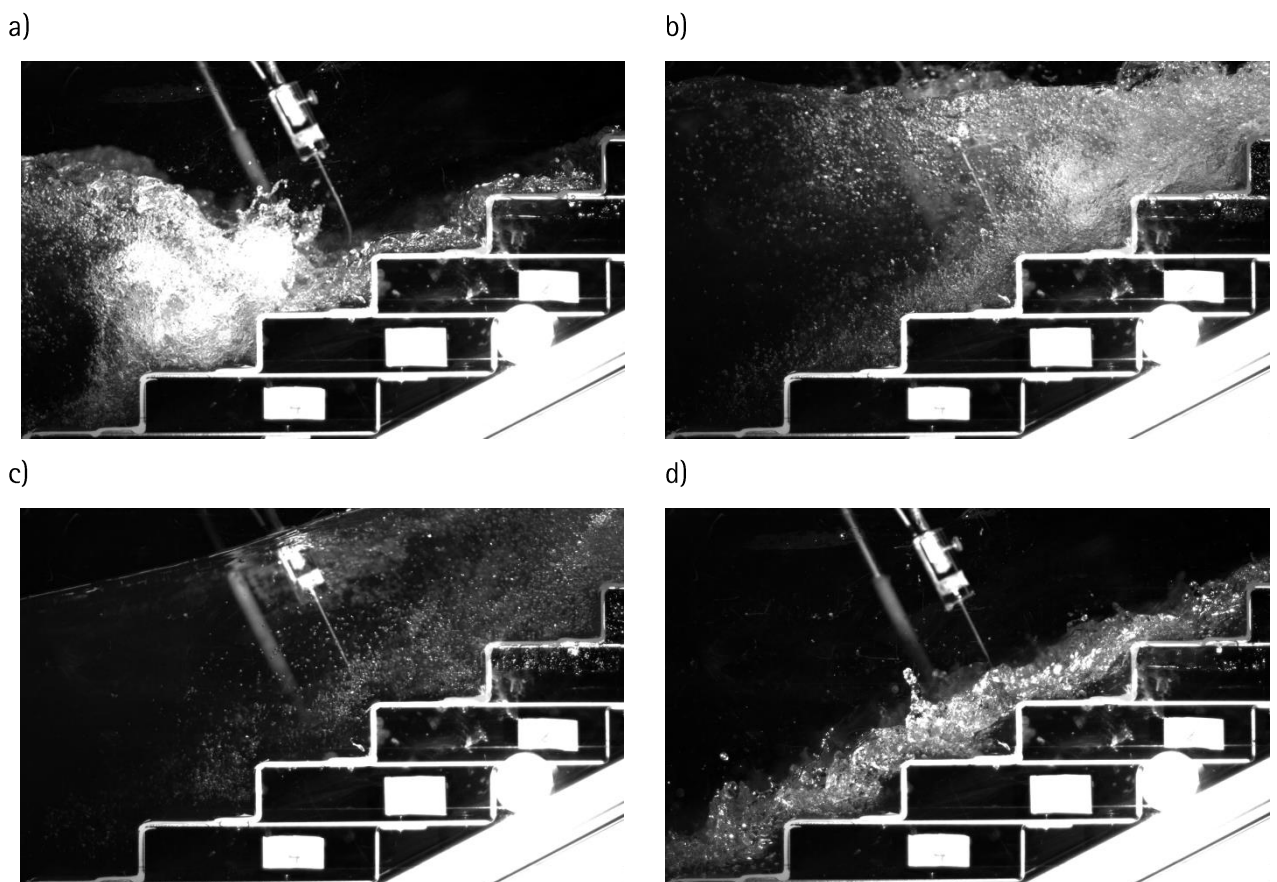


Figure 3.36: Test with CP located with the tips at the SWL. a) Wave impacting against the CP tips (lag time  $\tau = 0$  s); b) wave run-up (lag time  $\tau = 0.217$  s); c) maximum reach of the wave run-up (lag time  $\tau = 0.602$  s); and d) wave run-down, aerated skimming flow over the steps.

Figure 3.37 also shows that certain variability is present across the analysed wave events at a single recording. For the sake of simplicity, it is here not shown the autocorrelation functions for the aeration duration, but each event has shown to be independent from the others (i.e., aeration at a given wave is not affected by the wave history but seems as a pseudo-random event).

The aeration duration also varied with the flow depth at which the CP was located. Close to the steps, the aeration levels remained small (around 20 to 30 % of the wave period) whereas for the upper locations, the aeration levels persisted longer times (up to 90 % of the wave period). Velocities also seemed to follow that pattern.

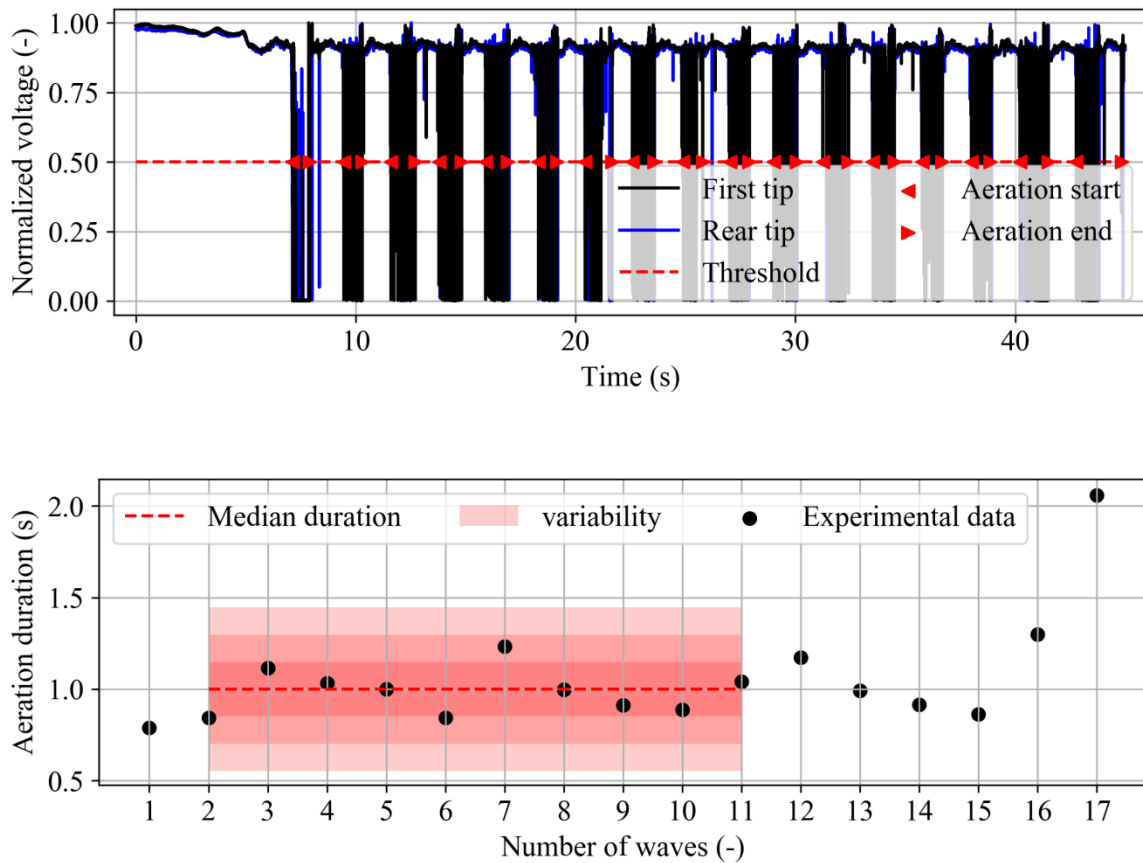


Figure 3.37. Data extracted from the CP signal, located at the SWL. Top: Waves automatically detected when probe is wet/dry (high/low voltages), period computed with the CP correspond to 1.18 s (-1.52 % relative to the wave generated); bottom: duration of the aeration (as defined in the top image, mean value of 1.0 s). Figure A1 correspond to the wave shown around Time  $\approx$  10 s (wave #2).

## 4 Discussion

### 4.1 Stepped revetment geometry: recommendations

The investigation of steady flows over stepped revetment cross-sections showed that turbulence quantities occurring over steps are mainly in the same order of magnitude of those in boundary layers flows over macro-roughness. When the cavity of the steps allow the formation of a big roller structure, large streamline curvature is caused and enhanced energy dissipation can be achieved. The step geometry thus governs the vortex formation, which implies that it can be expected that stepped revetments with small aspect ratios (i.e. steeper revetment slopes) will be more effective in energy dissipation. This was proven by comparing the flow structures of three stepped revetment slopes (1V:2H, 1V:3H and 1V:6H) by applying different techniques, including ADV, conductivity probe and high speed camera. A different flow structure was found for the 1V:6H stepped revetment cross-section. Here the flow reattached parallel to the smooth horizontal face and hence the recirculation is considerably disturbed, which result in lower friction factors. From the perspective of steady flows, it is thus recommended to design stepped revetments with smaller aspect ratios (1V:2H, or 1V:3H).

In the wave flume experiments with breaking waves, it was also found that the 1V:6H revetment, compared to the 1V:3H, was less effective in reducing wave overtopping. However, still a significant reduction in overtopping, around 35%, was achieved compared to a smooth slope. A stepped revetment with 1V:1H slope has shown to be less effective in reducing wave overtopping than the 1V:2H or 1V:3H slopes. For optimum wave overtopping reduction of up to 65 %, a characteristic step height in the range of  $0.5 \leq \cos\alpha \cdot S_h / H_{m0} \leq 2$  is recommended.

### 4.2 Flow processes of stepped revetments with varying step heights

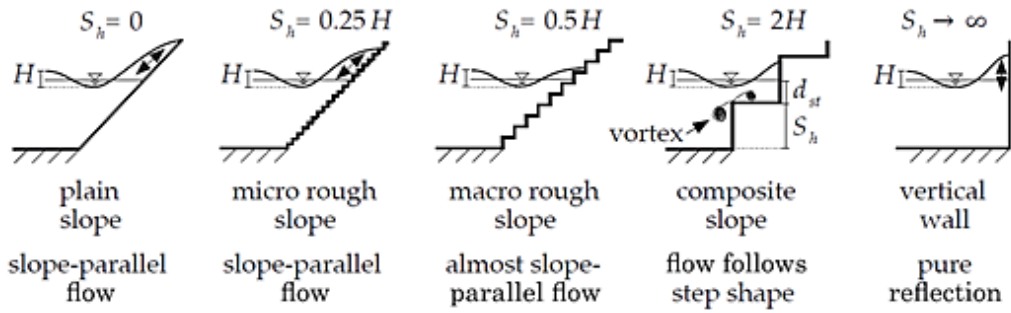
The flow conditions for stepped revetments related to step ratios and characteristic step heights are summarised in Figure 4.1. Two illustrative extreme cases of stepped revetments are considered: on the one extremity a smooth slope where  $S_h=0$  m, while on the other, a vertical wall where  $S_h \rightarrow \infty$ . For a smooth or plain slope, the flow during wave run-up is parallel to the slope and there is negligible influence of slope roughness, as is the case for concrete slopes.

With increasing step heights ( $S_h < H$ ), the slope roughness of the steps begins to have an influence on the wave run-up, as low turbulence is induced in the step cavities. The steps of the revetment are considered micro roughness as minor energy dissipation occur and flows are still slope parallel.

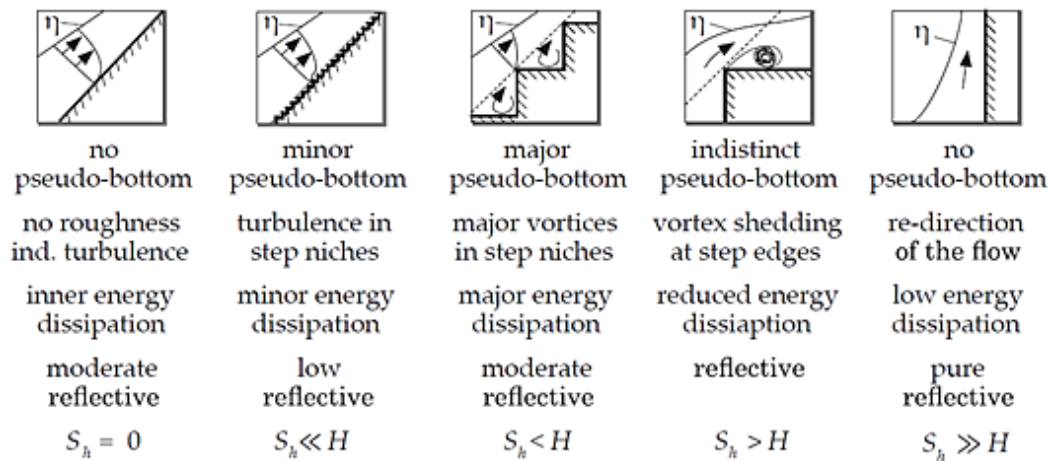
As the step height further increases ( $S_h < H$ ), the flow is substantially influenced by the steps. The flow is still almost parallel, but a distinct pseudo-bottom is present with recirculating vortices. Major turbulence is induced and optimum wave run-up and overtopping reduction occur for  $0.5 < \cos\alpha \cdot S_h / H_{m0} < 2$ .

When the step height becomes larger than the wave height ( $S_h >> H$ ) nappe flow occurs as the flow follows the shape of the steps. Reduced energy dissipation is achieved and the structure becomes highly reflective. As the step height further increases, the other extremity of a vertical wall is reached, where the structure becomes purely reflective.

global flow conditions:



local flow conditions:



qualitative overtopping volume:

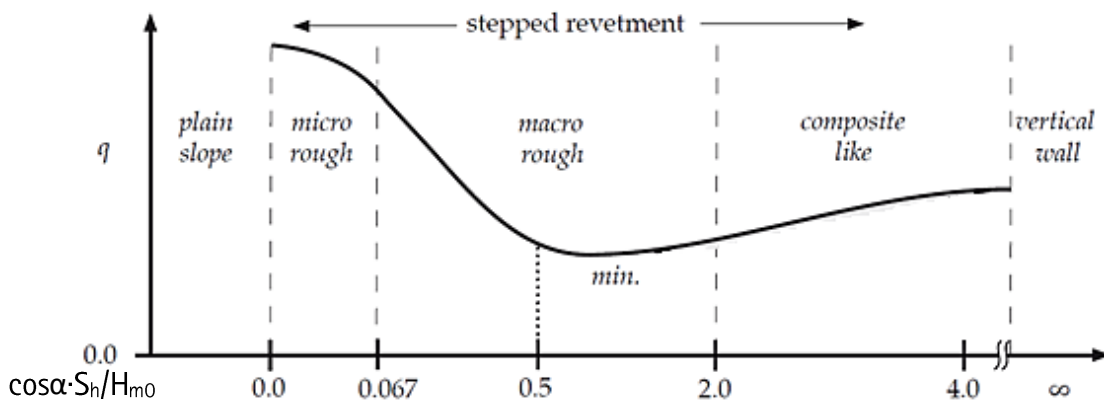


Figure 4.1. Flow processes based on the characteristic step height (Kerpen et al. 2019)

## 5 Conclusions

Steady flow investigations and wave flume experiments were conducted to research the effectivity of a stepped revetment to reduce wave run-up and wave overtopping in comparison to a smooth slope. Flow structures on various revetment geometries revealed that smaller aspect ratios of the step cavities lead to enhanced energy dissipation.

With the wave flume tests a stepped revetment's ability to reduce wave run-up and overtopping were quantified by calculating roughness factors ( $\gamma_f$ ) for a wide range of geometries and wave conditions. A roughness factor of  $\gamma_f=0.7$  for wave run-up was determined based on large scale tests. Roughness factors, derived in small scale, were lower, thus suggesting they are influenced by scale effects. This results in the underestimation of wave run-up heights.

For wave overtopping it was established that the roughness factor is influenced by the revetment's aspect ratio (represented by  $\cos\alpha \cdot S_n$ ) and the incident wave height ( $H_{m0}$ ). An optimum reduction in wave overtopping of 65% can be achieved at  $\cos\alpha \cdot S_n/H_{m0}=1.2$ . A comparison between large and small scale data could not directly quantify scale effects. However, the large scale data show higher roughness factors compared to the prediction by Van Steeg et al. (2018) which was conducted under comparable conditions in small scale.

## References

- Adrian, R. J. and Westerweel, J.: Particle Image Velocimetry. Cambridge University Press, 2011.
- Amador, A., Sánchez-Juny, M. and Dolz, J. (2006). Characterization of the nonaerated flow region in a stepped spillway by PIV. *Journal of Fluids Engineering*, 128(6), 1266-1273.
- Antonia, R. A., and Krogstad, P. Å. (2001). Turbulence structure in boundary layers over different types of surface roughness. *Fluid Dynamics Research*, 28(2), 139-157.
- Brand, A.; Noss, C.; Dinkel, C. and Holzner, M.: High-resolution measurements of turbulent flow close to the sediment-water interface using a bistatic acoustic profiler. *Journal of Atmospheric and Oceanic Technology*, 33(4), 769-788, 2016.
- Bung, D. B. and Valero, D.: Application of the Optical Flow Method to Velocity Determination in Hydraulic Structure Models, 6th International Symposium on Hydraulic Structures, Portland, 2016b.
- Bung, D. B. and Valero, D.: FlowCV – An open-source toolbox for computer vision applications in turbulent flows, 37th IAHR World Congress, Kuala Lumpur, 2017.
- Bung, D. B. and Valero, D.: Optical flow estimation in aerated flows, *Journal of Hydraulic Research* 54(5), 575-580, 2016a.
- Cameron, S. M., Nikora, V. I., and Stewart, M. T. (2017). Very-large-scale motions in rough-bed open-channel flow. *Journal of Fluid Mechanics*, 814, 416-429.
- Cartellier, A. and Achard, J. L.: Local phase detection probes in fluid/fluid two-phase flows. *Review of Scientific Instruments*, 62(2), 279-303, 1991.
- Castro-Orgaz, O. and Hager, W. H.: Non-hydrostatic Free Surface Flows. Springer, Advances in geophysical and Environmental Mechanics and Mathematics. ISBN: 978-3-319-47969-9, 2017.
- Chamani, M. R., and Rajaratnam, N. (1999). Characteristics of skimming flow over stepped spillways. *Journal of Hydraulic Engineering*, 125(4), 361-368.
- Chang, K. A.; Lim, H. J. and Su, C. B.: Fiber optic reflectometer for velocity and fraction ratio measurements in multiphase flows. *Review of scientific instruments*, 74(7), 3559-3565, 2003.
- Chanson, H. and Toombes, L. (2002). Experimental investigations of air entrainment in transition and skimming flows down a stepped chute. *Canadian Journal of Civil Engineering*, 29(1), 145-156.
- Chanson, H., and Toombes, L. (2004). Hydraulics of stepped chutes: The transition flow. *Journal of Hydraulic Research*, 42(1), 43-54.
- Chanson, H., Bung, D. B., Matos, J. (2015). Stepped spillways and cascades. In: Energy dissipation in hydraulic structures. IAHR monograph. CRC Press, Taylor & Francis Group, Leiden, Netherlands.
- Chanson, H.: Air Bubble Entrainment in Free-Surface Turbulent Shear Flows. San Diego, USA: Academic Press, 1996.
- Chanson, H.: Hydraulics of aerated flows: qui pro quo?. *Journal of Hydraulic Research*, 51(3), 223-243, 2013.
- Chanson, H.: The Hydraulics of Stepped Chutes and Spillways. Lisse, Niederlande: A. A. Balkema, 2002.
- Cheng, N.-S.: Simple Modification of Manning-Strickler Formula for Large-Scale Roughness. *Journal of Hydraulic Engineering*, 143(9), 04017031. doi: 10.1061/(ASCE)HY.1943-7900.0001345, 2017.

- Dai, Y. B. and Kamel, A. M. (1969). Scale effect tests for rubble-mound breakwaters: Hydraulic model investigation. U S Waterways Experiment Station-Research Report H-69-2, (69-2).
- Dey, S., and Lambert, M. F. (2005). Reynolds stress and bed shear in nonuniform unsteady open-channel flow. *Journal of hydraulic engineering*, 131(7), 610-614.
- Einstein, H. A. (1934). Der hydraulische oder Profilradius. *Schweizer Bauzeitung*, 103(8), 89-91.
- Einstein, H. A. (1948). Formulas for the transportation of bedload. *Transactions of ASCE*, 107, 561-597.
- EurOtop, 2018. Manual on wave overtopping of sea defences and related structures. An overtopping manual largely based on European research, but for worldwide application. Van der Meer, J.W., Allsop, N.W.H., Bruce, T., De Rouck, J., Kortenhaus, A., Pullen, T., Schüttrumpf, H., Troch, P. and Zanuttigh, B.
- Felder, S. and Chanson, H. (2009). Turbulence, dynamic similarity and scale effects in high-velocity free-surface flows above a stepped chute. *Experiments in Fluids*, 47(1), 1-18.
- Felder, S., & Chanson, H. (2017). Scale effects in microscopic air-water flow properties in high-velocity free-surface flows. *Experimental Thermal and Fluid Science*, 83, 19-36.
- Felder, S., and Chanson, H. (2015). Simple design criterion for residual energy on embankment dam stepped spillways. *Journal of Hydraulic Engineering*, 142(4), 04015062.
- Frizell, K. W. (2000). Effects of aeration on the performance of an ADV. In: Joint Conference on Water Resources Engineering and Water Resources Planning and Management, Symposium on Modern Velocity and Discharge Measurement Techniques and Application, July 20 – August 2, 2000.
- Frostick, L. E., McLelland, S. J., and Mercer, T. G. (2011). Users guide to physical modelling and experimentation: Experience of the HYDRALAB network. Leiden, The Netherlands: CRC Press/Balkema, 1st ed. edition.
- Gallach-Sánchez, D. 2018. Experimental Study of Wave Overtopping Performance of Steep Low-Crested Structures. Ghent University
- Goda, Y. and Kishira, X. (1976). Experiments on irregular wave overtopping characteristics of seawall of low crest types. *TN of PARI*, (242).
- Goring, D. G. and Nikora, V. I. (2002). Despiking acoustic Doppler velocimeter data. *Journal of Hydraulic Engineering*, 128(1), 117-126.
- Graf, W. H., and Song, T. C. (1995). Bed-shear stress in non-uniform and unsteady open-channel flows. *Journal of Hydraulic Research*, 33(5), 699-704.
- Guo, J. (2014). Sidewall and non-uniformity corrections for flume experiments. *Journal of Hydraulic Research*, 53(2), 218-229.
- Guo, J.: Exact procedure for Einstein-Johnson's sidewall correction in open channel flow. *Journal of Hydraulic Engineering*, 143(4), 06016027, 2016.
- Hampel, F. R.: The influence curve and its role in robust estimation. *Journal of the American Statistical Association*, 69(346), 383-393, 1974.
- Heimbaugh, M. S. (1988). Coastal engineering studies in support of Virginia Beach, Virginia, Beach Erosion Control and Hurricane Protection Project: Report 1, Phys. model tests of irregular wave overtopping and pressure meas., volume 88-1 of CERC. Springfield, Va.
- Heller, V. (2011). Scale effects in physical hydraulic engineering models. *Journal of Hydraulic Research*, 49(3), 293-306.

- Hurther, D., and Lemmin, U. (2001). A correction method for turbulence measurements with a 3D acoustic Doppler velocity profiler. *Journal of Atmospheric and Oceanic Technology*, 18(3), 446–458.
- Jachowski, R. A. (1964). Interlocking precast concrete block seawall. *Coastal Engineering Proceedings*, (1(9)).
- Jimenez, J. (2004). Turbulent flows over rough walls. *Annu. Rev. Fluid Mech.*, 36, 173–196.
- Jones Jr, O. C. and Delhaye, J. M.: Transient and statistical measurement techniques for two-phase flows: a critical review. *International Journal of Multiphase Flow*, 3(2), 89–116, 1976.
- Kass, R. E.; Carlin, B. P.; Gelman, A. and Neal, R. M.: Markov chain Monte Carlo in practice: a roundtable discussion. *The American Statistician*, 52(2), 93–100, 1998.
- Kerpen, N. and Schlurmann, T., 2016. Stepped revetments – revisited. *Proceedings of the 6th International Conference on the Application of Physical Modelling in Coastal and Port Engineering and Science (Coastlab16)*.
- Kerpen, N. B., Goseberg, N. and Schlurmann, T. (2014). Experimental Investigations on Wave Overtopping on Stepped Embankments: Proc. 5th Int. Conf. on Appl. of physical modelling to port and coastal protection, vol. 14. Black Sea Coastal Research Ass., Varna.
- Kerpen, N., T. Schoonees, and T. Schlurmann. 2018. Wave Impact Pressures on Stepped Revetments. *Journal of Marine Science and Engineering*. 6:156. doi: 10.3390/jmse6040156
- Kerpen, N.B., T. Schoonees, and T. Schlurmann. 2019. Wave Overtopping of Stepped Revetments. *Water*. 11:1035. doi: 10.3390/w11051035
- Kim, J., Moin, P., and Moser, R. (1987). Turbulence statistics in fully developed channel flow at low Reynolds number. *Journal of fluid mechanics*, 177, 133–166.
- Klebanoff, P. (1955). Characteristics of turbulence in boundary layer with zero pressure gradient.
- Koca, K., Noss, C., Anlanger, C., Brand, A., and Lorke, A. (2017). Performance of the Vectrino Profiler at the sediment–water interface. *Journal of Hydraulic Research*, 1–9.
- Krecic, M. R. and Sayao, O. J. (2003). Wave overtopping on Chicago shoreline revetment. *Coastal Structures*, pages 542–554.
- Krogstad, P. Å., & Antonia, R. A. (1999). Surface roughness effects in turbulent boundary layers. *Experiments in fluids*, 27(5), 450–460.
- Landau, L.D. and Lifshitz, E. M. (1987). *Fluid Mechanics. Course of Theoretical Physics, Volume 6*, 2<sup>nd</sup> edition. Elsevier, Butterworth Heinemann.
- Leng, X. and Chanson, H.: Unsteady turbulence during the upstream propagation of undular and breaking tidal bores: An experimental investigation. Rep. No. CH98/15. Brisbane, Australia, Univ. of Queensland, 2015.
- Leonardi, S., Orlandi, P. and Antonia, R. A. (2007). Properties of d- and k-type roughness in a turbulent channel flow. *Physics of Fluids*, 19(12), 125101.
- Lozano-Durán, A., and Jiménez, J. (2014). Effect of the computational domain on direct simulations of turbulent channels up to  $Re_{\tau} = 4200$ . *Physics of Fluids*, 26(1), 011702.
- Lykke Andersen, T., H. Burcharth, and X. Gironella. 2011. Comparison of new large and small scale overtopping tests for rubble mound breakwaters. *Coastal Engineering*. 58:351–373. doi: 10.1016/j.coastaleng.2010.12.004

- MacVicar, B. J.; Dilling, S.; Lacey, R. W. J. and Hipel, K.: A quality analysis of the Vectrino II instrument using a new open-source MATLAB toolbox and 2D ARMA models to detect and replace spikes. In: Proceedings of the River Flow Conference, 1951-1959, 2014.
- Manning, R. (1895). On the flow of water in Open Channels and Pipes. Transactions of the Institution of Civil Engineers of Ireland, Dublin, 20, pp. 161-207.
- Marusic, I., McKeon, B. J., Monkewitz, P. A., Nagib, H. M., Smits, A. J., and Sreenivasan, K. R. (2010). Wall-bounded turbulent flows at high Reynolds numbers: Recent advances and key issues. *Physics of Fluids*, 22(6), 065103.
- Monin, A. S., & Yaglom, A. M. (2007). *Statistical fluid mechanics, volume II: mechanics of turbulence* (Vol. 2). Courier Corporation.
- Montes, S. (1998). *Hydraulics of Open Channel Flow*. ASCE Press.
- Montes, S. (1998). *Hydraulics of Open Channel Flow*. ASCE Press.
- Morris, H. M. (1968). Design of Roughness Elements for Energy Dissipation in Highway Drainage Chutes. Highway Research Record.
- Mrokowska, M. M., Rowiński, P. M. and Kalinowska, M. B. (2015). Evaluation of friction velocity in unsteady flow experiments. *Journal of Hydraulic Research*, 53(5), 659-669.
- Nezu, I., and Rodi, W. (1986). Open-channel flow measurements with a laser Doppler anemometer. *Journal of Hydraulic Engineering*, 112(5), 335-355.
- Nikora, V. I., Koll, K., McLean, S. R., Ditrich, A., & Aberle, J. (2002). Zero-plane displacement for rough-bed open-channel flows. In *Fluvial Hydraulics River Flow 2002* (pp. 83-92).
- Nikuradse, J. (1926). *Untersuchungen über die Geschwindigkeitsverteilung in turbulenten Strömungen*. Thesis, Göttingen, VDI Forschungsheft 281.
- Nikuradse, J. (1932). *Gesetzmäßigkeit der turbulenten Strömungen in glatten Röhren*. VDI Forschungsheft 356.
- Nussbaum, P. J. and Colley, B. E. (1971). *Dam construction and facing with soil-cement*. Research and Development Bul. PCA, Chicago
- O'Shaughnessy, M. M., Perry, L., Haupt, L. M., Leeds, C. T., and Fowler, C. E. (1924). *Ocean Beach Esplanade, San Francisco, California*. American Society of Civil Engineers, [New York]
- Oertel, M., and Schlenkhoff, A. (2012). Crossbar block ramps: Flow regimes, energy dissipation, friction factors, and drag forces. *Journal of Hydraulic Engineering*, 138(5), 440-448.
- Pagliara, S., and Chiavaccini, P. (2006). Flow resistance of rock chutes with protruding boulders. *Journal of Hydraulic Engineering*, 132(6), 545-552.
- Pfister, M., and Chanson, H. (2012). Scale effects in physical hydraulic engineering models By VALENTIN HELLER, *Journal of Hydraulic Research*, Vol. 49, No. 3 (2011), pp. 293-306. *Journal of Hydraulic Research*, 50(2), 244-246.
- Pope, S. B. (2000). *Turbulent flows*. Cambridge University Press.
- Rice, C. E., K. C. Kadavy, and K. M. Robinson (1998). Roughness of loose rock riprap on steep slopes. *Journal of Hydraulic Engineering* 124(2), pp. 179-185.
- Ross, S. M.: *Introduction to Probability and Statistics for Engineers and Scientists*. Elsevier, Fourth Edition, 2009.

- Rousseeuw, P. J. and Croux, C.: Alternatives to the median absolute deviation. *Journal of the American Statistical Association*, 88(424), 1273–1283, 1993.
- Saville, T. (1955). Laboratory data on wave run-up and overtopping on shore structures, volume no. 64 of Technical memorandum – Beach Erosion Board. U.S. Beach Erosion Board, Washington, D.C.
- Saville, T. (1956). Wave run-up on shore structures. *Proceedings of the American Society of Civil Engineering*, (952-WW2):1–14.
- Saville, T. (1957). Wave run-up on composite slopes. U.S. Beach Erosion Board, pages 691–699.
- Schlichting, H. (1968). *Boundary-layer theory*. McGraw-Hill series in mechanical engineering.
- Schoonees, T.; Kerpen, N.B.; Liebisch, S.; Schlurmann, T.(2018). Wave overtopping prediction of a gentle sloped stepped revetment. *Coast. Eng. Proc.* 2018, 1, 99.
- Soares-Frazão, S. and Fent, I. (2016). Experimental evaluation of the friction slope in unsteady flows. In *River Flow 2016* (pp. 358–364). CRC Press.
- Song, T. C., and Graf, W. H. (1996). Velocity and turbulence distribution in unsteady open-channel flows. *Journal of Hydraulic Engineering*, 122(3), 141–154.
- Steendam, G.J., J. van der Meer, P. van Steeg, and R. Joosten. 2018. Wave impacts at small and real scale for the stepped sloped seawall design at den oever. *Proceedings of the Coastal Engineering Conference*. 36: doi: 10.9753/icce.v36.papers.51
- Stoa, P. N. (1978). Reanalysis of wave run-up on structures and beaches, CERCTP- 78-2. Coastal Eng. Research Center, Fort Belvoir.
- Tabata, T., Shibata, K., and Yagyu, T. (1980). Compilation of existing design data of stepped face seawall. Technical Note of the Port and Harbour Research Institute, Ministry of Transport, (346).
- Takayama, T., Nagai, T., and Nishida, K. (1982). Decrease of wave overtopping amount due to seawalls of low crest types. Report of The Port and Harbour Research Institute, (21(2) (in Japanese)):151–206.
- TAW (2002). Technical Report Wave Run-up and Wave Overtopping at Dikes, Technical Advisory Committee on Flood Defence (TAW), Delft.
- Thomas, R. E.; Schindfessel, L.; McLelland, S. J.; Creëlle, S. and De Mulder, T.: Bias in mean velocities and noise in variances and covariances measured using a multistatic acoustic profiler: the Nortek Vectrino Profiler. *Measurement Science and Technology*, 28(7), 075302, 2017.
- Tozzi, M. J. (1994). Residual energy in stepped spillways. *International water power & dam construction*, 46(5), 32–34.
- USACE (1984). *Shore protection manual*. U.S. Army Corps of Engineers, Washington, 4th edition.
- Valero, D. and Bung, D. B.: Reformulating self-aeration in hydraulic structures: Turbulent growth of free surface perturbations leading to air entrainment. *International Journal of Multiphase Flow*, 100, 127–142, 2018a.
- Valero, D. and Bung, D. B.: Vectrino Profiler Spatial Filtering for Shear Flows Based on the Mean Velocity Gradient Equation. *Journal of Hydraulic Engineering*, 144(7), 2018b.
- Vallejos, R. and Osorio, F.: Effective sample size of spatial process models. *Spatial statistics*, 9, 66–92, 2014.
- Van Steeg, P., (2012). Influence factor due to roughness on overtopping of a stair-shaped slope at dike revetments (in Dutch, original title: Invloedsfactor voor ruwheid van een getrappt talud bij golfoverslag bij dijken: Verslag fysieke modeltesten en analyse), Deltares report 1206984-000-HYE-0006, (unpublished).

- Van Steeg, P., R.A. Joosten, and G.J. Steendam. 2018. Physical model tests to determine the roughness of stair shaped revetments. 3th International Conference on Protection against Overtopping, UK. 1–8.
- Wahl, T. L.: "Discussion of 'Despiking acoustic Doppler velocimeter data' by Derek G. Goring and Vladimir I. Nikora." *Journal of Hydraulic Engineering*, 129(6): 484–487, 2003.
- Ward, D. L. (2003). Overtopping Studies of a Stepped Revetment for City of Chicago, Illinois. Defense Technical Inf. Center, Ft. Belvoir.
- Ward, D. L. and Ahrens, J. P. (1992). Overtopping Rates for Seawalls, CERC-92-3 of Miscellaneous Paper. USACE, Washington.
- Wassing, F. (1957). Model Investigation on Wave Run-Up Carried out in the Netherlands during the Past Twenty Years. CERC
- White, F. M. (2006). *Viscous Fluid Flow*. McGraw-Hill, Third Edition.
- Wong, P.P., I.J. Losada, J.-P. Gattuso, J. Hinkel, A. Khattabi, K.L. McInnes, Y. Saito, and A. Sallenger, 2014: Coastal systems and low-lying areas. In: *Climate Change 2014: Impacts, Adaptation, and Vulnerability. Part A: Global and Sectoral Aspects. Contribution of Working Group II to the Fifth Assessment Report of the Intergovernmental Panel on Climate Change* [Field, C.B., V.R. Barros, D.J. Dokken, K.J. Mach, M.D. Mastrandrea, T.E. Bilir, M. Chatterjee, K.L. Ebi, Y.O. Estrada, R.C. Genova, B. Girma, E.S. Kissel, A.N. Levy, S. MacCracken, P.R. Mastrandrea, and L.L. White (eds.)]. Cambridge University Press, Cambridge, United Kingdom and New York, NY, USA, pp. 361–409.
- Xiaomin, W., Liehong, J., and Treuel, F. M. (2013). The study on wave run-up roughness and permeability coefficient of stepped slope dike. *Proceedings of the 7th International Conference on Asian and Pacific Coasts (APAC 2013)*, pages 295–299.
- Yang, S. Q., and Lee, J. W. (2007). Reynolds shear stress distributions in a gradually varied flow in a roughened channel. *Journal of Hydraulic Research*, 45(4), 462–471.

## A Appendix

### A.1 Flow depth filtering technique (Robust Outlier Cutoff)

A commonly used technique is to estimate the variance of the sample, estimated by means of the STD, to establish the filtering bounds around a certain number of STD away from the mean. An alternative way to estimate the variance can be done through robust estimators, by using the Median (MED) and the Median Absolute Deviation (MAD):

$$\tilde{h}' = k \text{MAD}(h) = k \text{MED}(|\eta|) \quad (\text{A.1})$$

being  $k$  a coefficient and  $\eta$  the time series of the free surface deviation from the median value:

$$\eta = h - \tilde{h} \quad (\text{A.2})$$

with  $\tilde{h} = \text{MED}(h)$ . When a Gaussian behaviour is assumed,  $k$  takes the value (Rousseeuw and Croux 1993):

$$k = 1.483 \quad (\text{A.3})$$

The MAD was popularized by Hampel (1974). It can be obtained by sorting the absolute value of the residuals around the median and selecting the value corresponding to the 50 %. On the question of how many standard deviations are necessary to be accounted for to make sure that "good data" is not filtered out, the universal threshold represents a conservative estimator. It can be expressed as (Goring and Nikora 2002):

$$\lambda_u = \sqrt{2 \ln(N)} \quad (\text{A.4})$$

with  $N$  the total number of data points of the sample. Use of the universal threshold yields bounds wide enough to avoid filtering out good data, even if the underlying distribution is slightly skewed, but (usually) narrower bounds than those proposed by the LUV technique. The skewness of the flow depth distribution may not be affected by the filtering technique. If the final distribution is skewed, MAD could be estimated for both deviations departing from the MED value on the upper and lower directions and, consequently, different filtering thresholds could be defined for both positive and negative deviations.

The filtering criterion can be thus written as:

$$\left( \frac{\eta}{\text{MAD}(\eta)} \right)^2 \leq (\lambda_u k)^2 \quad (\text{A.5})$$

## A.2 Sampling time uncertainty on velocity measurements

Choice of the sampling time was done based on a histogram sensitivity analysis over the 1V:2H setup, as shown in Fig. A1. Figure A1 shows that velocity Probability Density Function (PDF) for sampling times ( $t_{sample}$ ) of 300 s and 600 s, respectively, are nearly coinciding when compared to smaller sampling times. For the sake of clarity, best fit normal distributions have been also considered in Fig. A1, showing that even after  $t_{sample} = 120$  s, no significant difference occurs.

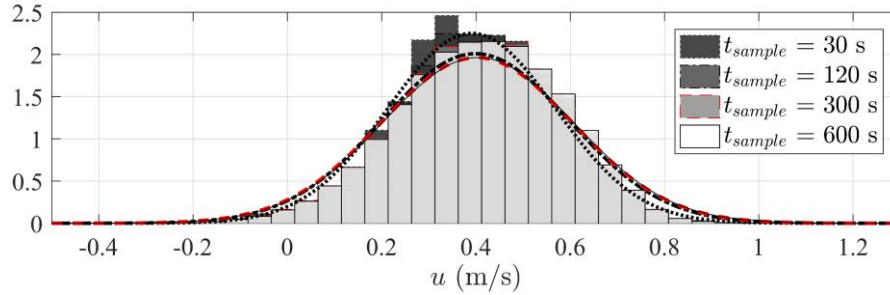


Figure A1. Probability Density Function of the velocity at the sweet-spot (SS) measured at a representative flow location (i.e. over the edge of step 6 of slope 1V:2H for  $q = 0.0862 \text{ m}^2/\text{s}$ ).

Additionally, confidence intervals for the mean and standard deviation of the velocity at the sweet spot have been computed (see Fig. A2). The confidence interval corresponds to the confidence level  $1 - \alpha$ , with  $\alpha = 0.01$ . The computation of the confidence levels for the mean value has been done based on a  $t$ -student analysis  $t_{\alpha/2, n-1}$  with  $n$  the number of samples considered within the considered  $t_{sample}$ . For the standard deviation confidence levels, a chi-squared analysis has been performed. Further information on the estimation of significance levels can be found in Chapter 8 of Ross (2009).

For excessively low sampling times, the samples are not representative of the entire hydrodynamic process. After some eddies pass under the ADV ( $t_{sample} > 10$  s) the obtained samples are more representative. However, small sampling times have been left in Fig. A2 to illustrate how confidence intervals considerably narrow with increasing sampling times, especially for the velocity variance analysis.

The  $t$ -student analysis  $t_{\alpha/2, n-1}$  assumes that  $n$  is the number of independent samples. A more accurate approach to estimate uncertainty bounds can be based on the autocorrelation function of the velocity series, which measures which part of every new sample depends on the previous one. Thus, an effective samples size could be defined as (Kass et al. 1998):

$$n_{eff} = \frac{n}{\tau_\rho} \quad (\text{A.6})$$

with  $\tau_\rho$  the autocorrelation time (Kass et al. 1998):

$$\tau = 1 + 2 \sum_{k=1}^{\infty} \rho(k) \quad (\text{A.7})$$

with  $\rho(k)$  the autocorrelation function, i.e., the correlation coefficient between the process at times  $t$  and  $t + k$  (Pope 2000):

$$\rho(k) \equiv R(k) / \overline{u(t)^2} \quad (\text{A.8})$$

with  $k$  the lag time and  $R(k)$  the autocovariance (Pope 2000):

$$R(k) \equiv \overline{u(t) u(t+k)} \quad (\text{A.9})$$

The effective sample size could be interpreted as an equivalent number of independent observations and admits more complex expressions than the herein proposed (e.g., see Vallejos and Osorio 2014). Thus, uncertainty bounds can be computed accounting for the intrinsic correlation of the data, as shown in Fig. A2. It is clear that the confidence intervals in the right-hand side of Fig. A2 are more accurate as they are able to cover the oscillations that the estimators show with increasing sampling time whereas in the left-hand side the confidence intervals fail.

The mean velocity of the analysed ADV recording is 0.40 m/s and its standard deviation 0.20 m/s which results in a turbulent intensity of 50 %; which is representative of the most turbulent flow case studied later. The uncertainty analysis for  $t_{sample} = 300$  s showed that the mean velocity can be determined with  $\pm 1.74$  % (90 % confidence level),  $\pm 2.09$  % (95 % confidence level) and  $\pm 2.74$  % (99 % confidence level). For the standard deviation, the uncertainty ranges between  $-2.36$  % to  $2.51$  % (90 % confidence level),  $-2.80$  % to  $3.00$  % (95 % confidence level) and  $-3.69$  % to  $3.98$  % (99 % confidence level). In any case, the mean velocity holds an uncertainty below 3 % and the velocity standard deviation below 4 %. When comparing the mean velocity determined at 300 s against the velocity determined at 600 s, the relative difference is 0.69 %. For the standard deviation, this relative difference reduces to 0.10 %. Thus, for both quantities, the relative difference is below 1 %.

The autocorrelation function itself is also of utmost interest in turbulent flows as it allows computation of integral timescales (Pope, 2000):

$$T_t \equiv \int_0^{\infty} \rho(k) dk \quad (\text{A.10})$$

The autocorrelation function for different sampling times can be found in Fig. A3. Conclusions on the necessary sample time are in agreement with the conclusions obtained from the comparison of the velocity probability density functions of Fig. A1. Moreover, it supports the choice of  $t_{sample} = 300$ s. Comparison on the integral time scale for different sample times can be found in Fig. A4. The one-dimensional velocity spectra can be obtained as (Pope 2000):

$$E(\omega) = \frac{2}{\pi} \int_0^{\infty} R(k) \cos(\omega k) dk \quad (\text{A.11})$$

where  $\omega$  is the frequency  $2\pi/k$ . Streamwise velocity spectra ( $E_{11}$ ) for different sample times are shown in Fig. A5. The  $-5/3$  Kolmogorov slope can be clearly observed independently of the sample time.

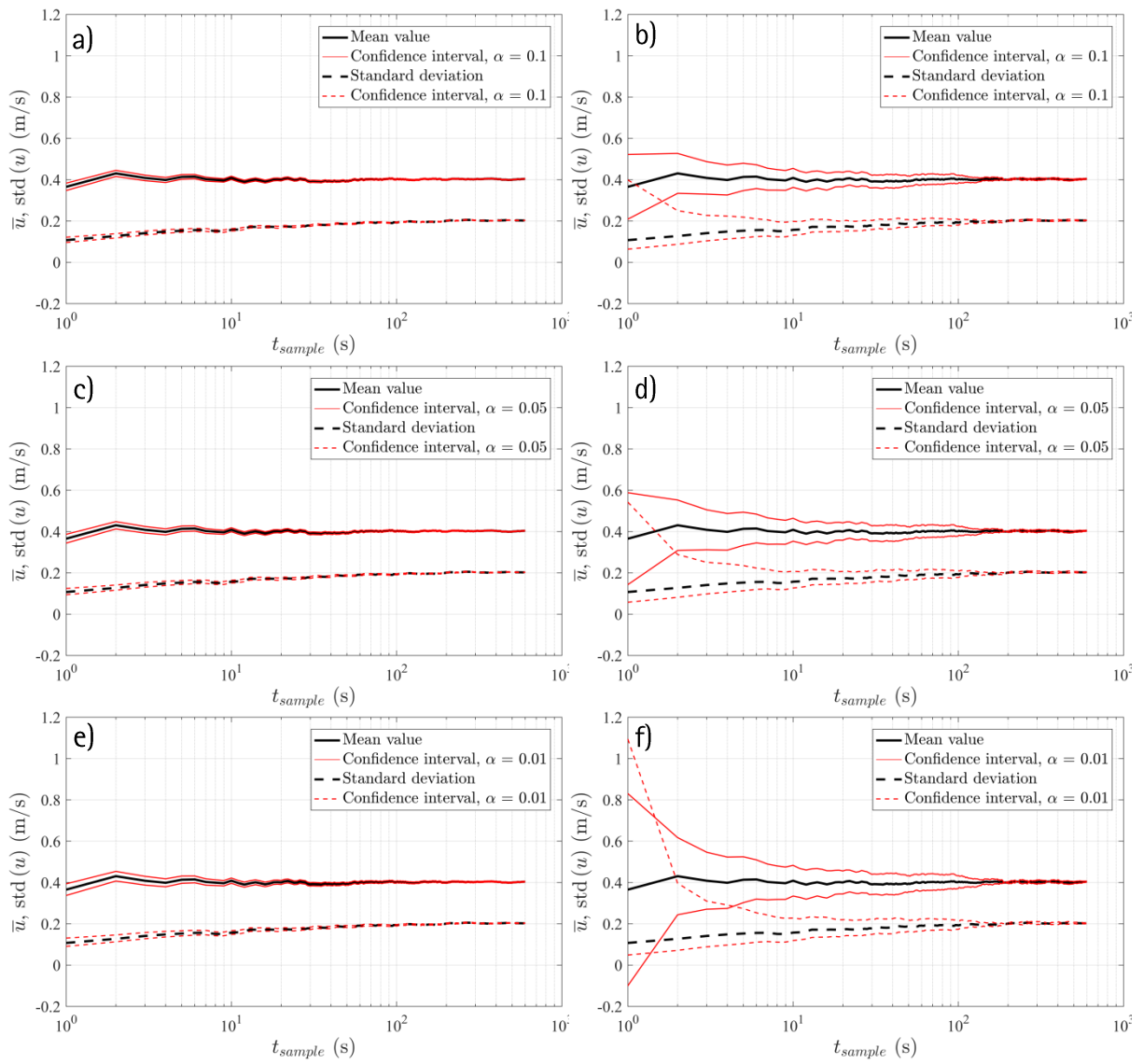


Figure A2. Confidence intervals for different confidence levels for the mean velocity and the fluctuating part: a) and b)  $\alpha = 0.10$ , c) and d)  $\alpha = 0.05$ , e) and f)  $\alpha = 0.01$ . Left: assuming independent data samples; and right: accounting for intrinsic autocorrelation of the data samples.

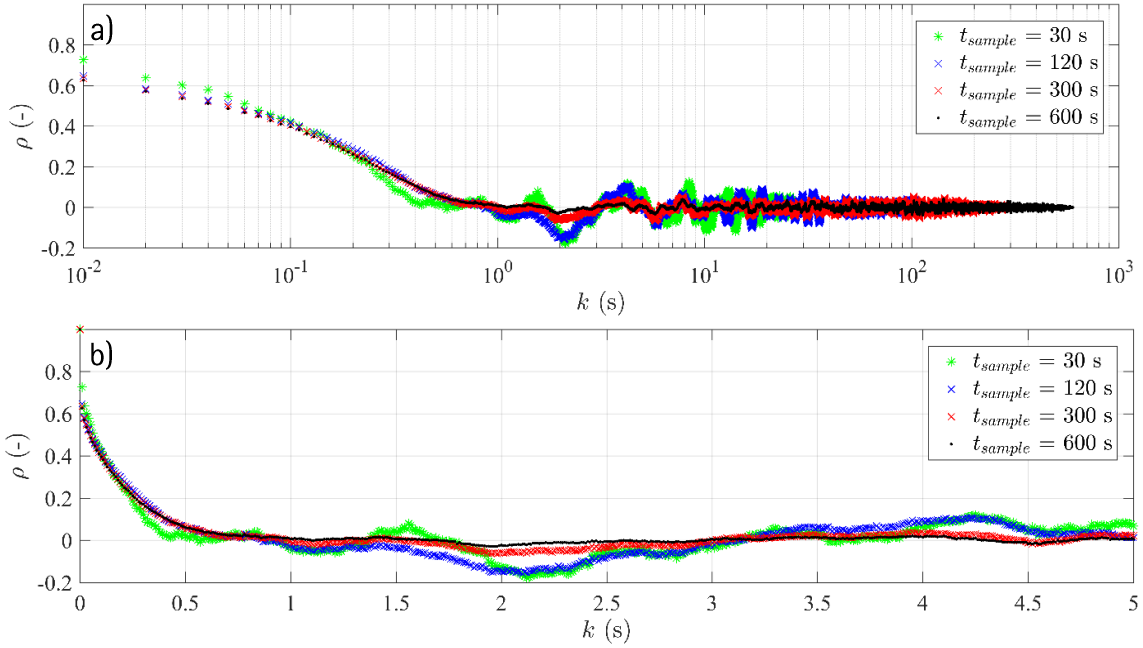


Figure A3. Autocorrelation function for different sampling times, a): time log scale, b): time linear scale.

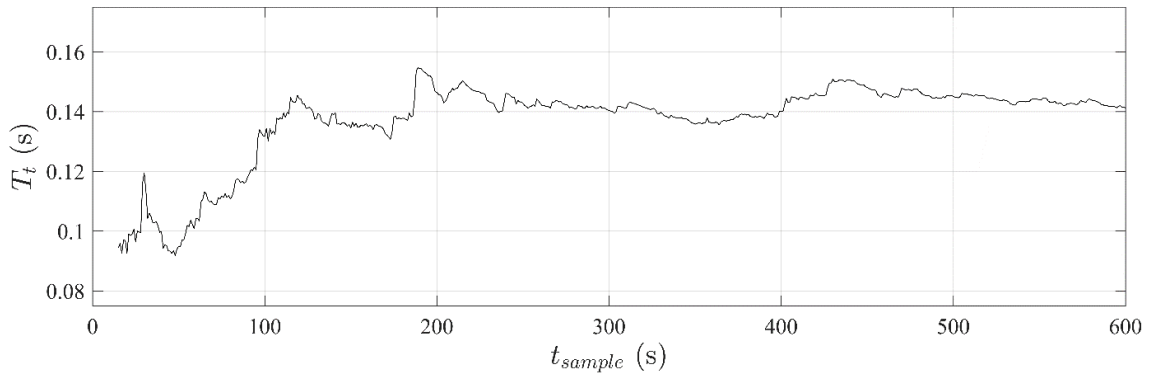


Figure A4. Integral time-scales determined by integration of the autocorrelation functions for different sample times.

In addition to the temporally dependent autocorrelation, the spatial autocorrelation can be defined in terms of the two-points correlation. Thus, instead of expressing a temporal scale it is rather showing the turbulent spatial length scale of the eddies. A simple expression for the shape of the autocorrelation function can be defined as:

$$\rho(s) = e^{-|s|/L_{t,s}} \quad (\text{A.12})$$

with  $L_{t,s}$  the turbulent length scale in the direction of the spatial lags  $s$ . More complex and complete autocorrelation functions (e.g., Bessel functions) can be also defined (see Pope 2000). As it is not likely to be reproduced the curvature at  $\rho(s = 0)$  – and consequently the Taylor microscale – the herein proposed function may be sufficient.

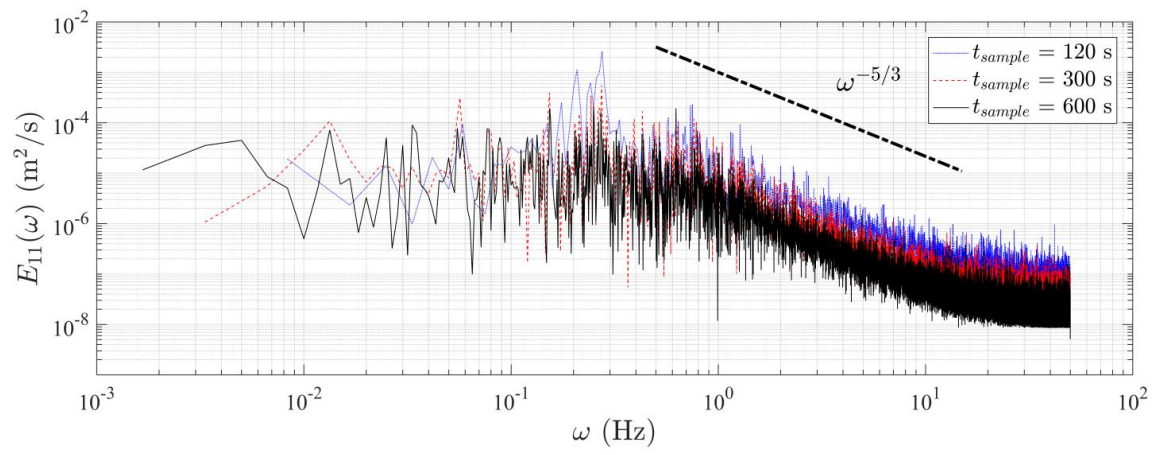


Figure A5. Streamwise velocity frequency spectra for different sample times.

### A.3 Air concentration profiles

The double-tip conductivity probe has been mainly employed to determine air-water interface velocities which may represent the flow velocity if a slip-free air bubble transport is assumed. Besides this information, the probes give the time-averaged air concentration or void fraction, i.e. the ratio of the time in which the probe was in air over the full sample time.

Subsequently, typical air concentration profiles are illustrated and compared to a theoretical air concentration model developed by Chanson (1996) for spillway flows. Figure A.6 shows that the data compares fairly well with this model, indicating the similarity between the present horizontal flume and aerated chute flows in spillways. In addition, it may be concluded that the gathered data is not significantly affected by model effects, e.g. due to a different buoyancy than in the prototype case.

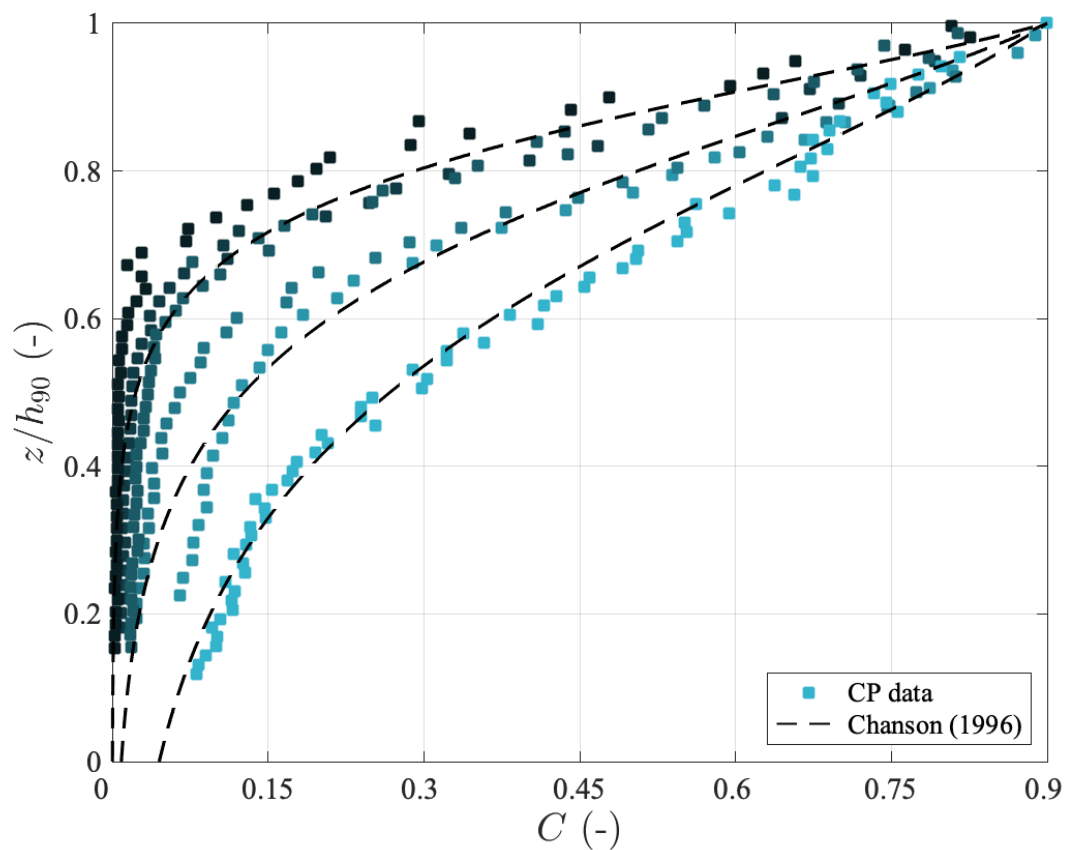


Fig. A.6. Comparison of some void fraction profiles to a theoretical air-bubble diffusion model by Chanson (1996) for mean air concentrations of 0.15, 0.25 and 0.35.